Deformation Processes in Magnetron Sputtered Nanocrystalline Palladium and Palladium Gold Films

Vom Fachbereich Material- und
Geowissenschaften genehmigte

Dissertation

zur Erlangung des akademischen Grades
Doktor der Ingenieurwissenschaften

vorgelegt von
Dipl.-Phys. Anna Castrup
geboren am 23.09.1982 in Herford

Tag der Einreichung: 15.05.2013
Tag der Prüfung: 05.11.2013

Referent: Prof. Dr. Horst Hahn
Koreferent: Prof. Dr. Martin Heilmaier
Darmstadt, 2013
D17

Erklärung

Die vorliegende Arbeit wurde im Zeitraum von Dezember 2006 bis Januar 2011 im Institut für Nanotechnologie des Karlsruher Instituts für Technologie unter der Anleitung von Herrn Prof. Dr.-Ing. Horst Hahn durchgeführt.

Hiermit versichere ich an Eides statt, dass ich die vorliegende Arbeit selbstständig verfasst und keine anderen als die angegebenen Quellen und Hilfsmittel verwendet habe. Von mir wurde noch kein Promotionsversuch unternommen.

Östringen, den 15.05.2013

(Anna Castrup)

Contents

List of Figures

List of Abbreviations

AFM	Atomic Force Microscopy
ARB	Accumulated Roll Bonding
CPS	Counts Per Second
CVD	Chemical Vapor Deposition
ECAP	Equal Channel Angular Pressing
EDX	Energy Dispersive X-Ray Spectroscopy
FCC	Face Centered Cubic
FIB	Focused Ion Beam
FWHM	Full Width at Half Maximum
GIF	Gatan Imaging Filter
HPT	High Pressure Torsion
HRTEM	High Resolution Transmission Electron Microscopy
HTXRD	High Temperature X-Ray Diffraction
IGC	Inert Gas Condensation
MBE	Molecular Beam Epitaxy
MD	Molecular Dynamic
MEMS	Micro Electro Mechanical System
NC	NanoCrystalline
PVD	Physical Vapor Deposition
RBS	Rutherford Backscattering Spectroscopy
SEM	Scanning Electron Microscopy
SMAT	Surface Mechanical Attrition Treatment
SPD	Severe Plastic Deformation
STM	Scanning Tunneling Microscopy
TEM	Transmission Electron Microscopy
TWAS	Twin-Wire Arc-Sprayed coating
UFG	Ultra Fine Grained
UHV	Ultra High Vacuum
UPS	Ultra-violett Photoelectron Spectroscopy
UTS	Ultimate Tensile Strength
XPS	X-ray Photoelectron Spectroscopy
XRD	X-Ray Diffraction

XRR X-Ray Reflectrometry

1 Introduction

In the early 1950s two independent research groups discovered the groundbreaking relationship between grain size and strength. At the University of Sheffield E.O. Hall worked on the yielding properties of mild steel and revealed a relationship between the length of slip bands and the grain size [1]. At the same time at the University of Leeds E.J. Petch worked on the variation in cleavage strength with respect to the ferritic grain size at very low temperatures and discovered the same effect [2]. Therefore, the relationship between strength and grain size is named after the two of them: Hall-Petch relationship. In simple words it says: "smaller is stronger".

Later on it was discovered that especially metals with grain sizes below 100 nm show extraordinary mechanical properties with an enormous scope of engineering applications: microelectronics, electronic packaging, medical applications and micro electro mechanical (MEMS) devices and systems.

Even superplasticity and exceptional high strength have been reported. These properties are resulting from modified or novel deformation mechanisms, which carry the deformation in nanocrystalline metals and define their strength and ductility. The knowledge about these processes is more or less vague up to now, but their investigation is currently in focus of the scientific community.

Thus, the goal of the present work is to identify and understand the deformation processes in nanocrystalline pure metals and alloys. As sample material Pd and solid solution PdAu alloys with different Au concentrations were chosen, which were prepared by magnetron sputtering under ultra high vacuum conditions. The resulting samples show nanocrystalline structure, high density, negligible amount of crystal defects, low impurity level and low residual stresses.

Primarily the samples were deformed by tensile testing. Therefore some special requirements of thin films (1 μm thickness) have to be kept in mind: freestanding films are very delicate and difficult to handle and only very small forces can be applied. To meet these requirements the films were deposited onto supporting flexible substrates and a miniature tensile tester equipped with a special thin film clamping was used for tensile testing. Nanoindentation tests were conducted to compare the results.

The microstructural investigation was performed by transmission electron microscopy, X-ray diffraction techniques, scanning electron microscopy, energy dispersive X-ray spectroscopy, scanning tunneling microscopy, rutherford backscattering spectroscopy and X-ray photoelectron spectroscopy.

The present work is structured as follows: the present chapter (**first chapter**) introduces the reader to the thesis. The **second chapter** reviews the state of the art of mechanical properties and deformation mechanisms in metals, how nanocrystalline metals can be prepared and mechanically tested, and provides some applications of nanocrystalline metals. In the following **third chapter** an overview of the variety of the applied characterization techniques is given. The **fourth chapter** demonstrates the preparation of nanocrystalline Pd and PdAu films by magnetron sputtering: the strong dependence of the film's residual stress and microstructure on the Ar-sputtering gas pressure is discussed. In the **fifth chapter** the mechanical properties and deformation processes in pure Pd films are presented. The following **sixth chapter** extends the mechanical investigations to solid solution PdAu alloys with different Au concentration. Finally the **seventh chapter** concludes the obtained results and gives an outlook to continuative ideas.

2 Literature Review

2.1 Mechanical Properties and Deformation Mechanisms of Metals

The technologically most important material group are metals. Their outstanding properties, mechanical (combination of strength and ductility) as well as electric (conductivity), cause their dominating role in materials science history for millennia, even geological ages have been named after them [3].

The knowledge of the mechanical properties of metals and the understanding of the underlying deformation mechanisms is crucial to any mechanical engineering application. The reaction of a solid state material to mechanical load depends on the direction of the applied force. If the force is applied parallel to the sample surface the sample is sheared. On the other hand if the force is applied perpendicular to the surface the deformation has tensile character. In the following we will concentrate on tensile deformation. In this case the elastic deformation is related to the applied force F via Hooke's law [3]:

$$\frac{F}{q} = E\,\frac{\Delta l}{l_0} \quad \text{or} \quad \sigma = E\epsilon \tag{2.1}$$

with l_0 the original sample length, q the sample's cross-sectional area and Δl the elongation. In other words: the normal stress σ is proportional to the strain ϵ. The constant of proportionality is defined as elastic modulus E. Elastic deformation is fully reversible and can be understood as a straining process in-between the sample's atoms.

Hooke's law is valid only for very small deformations. At larger deformation stress and strain are no longer proportional, the stress is reduced, the material deforms plastically. Plastic deformation is macroscopically permanent and is carried by microscopic deformation processes.

The field of conventional coarse grained metals is well investigated and understood, their properties will be explicated in detail in chapter 2.1.1. For nanocrystalline metals with grain sizes below 100 nm research is still in progress and different approaches exist, which will be quoted in chapter 2.1.2.

2.1.1 Conventional Metals

The atomic structure of metals is crystalline and their ductility, the ability to deform plastically, is carried by microscopic changes. The overall crystal lattice structure remains constant, as was proven by X-ray diffraction methods, which implies that complete crystal regions are moved along crystallographic planes, called glide planes. In face centered cubic (fcc) crystals these glide planes are parallel to the {111} plane of the crystal. Theses gliding processes result in two-dimensional lattice defects: edge dislocations and screw dislocations. Figure 2.1 illustrates the movement of two lattice planes and the corresponding edge dislocation.

At larger strains the dislocation density increases, because moving dislocations can react with primary dislocations in the crystal lattice and become trapped [3]. To accommodate these immobile dislocations and the macroscopic deformation speed new mobile dislocations have to be formed. The most common source of dislocations is the Frank-Read source: a mobile two-dimensional dislocation with two pinning points. If an appropriate stress is applied, the dislocation is bent, forms a semicircle and finally a dislocation ring is released and the process is reiterated.

Much less dominating deformation processes in coarse grained metals are diffusional creep and twin formation. Diffusion processes are dominating in coarse grained metals at high temperatures, but are of minor importance at ambient temperatures.

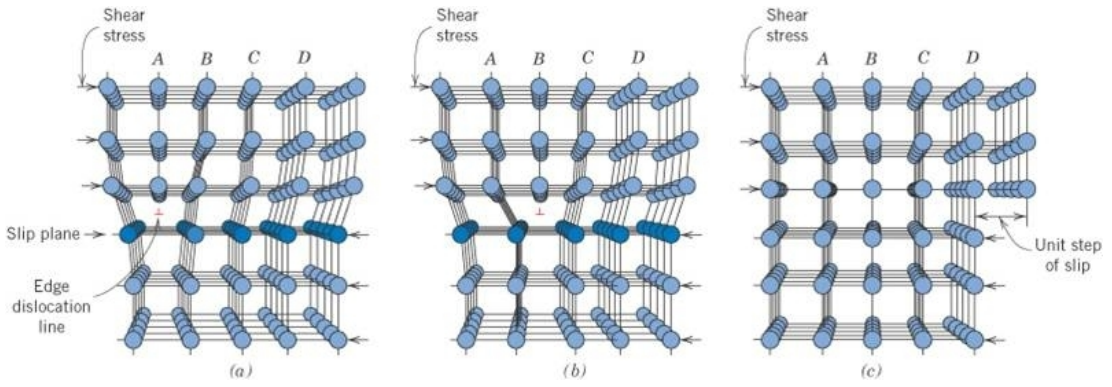

Figure 2.1: Atomic rearrangements that accompany the motion of an edge dislocation as it moves in response to an applied stress [4].

Twin boundaries are mirror-symmetric lattice structures, they are related to shearing processes in the grains during tensile straining. They develop spontaneously and instantaneously and may be accompanied by a sudden decrease in the stress. The required energy for twin formation is quite high, because atoms that are distanced from the twinning plane have to travel large distances. Hence, gliding processes are preferred at ambient temperatures. At low temperatures, where the strength is increased, twinning becomes more important.

2.1.2 Nanocrystalline Metals

In nanocrystalline metals conventional deformation processes are hindered by the grain boundaries. The volume fraction of the grain boundary becomes more important the smaller the grain size is. Hence, in nanostructures the impact of intragranular gliding is remarkably reduced. The change in the deformation mechanisms is coupled with changes in the mechanical properties [6]:

The strength increases extraordinary with decreasing grain size. The relationship between yield strength σ_y and grain size d is called Hall-Petch relationship and is described empirically by

$$\sigma_y = \sigma_0 + \frac{k_y}{\sqrt{d}} \,, \tag{2.2}$$

with σ_0 and k_y material dependent constants. Physically this effect can be understood as result of the difficulty to move dislocations through grain boundaries and the resulting stress concentration and due to dislocation pile-up at the boundaries. The increase in strength is experimentally proven for various metals down to grain sizes of about 10 nm [6], for smaller sizes the Hall-Petch relationship is assumed to be no longer valid, but experimental data is rare due to difficulties in sample preparation. Inverse Hall-Petch as well as saturation are debated [6].

Nanocrystalline metals show reasonably good ductility [7]. Even superplastic behaviour was observed in nanocrystalline copper ($d = 24$ nm) at room temperature [8]. Earlier nanocrystalline metals often suffered from brittleness, they fractured even in the elastic regime. This effect was later on attributed to preparation effects like high residual stresses, porosity and contamination. Ductility is often limited by intensely localized inelastic strain in nanocrystals. Fracture surfaces are characterized by a mixture of ductile dimples and shear regions [6].

The strain rate sensitivity of nanocrystalline metals is rather strong. The strain rate sensitivity m describes the change in flow stress σ due to variation of the strain rate $\dot{\epsilon}$ and is defined as:

$$m = \frac{\partial \log\sigma}{\partial \log\dot{\epsilon}}|_{\epsilon,T}, \tag{2.3}$$

for constant temperature T and strain ϵ. The value of the strain rate sensitivity is believed to be coupled with different deformation mechanisms. In coarse grained metals the strain rate sensitivity is always $m < 0.01$, whereas in superplastic metals, where grain boundary sliding is dominating, $m \geq 0.5$. Nanocrystalline metals show m-values in-between these extremes [9].

Thermally activated deformation processes

Energy barriers that hinder the movement of dislocations are commonly in the orders of electron-volt or less with only some hundreds of atoms involved. Under these conditions the thermal energy favors to overcome these barriers. Hence, with rising temperature the stress required to move dislocations at a given strain rate decreases [11].

According to the first and second principles in thermodynamics the Gibbs free energy ΔG, which is responsible for the energy barriers, can be written as:

$$\mathrm{d}\Delta G = \left(\frac{\partial \Delta G}{\partial \tau}\right)_T \mathrm{d}\tau + \left(\frac{\partial \Delta G}{\partial T}\right)_\tau \mathrm{d}T, \tag{2.4}$$

with $\Delta V = -\left(\frac{\partial \Delta G}{\partial \tau}\right)_T$ the activation volume, $\Delta S = -\left(\frac{\partial \Delta G}{\partial T}\right)_\tau$ the activation entropy, T the temperature, and τ the applied shear stress. If the activation volume ΔV is constant, equation (2.4) becomes:

$$\mathrm{d}\Delta G = -\Delta V\, \mathrm{d}\tau + \left(\frac{\partial \Delta G}{\partial T}\right)_{\tau=0} \mathrm{d}T, \tag{2.5}$$

integrating (2.5) results in:

$$\int \mathrm{d}\Delta G = \int -\Delta V\, \mathrm{d}\tau + \int \left(\frac{\partial \Delta G}{\partial T}\right)_{\tau=0} \mathrm{d}T, \tag{2.6}$$

which simplifies to:

$$\Delta G = -\Delta V \tau + \int \mathrm{d}\Delta G_{\tau=0}. \tag{2.7}$$

By defining ΔG_0 as the temperature-dependent barrier activation energy at zero stress ($\tau = 0$), one obtains:

$$\Delta G = \Delta G_0 - \tau \Delta V. \tag{2.8}$$

The determination of the derivation of the strain rate $\dot{\gamma}$ starts from the Orowan equation, which characterizes the proportionality of $\dot{\gamma}$, the mobile dislocation density ρ_m, the average dislocation velocity ν and the Burger's vector b:

$$\dot{\gamma} = A \rho_m b V, \tag{2.9}$$

with A a geometrical factor. Equation (2.9) can be simplified to:

$$\dot{\gamma} = \dot{\gamma}_0 \exp\left(-\Delta G / kT\right), \tag{2.10}$$

By inserting equation (2.8) into equation (2.10) one obtains:

$$\dot{\gamma} = \dot{\gamma}_0 \exp\left(-\frac{\Delta G_0 - \tau \Delta V}{kT}\right), \tag{2.11}$$

Testing the sample with two different strain rates $\dot{\gamma}_1$ and $\dot{\gamma}_2$ at constant temperature T results in:

$$\frac{\dot{\gamma}_2}{\dot{\gamma}_1} = \exp\left(\frac{\Delta V(\tau_2 - \tau_1)}{kT}\right), \tag{2.12}$$

which simplifies to:

$$\Delta V = \frac{kT \ln\left(\frac{\dot{\gamma}_2}{\dot{\gamma}_1}\right)}{(\tau_2 - \tau_1)}, \tag{2.13}$$

The shear stress τ and its components $\dot{\gamma}$ are related to the normal stress σ and its corresponding components $\dot{\epsilon}$ by the Von Mises yield criterion $\tau = \sigma/\sqrt{3}$ and $\dot{\gamma} = \sqrt{3}\,\dot{\epsilon}$. Applying this criterion to equation (2.13) results in:

$$\Delta V = \frac{\sqrt{3}\,k\,T\,\ln(\dot{\epsilon}_2/\dot{\epsilon}_1)}{\sigma_2 - \sigma_1}, \tag{2.14}$$

with strain rate $\dot{\epsilon}_2 > \dot{\epsilon}_1$ and flow stress $\sigma_2 > \sigma_1$. The activation volume is given in multiples of b^3, the Burger's vector. The activation volume is another parameter to identify deformation mechanisms.

As deformation mechanisms in nanocrystalline metals several mechanisms are under discussion [6]: intragranular slip, dislocation motion, dislocation nucleation by grain boundary sources, forest dislocations, Coble creep, grain boundary sliding, twin formation, and stress-induced grain coarsening. Some deformation mechanisms are depicted exemplary in figure 2.2. The mechanisms are explained in more detail in the following [6, 9, 10, 12]. Additionally their corresponding strain-rate sensitivity and activation volume are given as far as they are known.

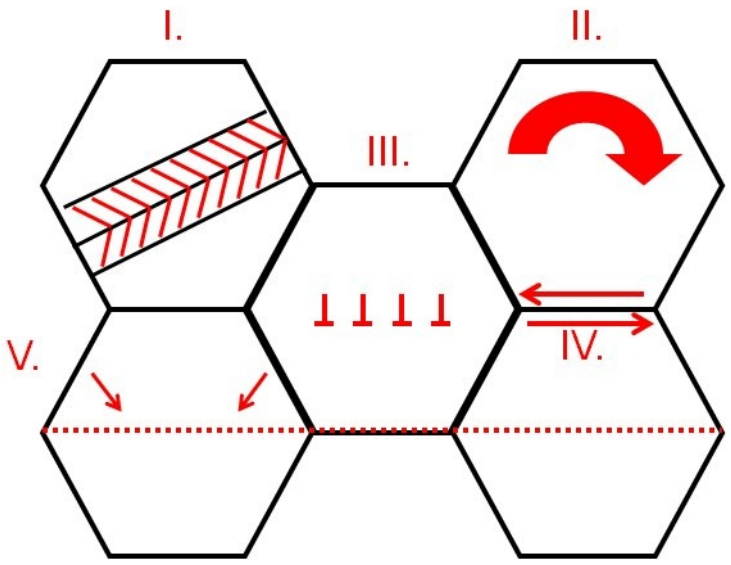

Figure 2.2: Deformation processes in nc materials as discussed in the literature: I. Twin formation, II. Grain Rotation, III. Dislocation Motion, IV. Grain boundary sliding, V. Formation of mesoscopic shear planes.

Intragranular Slip and Dislocation Motion

In post-mortem TEM investigations only very few dislocations are found in the grain interior of nc grains, even though in-situ X-ray diffraction shows a remarkably increase in the peak broadening upon loading, which is related to the dislocation density. This points to a reduced ability of nc materials to store dislocations in the grains. Molecular dynamic (MD) simulations suggest that the evolving dislocations travel through the grain interior and disappear into the grain boundary. Even stationary dislocations might relax into a nearby grain boundary after stress-removal due to the high density of grain boundaries in nc materials. Here the activation volume is in the order of $\Delta V = 10...100\ \mathrm{b}^3$.

Dislocation Nucleation by Grain Boundary Sources

The operation of Frank-Read sources is hindered in nc grains due to the limited space in-between the grain boundaries. A possible source of dislocations in these systems are the grain boundaries themselves. In MD simulations dislocation rings were observed that were nucleated at the grain boundaries, where a large number of dislocations is located, and travelled through the grain interior. The activation volume for this process is in the order of $\Delta V = \pi\ \mathrm{b}^3$.

Forest Dislocations

The dislocation pile-up of Frank-Read sources operating primarily in coarse grained materials is also called forest dislocations. Dislocations evolve at the Frank-Read source and form circles around the source, which are pushed away by successive dislocations and move towards the grain boundaries, where they pile up. This process is associated with the parameters in the order of $m << 0.01$, $\Delta V = 100...10\ 000\ \mathrm{b}^3$.

Coble Creep

Coble creep is a form of diffusional creep, where atoms move along the grain boundaries during deformation. By this process the grain boundary slides through the material associated with a net material transport. Coble creep is primarily associated with superplastic flow. The deformation parameters are in the order of $m = 1$, $\Delta V = 1\ \mathrm{b}^3$.

Grain Boundary Sliding and Formation of Mesoscopic Shear Planes

Grain boundary sliding is suggested to be the dominant deformation mechanism in superplasticity [13]. Interfacial sliding can lead only to small creep strains because of

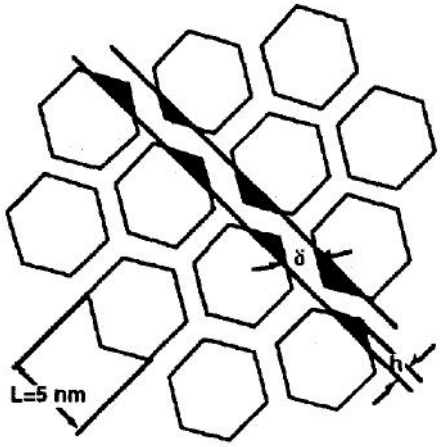

Figure 2.3: 2D-Schematic representation of a grain arrangement in a nanocrystalline material. A mesoscopic planar interface can be formed by grain boundary migration. Atoms located in the darker regions have to be rearranged [13].

steric hindrance due to the presence of blocking grains, which prevents any extended deformation.

Contrarily, by forming mesoscopic shear planes several grains can shear along these planes. This can eventually lead to large strains and even superplastic deformation. To allow the formation of mesoscopic shear planes the grain boundaries migrate into the grain interior, compare the black regions in fig. 2.3. This process is associated with the deformation parameters in the order of $m = 0.5$, $\Delta V = 1\ \mathrm{b}^3$.

Grain Rotation

Nanocrystalline grains are able to rotate along their grain boundaries. By this rotation two or more neighbouring grains can coalesce and form one single grain. The rotation is needed to bring the crystallographic orientations of the grains together and eliminate the grain boundary between the grains. The resulting larger grain is often aligned along the direction of shear and is called shear band.

Stress-induced Grain Coarsening

Stress-induced grain coarsening was directly observed in nc Al by in-situ TEM straining measurements [14]. The process is supposed to be resulting from interaction of the external stress with grain boundary dislocations or a shear-coupled motion of the grain boundaries. Grain coarsening might improve the ductility of nc materials.

Twin Formation

The formation of twin boundaries as already described in chapter 2.1.1 is mainly observed at extreme temperatures or high stress levels, like in nanoindentation, grinding, high pressure torsion, ball milling etc. This implies that the required stress to activate the formation of twin boundaries is very high.

2.1.3 Strengthening Mechanisms

The strength of a material depends not only on its grain size as is described by the Hall-Petch relationship in equation (2.2). It can be improved by several hardening processes that will be discussed in the following.

The most effective hardening processes use alloying with a second constituent to enhance the material's strength [3]. If the alloy is in solid solution the process is called solid solution hardening. Discrete precipitates of the second constituent cause the so-called precipitation hardening. If the second constituent is non-metallic and forms small particles in the matrix the strengthening mechanism is called dispersion hardening.

A third class of strengthening mechanism is the so-called strain hardening, alternatively referred to as work hardening. Here the strength of a material is improved by plastic deformation [10].

Solid Solution Hardening

In solid solution alloys the second constituent is incorporated in the lattice of the matrix atoms. The second constituent interacts with dislocations moving through the lattice during deformation and causes the solid solution hardening. This interaction is resulting from the differences in atom size (parelastic interaction) and elastic modulus (dielastic interaction) of the matrix and the second constituent.

The parelastic interaction in fcc metals affects only edge dislocations. The edge dislocation results in a hydrostatic stress field with widened and compacted zones in the lattice. The second constituent alters the bonding interaction between the atoms in the edge dislocation. Hence, the elastic deformation of the lattice caused by the second constituent increases the restoring force, that has to be overcome by the edge dislocation when passing the second constituent. This results in an increasing critical stress in the solid solution compared to the pure matrix [3]. The maximum force F^d_{max} caused by parelastic interaction is [3]:

$$F_{max}^{p} = Gb^2 \left|\delta\right|, \tag{2.15}$$

with

$$\delta = \frac{d \ln a}{dc^a}, \tag{2.16}$$

where G is the shear modulus, b is the Burger's vector, a is the lattice parameter and c^a is the concentration of the second constituent atoms.

The dielastic interaction is resulting from the proportionality between elastic modulus and the energy stored in a screw or edge dislocation. Hence, the lattice volume of the second constituent with a different elastic modulus alters the total energy of the screw dislocation. This results in a maximum dielastic force [3]:

$$F_{max}^{d} \approx \frac{1}{20} Gb^2 \left|\eta\right|, \tag{2.17}$$

with

$$\eta = \frac{d \ln G}{dc^a}. \tag{2.18}$$

Precipitation Hardening

Precipitates with coherent or semi-coherent phase boundaries to the matrix increase the material's strength as well [3]. Precipitates are formed by solution heattreatment above the solidus line but below the eutectic temperature, subsequent quenching and finally annealing at lower material specific temperature for a certain time [5].

Dislocations are able to cut coherent or semi-coherent precipitates. But therefore the parelastic and dielastic force have to be overcome, where in contrast to the solid solution the maximum parelastic force increases with the particle diameter $2r$ [3]:

$$F_{max}^{p} = Gb^2 \left|\delta\right| r, \tag{2.19}$$

When the dislocation cuts a coherent phase boundary, the particle is sheared by one Burger's vector. If the particle has an ordered microstructure an antiphase boundary is formed inside the particle. Therefore, a phase boundary specific force F^{pb} has to be overcome [3]:

$$F^{pb} = \tilde{\gamma} \cdot r, \tag{2.20}$$

where $\tilde{\gamma}$ is an effective phase boundary energy.

Dispersion Hardening

Small particles of the second constituent in the matrix may result in a remarkable increase of the mechanical strength [3]. The particles act as obstacles for moving dislocations that cannot be cut by the dislocations, because the particles are incoherent with the matrix [5]. The dislocations have to bulge between the particles which can be compared to the mechanism of the Frank-Read source. While passing the particle the diameter of the dislocation increases. Finally two parallel dislocation segments will get in contact and form a free dislocation and a dislocation loop enclosing the particle. This process is called Orowan mechanism.

The critical stress σ_o to initiate the Orowan mechanism depends on the mean particle diameter $2r$ and the mean distance l between the particles:

$$\sigma_O = \frac{Gb}{l - 2r}. \tag{2.21}$$

Dispersion hardening is not as effective as precipitation hardening. To observe the most effective hardening the particles have to be small hard and numerous [5]. But their advantage is their improved temperature stability: the particles neither dissolve or grow in size at high temperatures.

Strain Hardening

Strain hardening has been used for ages to strengthen metals, but is still a process that is only semi quantitatively understood [10]. During deformation more and more dislocations are formed, the strain fields of these dislocations interact and increase the strength. There are two forms of strain hardening: interplane hardening and intraplane hardening. Interplane hardening denotes the interaction of stress fields of edge dislocations moving on parallel planes. Intraplane hardening corresponds to dislocations interacting with slip obstacles in their glide plane.

Method	+	-
Ball milling	simple and cost-effective	high impurity level
HPT	cheap, small grain sizes	small sample dimensions, high dislocation density
ECAP	large sample pieces	min. grain size: 100 nm
IGC	very small grains ($\leq$10 nm)	porosity and high costs
Electrodeposition	small grains	high impurity level
Magnetron sputtering	small grains, alloys	limited thickness (several μm)
MBE	small grains	very slow $\Rightarrow$ thickness $\leq$ 1 μm

Table 2.1: Methods to prepare nc materials including the method's advantages and disadvantages.

2.2 Preparation of Nanocrystalline Metals

On the laboratory-scale there are already several techniques available to produce nanocrystalline metals. They are in general prepared by two different approaches: top-down and bottom-up. Where top-down refers to originally coarse grained materials whose microstructure is broken down to the nanoscale: typical variants are mechanical milling/alloying (ball milling, cryomilling) and severe plastic deformation (SPD) (high pressure torsion (HPT), equal channel angular pressing (ECAP), accumulated roll bonding (ARB), and surface mechanical attrition treatment(SMAT)). The bottom-up approach is characterized by nanostructures that are built up atom by atom and/or layer by layer: gas phase consolidation (inert gas condensation (IGC)), electrodeposition and physical vapor deposition (PVD) (magnetron sputtering, molecular beam epitaxy (MBE)), and chemical vapor deposition (CVD) [6, 16]. Advantages and disadvantages of the different approaches are summarized in table 2.1.

Historically, ball milling und IGC have been the first methods available. But despite their ability to produce nc materials with grain sizes below 100 nm both methods suffer from several drawbacks:
IGC processed materials show relative high porosities due to the compaction process. Additionally, the processing costs are quite high compared to the low amount of material produced. The process itself is complex and cannot be easily employed for different materials or alloys.
Ball milling on the other hand is an easy-to-use technique, but also requires a compaction step, that leads to porosity. Additionally, high impurity contents are observed due to the wear of friction produced by the grinding balls, which are fre-

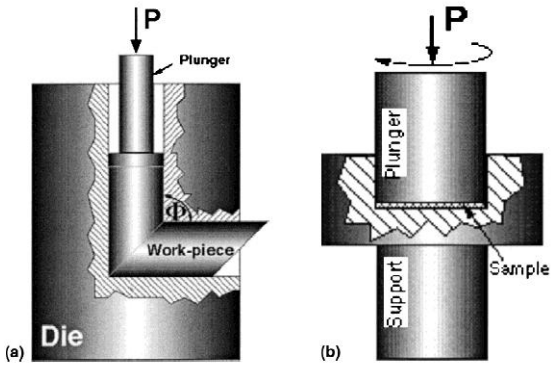

Figure 2.4: Schematics of severe plastic deformation techniques: (a) equal-channel angular pressing and (b) high-pressure torsion [15].

quently made of stainless steel. The resulting lattice structure shows considerable lattice distortions [6].

Severe plastic deformation is one of the preparation methods with high potential for industrial application [7]. Bulky pieces of material are heavily deformed by rolling, pressing and/or torsional deformation in repeated manner. Equal channel angular pressing and high pressure torsion are the most common variants of SPD, schematic views of these methods are displayed in fig. 2.4.

Materials prepared by SPD methods have full density and low impurity levels. They can easily be produced in larger amounts and the resulting sample shape is still bulky, which is desirable for industrial applications. Unfortunately, the microstructure of spd processed materials is usually characterized by larger grains, which are above 100 nm in size [6, 16].

Electrodeposition (direct current and pulsed) is used to prepare sheets of nc metals and metallic alloys. Thicknesses of 100 μm and more are routinely produced with grain sizes well below 100 nm and narrow grain size distributions. Additionally, no porosity is present in electrodeposited films. These features and their commercial availability made them highly interesting candidates for mechanical investigation, because the pores present in other samples resulted in misleading material properties [16]. Later on, the originally underestimated amount of impurities due to the additives in the electrolyte bath was considered to also effect the deformation mechanisms and cleaner preparation methods like ultra high vacuum (uhv) physical vapor deposition were investigated:

Magnetron sputtering is the PVD technique with the highest potential to prepare thick coatings in reasonable time with nc microstructure, full density and low impurity level [17–19]. A special sputtering technique was developed by A. Hodge and

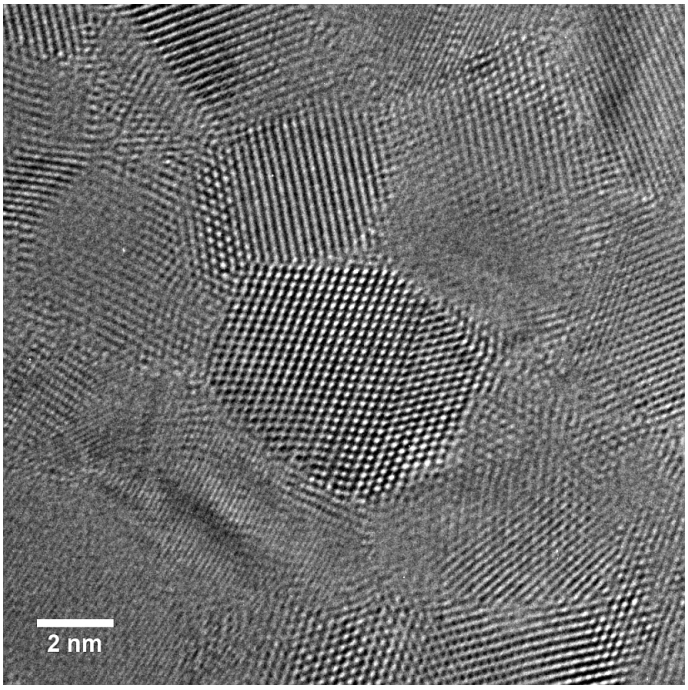

Figure 2.5: A high resolution transmission electron micrograph of a 6 nm thick magnetron sputtered Pd film.

coworkers to prepare pure ufg and nc metals: the nanoscale multilayer technology. The technique is based on the conventional multilayer technique, invented to prepare multilayers of two different materials. To prepare pure nc samples, the second material is exchanged by an interruption of the sputtering process, which can be achieved by a shutter system in front of the source or the sample. In the case of Cu, film thicknesses of 22 μm and sample diameters of 10 cm with grain sizes of 200 nm were prepared and their mechanical properties were investigated, showing improved strength compared to conventional Cu [18]. By sputtering very thin films even smaller grain sizes below 10 nm are possible, compare figure 2.5.

2.3 Mechanical Testing at the Nanoscale

The investigation of the mechanical properties of nanocrystalline materials requires special testing techniques, because nanocrystalline materials are usually limited in size, like thin films or small pellets.

The gold standard test concerning mechanical properties is the tensile test. Standard sizes are 12.8 mm diameter and 50 mm gauge length [4]. Compared to these

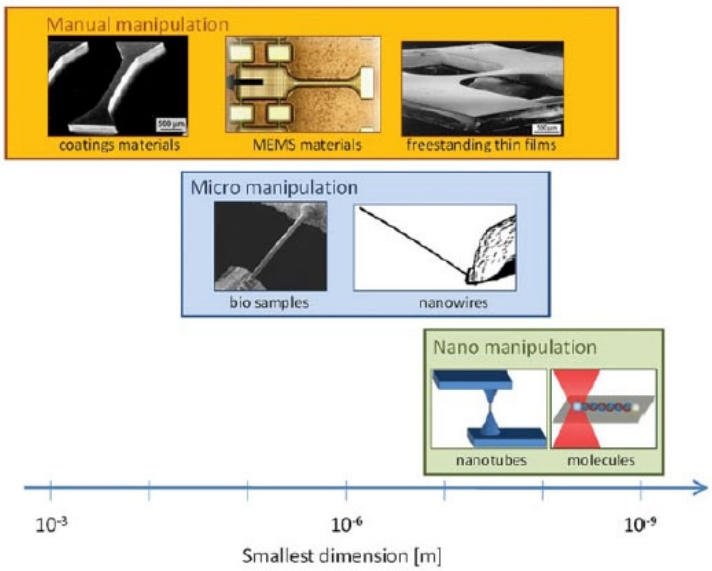

Figure 2.6: Specimen manipulation strategies are illustrated schematically across the length scales involved in micro- and nanotensile testing [21].

size testing nanocrystalline materials with 1 μm film thickness or 9 mm pellet diameter [20] requires novel device architectures. The advantage of tensile testing is the straightforward interpretation, while the technical layout can be challenging. Other techniques like nanoindentation or bulge testing are easy to execute, but the interpretation is quite difficult [21].

2.3.1 Nanoscale Tensile Testing

The main challenges in nanoscale tensile testing are related to the small sample dimensions and their fragility: handling them with conventional tools like hands or tweezers is often impossible. Additionally the actuation of the tensile tester and the acquisition of force and strain is very sensitive, because distances and forces are very small [21].

Depending on the sample size different approaches have been invented to manipulate the specimen, see fig. 2.6. Commonly, a support structure is involved. In the case of thin films flexible substrates, Si support frames or MEMS structures (microelectromechanical systems) can be used to support the films [21].

Flexible substrates as support material are very easy to fabricate and handle, because the thin film is simply deposited on the flexible substrate that can be cut in the desired shape beforehand. For tensile testing itself a conventional small scale

testing apparatus can be used, which monitors the applied force and the sample strain. As a disadvantage the measured data needs to be interpreted more carefully, because the measured force is the sum of the force applied on the thin film and the substrate. Therefore, tensile tests are performed on the flexible substrate with and without film and the film stress is calculated from the small difference between the two force-strain curves [22, 23].

Testing of free-standing films is much more challenging. To use frame structures for support [19], thin films are grown on stiff substrates like Si wafers. Subsequently, the substrate is removed in the gauge section using etching techniques, but a stable Si support frame remains. This way the sample can be handled easily with tweezers. Prior to the test the frame is cut by special diamond cutters and only the load on the free-standing film is measured.

By integrating the specimen in MEMS structures load and strain can be directly monitored using optical methods [24]. These samples are attractive for in-situ testing in microscopes like SEM and TEM, where measuring the load externally is very difficult. Another advantage is the possibility of batch processing, means many specimen can be prepared on a single wafer. This way the main disadvantage, the complex and time-consuming processing route can be compensated. But still high requirements concerning the dimensional accuracy of the integrated sensors have to be fulfilled.

2.3.2 Other Nanoscale Mechanical Tests

Several very specialized testing techniques have been invented to investigate nanostructures in the last years [25]. The most straight-forward mechanical tests are hardness tests that can be easily adapted to thin films, like nanoindentation tests. More details about nanoindentation will be given in chapter 3.4.2.

Other techniques involve special features of nanostructures and would not be applied to conventional materials, these are:

- Thermal cycling: Thin films deposited onto thicker substrates suffer residual stresses, which are caused by the different thermal expansion coefficients of the film and the substrate. After deposition the temperature of the sample decreases but the dimensional mismatch is fully accommodated in the thin film by residual stresses. These stresses cause changes in the curvature of the film which can be measured by optical methods and finally the stresses are calculated. Thermal cycling is very easy to execute, but also very limited due to the interdependence of material and thermal expansion coefficient.

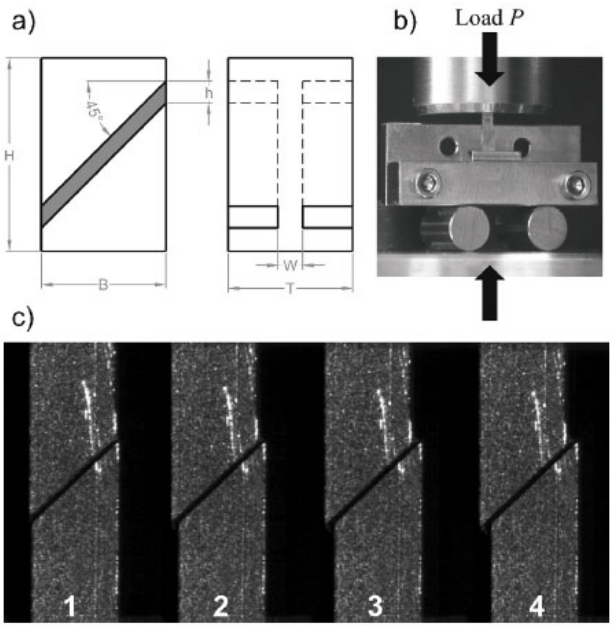

Figure 2.7: (a) Engineering drawing of the shear compression specimen (SCS), the gauge section is colored; (b) SCS mounted on sample holder and loaded by P; (c) series of consecutive plastic deformation steps [26].

- Bulge testing: A free-standing thin film supported by a Si frame is deflected by applying uniform pressure. The mechanical properties are determined by measuring the deflection behavior with optical methods. This technique requires sample preparation, because the substrate has to be removed in a defined area, additionally the data analysis is quite complicated.

- Microbeam bending: Microbeams of thicknesses between 1 to 7.5 μm are prepared out of a film by focussed ion beam (FIB) techniques and its ends are attached to the substrate. A nanoindenter with a flat punch is used to bend the microbeam. The interpretation is quite troublesome due to the complex stress state and preparational effects related to the Ga^+ ions implemented in the sample surface.

- Micropillar compression tests: Micropillars with diameters even below 400 nm prepared by FIB are compressed by a nanoindenter with a flat punch. These tests also suffer from preparational effects, but the interpretation is more straight-forward due to the defined geometry.

- Shear compression tests: Shear compression specimens are fabricated from bulk material, the samples have a gauge section, which is tilted by 45° to the loading direction, compare fig. 2.7. The gauge section experiences a superposition of shear deformation and compressive stress, where the compressive

stress helps to suppress the influence of processing faults as sources of material failure [26].

2.4 Applications of Nanostructured Materials

The extraordinary mechanical properties of nanostructured materials make them interesting candidates for several applications. They are used as coatings to enhance the surface properties of softer materials [27], as well as bulk structures for special applications e.g. medical implants [28] or dispersed nanostructures in nanocomposites [29].

Nanocrystalline coatings are applied as protective coatings to improve the friction, wear and corrosion resistance of conventional cast iron parts [27]. Possible applications are automotive cylinders, plungers, gearings, chains, turbines, bearings etc.

Figure 2.8 displays schematically the NANOSLIDE technique patented by Daimler AG [30]. The technique employs twin-wire arc-sprayed coating (TWAS) to optimise cylinder surfaces. After melting iron-carbon wires by means of an electric arc, a flow of gas is applied to spray the metal droplets onto the inner walls of the cylinders of the lightweight aluminium crankcase. Extremely fine finishing of the resultant ultra-fine-grained to nanocrystalline iron layer produces an almost perfectly smooth surface [27].

Bulk nanocrystalline materials prepared by SPD techniques, especially ECAP, can already be produced in considerable amounts, that allow direct industrial application [28]. Figure 2.9 shows a dental implant made of nanocrystalline Ti (a) compared to a conventional Ti dental implant. Due to the remarkably improved mechanical properties the diameter of the implant made of nc Ti is reduced by more than 30%. By using nanocrystalline Ti no alloying is needed to improve the mechanical properties, which is beneficial for the biocompatibility of the implants.

The fracture toughness of ceramics can be considerably enhanced by dispersing nanostructures, these materials are called superstrong and supertough ceramics [29]. They are produced by stabilizing the nanocomposite with nanoparticles like whiskers, pellets or long fibers. Additionally the dispersed nanostructures increase the creep resistance of the nanocomposite by suppressing grain boundary sliding. Even high temperature applications up to 1200 °C are possible. These superceramics may find use in severe engineering applications, like turbines or aerospace and automobile components [29].

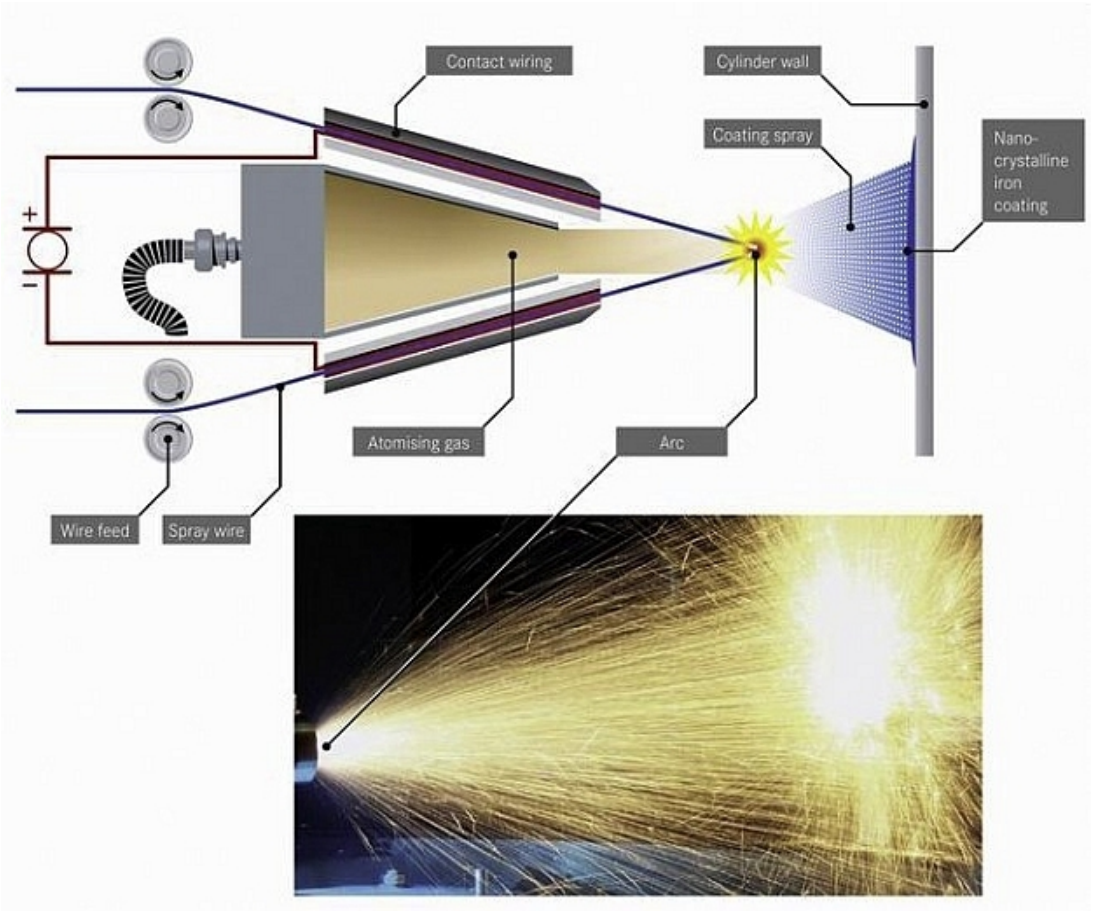

Figure 2.8: Daimler NANOSLIDE technology uses the twin-wire arc spraying process to melt metal wires and spray the molten material onto the internal cylinder wall with the help of a gas flow [27].

Figure 2.9: a) Nanocrystalline Ti dental implant Nanoimplant® (2.4 mm diameter), b) conventional dental implant Timplant® (3.5 mm diameter) [28].

3 Characterization Techniques

3.1 Transmission Electron Microscopy

The setup of a conventional TEM is similar to that of an optical microscope, but instead of visible light and optical lenses a beam of electrons and magnetic lenses are used. This exchange enables the TEM to reach a much higher resolution than optical instruments down to 140 pm. By using additional aberration correctors it can be enhanced to 80 pm [31]. Figure 3.1 shows the building of a conventional TEM in detail.
The electron gun consists of a cathode made of tungsten or LaB_6 and an anode, the potential difference between them accelerates the electrons towards the condenser with condenser lens and aperture, which focuses the beam onto the sample. This focusing maximizes the contrast and avoids thermal pollution of not investigated sections of the sample. The sample itself is fixed on the nitrogen cooled sample holder, which can be tilted up to $\pm$ 80° in relation to the beam direction. This tilt is useful for setting the eucentric height and for High Resolution TEM, see below. The magnification and imaging are performed by diffraction objective and lens, intermediary and projection lens in one of the three imaging modes: bright-field imaging, dark-field imaging and stray field imaging. These modes are described in more detail in [32].

3.1.1 Grain Size Estimation from TEM Images

In transmission electron microscopy thin foils of sample material are investigated. Therefore the sample material is cut into a lamella (see chapter 3.1.4) and only the grains cross-sections can be imaged.

Assuming a perfectly spheric grain shape with grain centers randomly distributed in the material and a negligible lamella thickness compared to the grain sizes, Swedish mathematical statistician S.D. Wicksell elucidated [80] two sampling effects: Firstly,

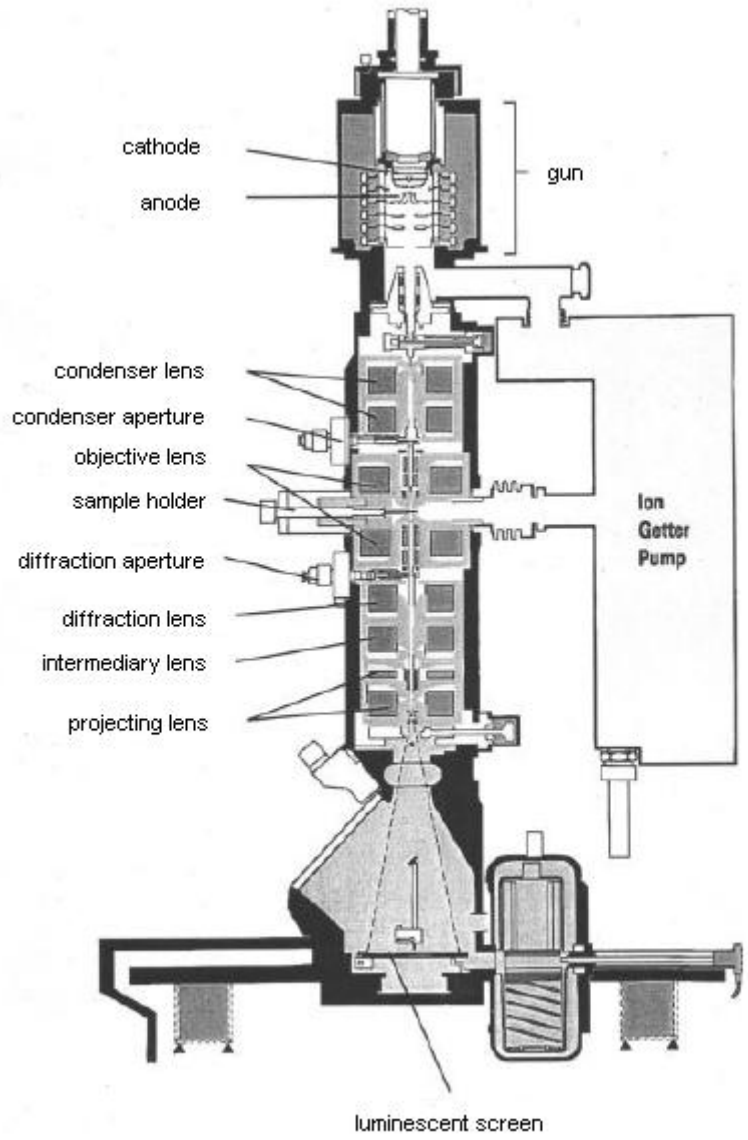

Figure 3.1: Schematic representation of the main components and pathways of the electron beam in a modern transmission electron microscope [33].

spherical grains are hit by the lamella with probability proportional to their diameters. Thus the diameters of grains selected by the lamella follow the size-weighted distribution

$$F_1(t) = \frac{1}{\mu} \int_0^t s dF(s) \tag{3.1}$$

where $\mu = \int_0^\infty t dF(t)$ is the mean grain diameter in the original sample material.

Secondly, given that a spherical grain of diameter t is cut by the TEM lamella, it yields a circular TEM image profile of diameter

$$s = \sqrt{t^2 - 4d^2} \tag{3.2}$$

where d is the distance from the centre of the sphere to the lamella plane. The distance d is conditionally uniformly distributed from 0 to $t/2$ with a probability density

$$f(d) = \begin{cases} 2/t & where \quad 0 \leq x \leq \frac{t}{2} \\ 0 & else. \end{cases} \tag{3.3}$$

Thus, the conditional distribution function of circular profile diameter s given a spherical grain diameter t is

$$H(s|t) = 1 - \sqrt{1 - \frac{s^2}{t^2}}\,;\ 0 \leq s \leq t \tag{3.4}$$

with conditional probability density

$$h(s|t) = \frac{s}{t\sqrt{t^2 - s^2}}\,;\ 0 \leq s \leq t. \tag{3.5}$$

Combining these two sampling effects, the observed distribution of circular profile diameter has the probability density

$$g(s) = \frac{s}{\mu} \int_s^\infty \frac{1}{\sqrt{t^2 - s^2}} dF(t). \tag{3.6}$$

By inverting the integral equation (3.6), F is given explicitly in terms of g and μ:

$$F(t) = 1 - \frac{2\mu}{\pi} \int_t^\infty \frac{g(r)}{\sqrt{r^2 - t^2}} dr. \tag{3.7}$$

Assuming that there are no particles of zero diameter, it follows $F(0) = 0$ and by inserting $t = 0$ in (3.7):

$$\mu = \frac{\pi}{2} \left[\int_0^\infty \frac{g(s)}{s} ds \right]^{-1}. \tag{3.8}$$

Hence, the mean particle diameter μ is related to the harmonic mean of the profile diameter μ_{harm} by

$$\mu = \frac{\pi}{2}\, \mu_{\text{harm}}. \tag{3.9}$$

Wicksell's evaluation gives only an upper estimate of the real particle size. His assumption, that the lamella thickness is negligible compared to the particle size, is questionable in case of TEM lamellas of nanocrystals, where the lamella thickness ($\approx$ 50 nm) equals the particle size ($\approx$ 50 nm). Additionally the grain shapes investigated in the present study is not perfectly spheric. There is a tendency to a columnar microstructure (compare fig. 4.9 in chapter 4). Hence, in the following we will give the grain size as the arithmetic mean of the grain size distribution estimated from the TEM images.

3.1.2 High Resolution Transmission Electron Microscopy

The High Resolution TEM is used to identify the sample's atomic planes using lattice mapping. Therefore, after passing the specimen the diffracted beam is recombined with the centric electron beam. Thus, an interference pattern is generated. The structural information can be obtained, if several diffracted beams interfere. Using the Scherzer focus as defocus one achieves the largest pass band of the contrast transfer function and therefore the crystal structure is reproduced in facsimile best [32].

3.1.3 FEI Titan 80-300

The *FEI Titan 60-300* with Cs-correction enables studies in STEM mode with a focused probe or in TEM mode with a parallel beam with 80 pm spatial resolution. The system is able to work in TEM, STEM, energy filtered TEM (EFTEM),

diffraction and electron energy loss spectroscopy (EELS) and energy dispersive X-ray spectroscopy (EDS) mode. The flexibility of operating the *Titan 60-300* in the acceleration voltage range of 60 to 300 kV allows to investigate a broad variety of materials, from ultra-light carbon compounds to ultra-dense heavy metal materials [31]. For the Pd and PdAu films an accelerating voltage of 300 kV was used always.

Electron tomography can be used to generate a 3D representation of even complex three-dimensional structures like highly porous foams with a spatial resolution of $1 - 2$ nm. This technique can also be employed to quantitatively measure e.g. particle distributions, surface areas and faceting.

In-situ investigations can be performed using an in-situ straining holder or an in-situ heating holder (up to 900° C) [34].

The statistical analysis was done using the software packages *Digital Micrographs (Version 3.9.5, Gatan Company)* and *ImageJ (Version 1.42q, Wayne Rasband, National Institutes of Health, USA)*.

3.1.4 Preparation of TEM Lamellas

Two different techniques were applied to prepare the electron transparent TEM specimens. On the one hand cross-sectional lamellas of undeformed films were cut using the focused ion beam technique (FIB) and on the other hand in-plane samples of deformed and undeformed films were prepared by conventional dimpling and a precision ion polishing system (PIPS).

Focused Ion Beam

The focused ion beam technique uses a focused gallium ion beam to scan the sample surface and image it. At higher operating voltages it can also be employed to sputter the surface atoms and cut predefined structures into the material. On the other hand by using precursor gases it can also be used to locally deposit C, Pt or W.

In this work a *FEI Strata Dual Beam FIB* was employed, which is a combination of a scanning electron microscope (SEM) and a FIB system, with the possibility of imaging and structuring the nanoscale material in parallel, which allows optimum control of the preparation process [34].

To prepare the Pd and PdAu lamellas on polyimide substrates, the film surface is initially covered with a thin C film and a 50 - 100 nm thick Pt film on top to prevent

ion damage in the film structure during cutting. After that a cross-sectional slice is cut out using the Ga^+-ion beam and lifted out in-situ for final thinning to about 50 nm thickness using a low Ga^+-ion current of 5 kV.

Dimpling and Precision Ion Polishing

The conventional way to prepare in-plane TEM specimen is a combination of dimple grinding and precision ion polishing: by dimple grinding the samples are mechanically pre-thinned from the substrate side. Therefore, the films were glued onto the sample holder by *Tesa Posterstrips* covered with tissue in the central part to protect the surface. The backside was covered with diamond polishing paste with 3 μm particle size. After about 30 min polishing with a *Gatan Dimple Grinder (Model 656)* the polyimide was fully removed in the center of the sample (1 - 2 mm diameter). This part was cut out and clamped into a Cu TEM folding grid with 50/50 mesh and holes 450 μm square to avoid sample bending during polishing.

A precision ion polishing system *Gatan PIPS (Model 691)* is used for final polishing of the metal films. It is a low angle polishing system with high milling rates. The system is equipped with two miniature Penning ion guns to deliver powerful and stable Ar^+-ion beams, the tilt angles range from 1° to 10° and can be varied independently. During polishing the sample is rotated to avoid preferential thinning [35]. The Pd and PdAu films were placed into the PIPS with the surface up and polished from the bottom with 10° tilt angle at both sources with accelerating voltage of 2.5 kV and about 10 μA. The polishing was stopped after a small hole appears in the sample, at its edges the film was electron-transparent.

3.2 Scanning Electron Microscopy

The scanning electron microscope (SEM) is a type of electron microscope that images the sample surface by scanning it with a high-energy beam of electrons in a raster scan pattern. The reflected (or back-scattered) electrons are collected and then displayed at the same scanning rate on the PC screen. The brightness contrast of the image represents the surface features of the specimen. The surface must be conductive, in case of nonconductive materials a very thin metallic surface coating must be applied. Magnifications range from 10 to 50,000 times and very deep field depths are possible [4].

3.2.1 Energy Dispersive X-ray Spectroscopy

Using the SEM the sample is shelled with a high energetic, focussed electron beam, which knocks out the electrons of the sample's atoms' inner shells. The resulting holes decay via an X-ray process in substance. During this process γ-quanta are created, which have a material specific energy. The energy dispersive X-ray spectroscope (EDX) is used to detect those quanta. The X-ray spectra have characteristic peaks, which enable the user to identify the involved elements. The present EDX is operated with a detection area of 100 nm to 1 μm radius.

3.2.2 Applied Instruments

A *Zeiss Leo 1530 Gemini* scanning electron microscope was applied for the investigation of undeformed and deformed samples. The electron gun was operated at 5 kV and a working distance of 3 mm was used. The instrument is also equipped with an EDX unit, which was used to determine the Pd and Au concentrations in the PdAu alloys.

3.3 X-ray Measurements

To characterize the samples' structure, composition, stress state, texture and film thickness several types of X-ray measurements were performed. XRD measurements give information about the crystalline structure, composition, grain size and texture. Residual stress measurements ($\sin^2\psi$ measurements) quantify the internal stress state of the films. Texture measurements deepen the knowledge of texture effects. In addition, using XRR measurements one obtains the sample's film thicknesses and surface properties.

Within the scope of this thesis a *Bruker D8 Discover* with Eulerian cradle was used. The diffractometer is configured horizontally and the circle diameter can be set inbetween 380 and 760 mm. The angular 2 Θ range spreads over -110° to 169° with minimum step size 0.0001°. The maximum scan speed is 30°/min and the parameters of the Eulerian cradle are:
-3°$\leq \chi \leq$ 94°; -$\infty \leq \varphi \leq +\infty$; -75 mm $\leq$ x, y $\leq$ 75 mm; -1 mm $\leq z \leq$ 12 mm.
The sample holder contains a vacuum chuck for wafers up to 3". Additionally, the diffractometer includes a Göbel mirror on the diffracted beam side and a Ge 022 analyzer crystal for Cu radiation.

The X-ray tubes contain a Cu anode, which emits Kα_1 radiation with a wavelength of 0.1540562 nm. The maximum voltage is 60 kV with an additional resistance of 50 kΩ. The heater voltage is 11 V and the heater current 3.8 A [36]. The X-ray tube is running at 40 kV and 40 mA by default.

3.3.1 X-ray Diffraction

When X-rays hit the sample's surface at larger angles of incidence among other things coherent scattering occurs. This is a perfectly inelastic collision between photon and electron and can be visualized as the electrons being reflected from the crystal's planes. Constructive interference can only occur, if all the waves scattered at a set of parallel planes come out in phase. This is equivalent to a difference in the optical path of multiples n of the wavelength λ. The optical path conforms:

$$(A + B) = n\lambda = 2d \ \sin\Theta \tag{3.10}$$

with A and B being the difference in incoming path length and emerging path length, respectively; d is the lattice spacing and Θ the angle of incidence, see also figure 3.2. Equation (3.10) was derived by W. L. Bragg in 1912 and is therefore named Bragg's law [37]. In practice the spacing d depends on the observed crystal direction named (hkl) and is for cubic lattices related to the lattice constant a by the following formula [38]:

$$d_{hkl} = \frac{a}{\sqrt{h^2 + k^2 + l^2}} \tag{3.11}$$

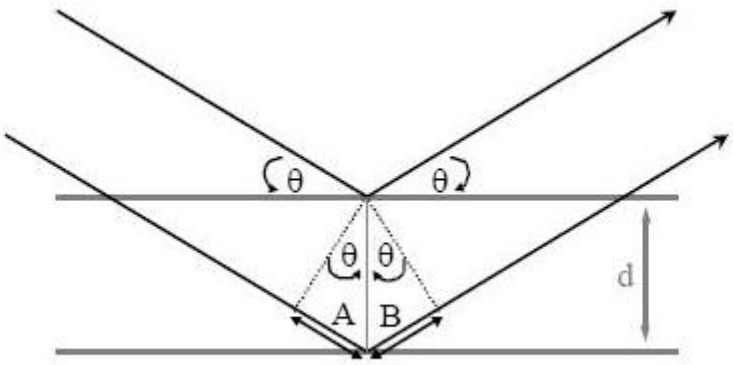

Figure 3.2: Bragg's law for parallel planes with spacing d [37].

In conclusion the position in terms of the angle of incidence of the Bragg peak provides information about the scattering lattice direction and the lattice constant.

Grain Size Analysis

The peak shape is related to grain size and texture. In a first approximation the relation between the full width at half maximum (FWHM) and the grain size (τ) is given by the Scherrer equation [37]:

$$\tau = \frac{K\lambda}{\sqrt{FWHM}\ \cos\Theta} \tag{3.12}$$

Here the FWHM is given in radians, K is the so-called shape factor, which is 0.9 for cubic structures, λ is the wavelength of the X-rays and Θ is the angle of incidence.

Having a closer look to the peak broadening one observes several effects contributing to the peak broadening: grain size, microstrain and machine broadening. The so-called "machine broadening" is related to the instrumental parameters influencing the peak shape. These are the beam characteristics, like wavelength and beam focussing, and the instrumental optics, like convergence slits, monochromators etc.

In 1969 Hugo Rietveld described the diffraction profile as a mathematical convolution of instrumental and sample characteristic functions [81]. The method is called Rietveld analysis or "whole-pattern-fitting structure refinement", because in contrast to the pure profile refinement fitting routines the primary structure parameters are refined and not the line profiles.

Though these functions are not necessarily of Gaussian shape, their convolution is of Gaussian shape. Rietveld fitted the resulting convolution function to the experimental peak profile using the least-squares method, which minimizes the squared differences of calculated parameters and experimental parameters. Therefore, the instrumental parameters have to be determined carefully.

The instrumental parameters can be derived from measurements with standard powder samples, e.g. LaB_6. The measured peak profile is fitted by a convolution of Gaussian, Lorentz and Hat functions. The resulting function is used for further convolution with the sample characteristic function to determine the sample parameters like grain size and microstrain.

The software *Topas (Version 3.0, Bruker AXS)* based on the Rietveld analysis was used for XRD simulations and analysis. This software allows fitting of the instrumental function to the peak profile of the standard sample. The resulting instrumental function and the measured profile are fitted using fundamental atomic parameters to determine the grain size and microstrain of the investigated sample.

3.3.2 Residual Stress Measurements

Residual stresses are related to forces and moments, which are in equilibrium within the material. Elastic and/or plastic deformation which are inhomogeneously distributed over the sample volume induce these stresses. Three types of residual stresses have been classified: first, second and third order [39]. This definition has been extensively used in the field of X-ray stress analysis and is related to the microstructure of crystalline materials.

- First order residual stresses - also called macroscopic residual stresses - are in equilibrium within the whole sample volume and constant over several grains. Stress relieve methods (e.g. hole drilling method or curvature measurement method) could also be used to measure these type of stresses.
- Second order residual stresses are constant within one crystal grain and compensated over a few grains. They result typically from differences in elastic and plastic behavior and thermally activated grain growth of single grains of a polycrystalline material.
- Third order residual stresses are usually induced by crystal lattice defects like substitution or implantation of atoms or dislocations. Hence, they vary on an atomic scale and are compensated for within one grain.

In X-ray diffraction analysis macroscopic residual stresses result in a peak shift of the diffraction lines. The method described here evaluates macroscopic residual stresses.

The 2nd- and 3rd-order residual stresses, often also called microscopic residual stresses, can be evaluated by X-ray methods based on shape and/or width of the diffraction lines.

The angles ϕ and ψ of the normal of the lattice planes describe the orientation of the examined lattice planes with respect to the external sample coordinate system. The non-strained lattice spacing (d_0) is changed by residual stresses. Thus, the angular shift of the diffraction lines can be used to determine the lattice strain:

$$\epsilon_{\phi\psi} = \frac{d_{\phi\psi} - d_0}{d_0} = -(\Theta_{\phi\psi} - \Theta_0)\ \cot\ \Theta_0 \tag{3.13}$$

The reliability of the measurements and their sensitivity to the exact d_0-value can be enhanced by recording a lattice strain distribution instead of just one strain component. This strain distribution is determined at different angles ϕ within the sample

surface area and additionally at different tilt angles ψ within an area perpendicular to the sample surface.

For a homogeneous macroscopic stress state within an elastically isotropic volume and assuming a plane-stress state in single-phase materials due to the small penetration depth of the soft X-rays used in XRD (about 5 μm in steel), the relationship between the strain components $\epsilon_{\phi\psi}$ measured via diffraction at angles ϕ, ψ and the stress components σ_{11} and σ_{22} is given by the theory of linear elasticity:

$$\epsilon_{\phi\psi} = \frac{1}{2}\, s_2\, \sigma_\phi\, \sin^2\psi + s_1[\sigma_{11} + \sigma_{22}] \tag{3.14}$$

This is the basic equation of the well known $sin^2\ \psi$-method [40] which evaluates the stress component σ_ϕ and the sum of the principal stresses σ_{11} and σ_{22} by a linear fit of the σ_ϕ-distribution. With

$$s_1 = -\frac{\nu}{E}, \quad \frac{1}{2}\, s_2 = \frac{\nu+1}{E}, \tag{3.15}$$

where ν = Poisson's ratio and E = Young's modulus.

For measurement and evaluation of the macroscopic residual stress states in the Pd and PdAu films the software packages *Edstress (Version 1.1., Bruker AXS)* and *Stress (Version 1.1, Bruker AXS)* which are based on the $sin^2\ \psi$-method were applied.

3.3.3 X-ray Reflection

In comparison to XRD, XRR is a much more surface sensitive method. A Θ-2Θ-scan is performed in both cases, but for XXR the angle range is much smaller: $0.1^\circ \leq \Theta \leq 10^\circ$. In this case the incoming beam is reflected and not scattered, because the interatomic distances are much smaller than the fracture of wavelength and the sine of the angle of incidence.

The XRR pattern is characterized by the critical angle Θ_c, below this angle the reflection is nearly constant, that is the region of total reflection, and the penetration depth is around 5 nm. Above Θ_c the intensity decreases, the decay is nearly proportional to Θ^{-4} for perfect smooth interfaces. At some point the transmission is equal to one, the X-rays penetrate unimpeded into the medium. The penetration depth

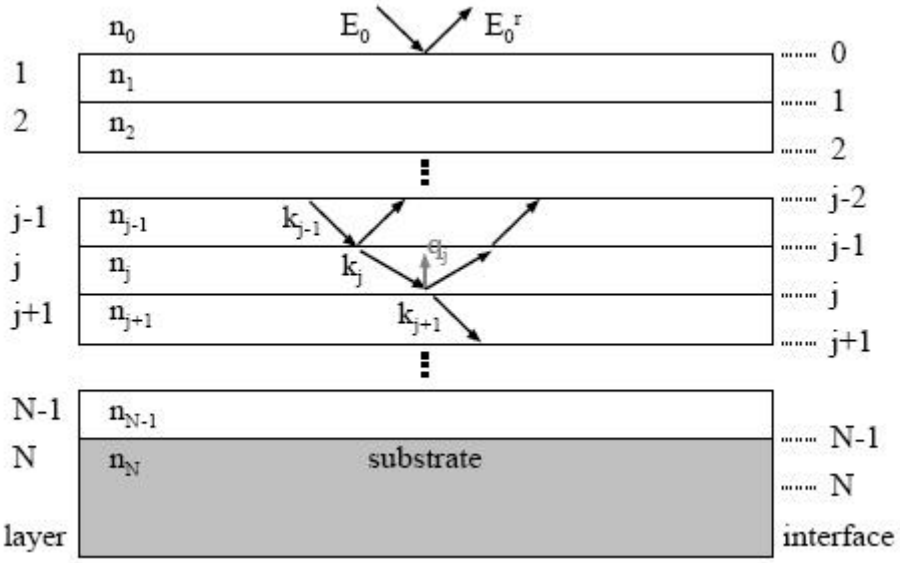

Figure 3.3: Scheme of reflection and transmission of X-rays at a multilayer [37].

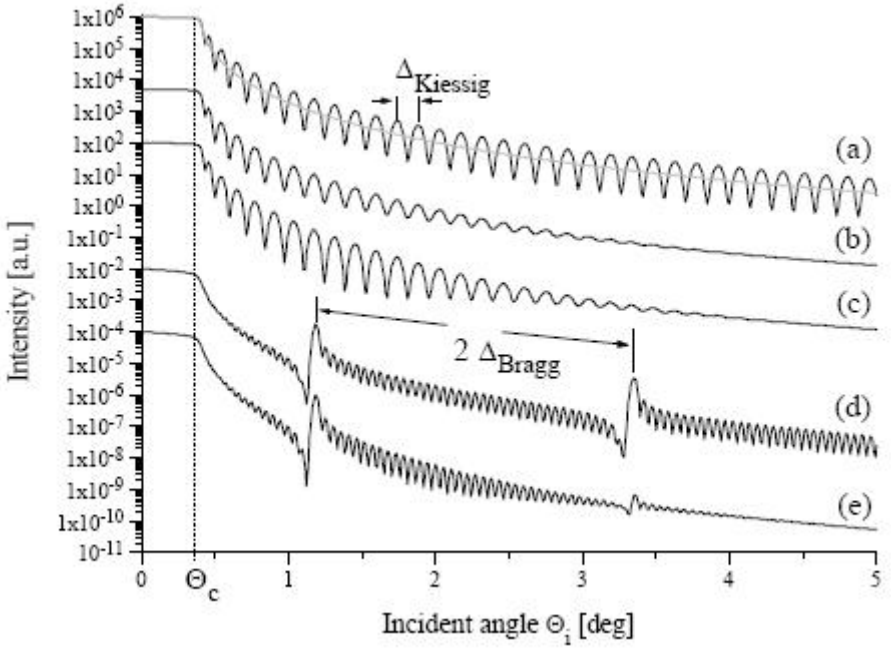

Figure 3.4: Calculated reflectivities: (a)-(c): Monolayer on Si substrate. (a) Neither surface nor interface roughness. (b) Rough interface but smooth surface. (c) Smooth interface but rough surface. (d) Multilayer with smooth interfaces. (e) Multilayer with rough interfaces [37].

increases rapidly to many microns for $\Theta \geq \Theta_c$. The critical angle is determined via the law of diffraction and due to this it is very sensitive on the density of the material [37].

Concerning thin film samples, many interfaces have to be taken into account, see figure 3.3. We consider a stack of N single layers including the substrate. The thicknesses are denoted as d_j and the refractive index as n_j for the j-th layer. The influences of all those layers are integrated recursively beginning from the substrate. Including finite substrate roughnesses, the pattern varies from the Θ^{-4}-shape. One obtains fringes, namely Kiessig fringes and Bragg fringes, see figure 3.4. The Kiessig fringes are due to the interference of waves scattered from the sample's surface and from the interface to the substrate, that is the whole sample's thickness. For small angles the positions of these fringes can be calculated out of the Bragg equation including the influence of refraction:

$$\Theta_{im}^2 - \Theta_c^2 = m^2 \left(\frac{\lambda}{2d}\right)^2 \tag{3.16}$$

with Θ_{im} being the fringe of order m, Θ_c the critical angle, λ the wavelength and d the sample's thickness.
The Bragg fringes belong to the interference of waves scattered from the single multilayer interfaces, that is the layer thickness of one single layer. Their positions can be calculated similarly to that of the Kiessig fringes:

$$\Theta_{im,Bragg}^2 - \Theta_c^2 = m^2 \left(\frac{\lambda}{2d}\right)^2 \tag{3.17}$$

with $\Theta_{im,Bragg}$ being the fringe of order m, Θ_c the critical angle, λ the wavelength and d the layer thickness.

The patterns are interpreted using *LEPTOS*, a software provided by *Bruker* that allows simultaneous fitting of film thickness and roughness even for complex samples [36]. This technique has been used to measure the thickness of thin (5 - 20 nm) sputtered films of one element to adjust the sputtering rates prior to sputtering thick (1 μm) films.

3.4 Mechanical Testing

The knowledge of the mechanical properties of a material is important to a variety of parties having different interests. Consequently, the consistency in the way the tests are conducted, and the interpretation of their results is of significant importance [4]. The most common mechanical stress-strain test is performed in tension. Since these tests are difficult to execute in case of thin films, nanoindentation tests were used to verify the tensile tests results.

3.4.1 Tensile Testing

Tensile tests are the standard mechanical tests to determine material properties that are important in product design. A gradually increasing uniaxial tensile load is applied along the long axis of the specimen which is deformed usually until it fractures. The standard tensile specimen is shaped like a "dogbone", that means it has a narrowed center region, to restrict deformation to this region and reduce the probability of fracture at the ends of the specimen. The specimen is fixed into the holding grips of the tensile tester by its ends. The tensile test is performed at a constant deformation rate, and the instantaneous applied load as well as the resulting elongations are continuously and simultaneously measured by a load cell and an extensometer, respectively. A stress-strain test typically takes several minutes to hours to perform and is destructive [4].

For testing the thin films in this work at room temperature a dedicated tensile stage for miniature specimens was applied. The tensile tester was equipped with a special thin film sample clamping to avoid sample deformation during mounting of the delicate thin films. The thin film sample clamping as shown in fig. 3.5 contains a stabilizing part, that is screwed to the backside of the holding grips while the specimen is fixed into the clamping and afterwards removed. Two binder clips on each side of the gauge section connect the two holding grips and support the specimen while the sample holder is transferred to the tensile tester. After the sample holder is mounted into the tensile tester the system is pre-loaded without

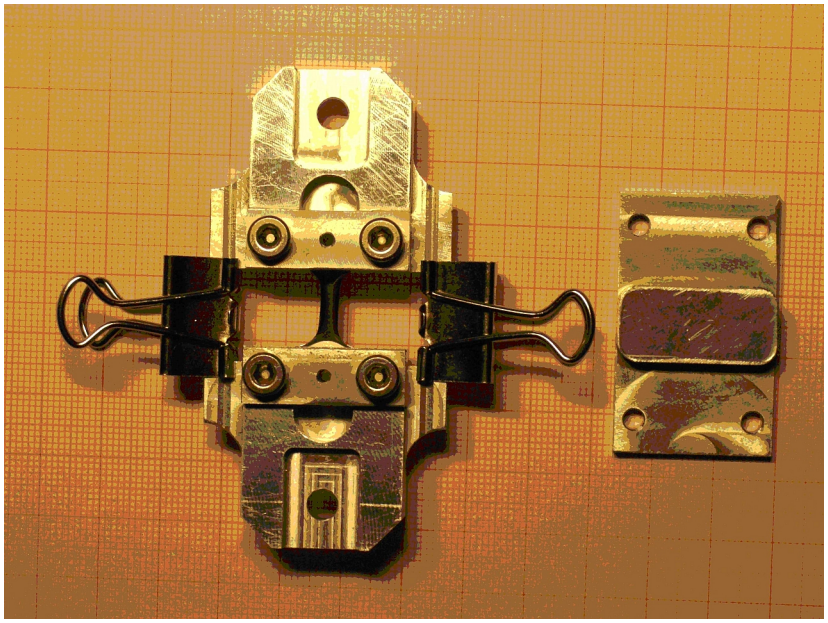

Figure 3.5: The special thin film sample clamping for mounting and tensile testing of delicate thin films.

applying load to the specimen. Finally the binder clips are removed to start the measurement.

The elongation was precisely measured using a *Laser Extensometer (Model P-50, Fiedler Optoelectronics)* to read glued white paper marks on the polyimide backside of the samples. Therefore the polyimide backside was painted black and two strip-shaped paper marks with 1 mm width were glued in the center part of the specimen. The initial distance between was approximately 6 mm. The laser extensometer detects the difference in contrast between the paper mark and the black polyimide. The distance between the two paper marks is than calculated automatically and expresses the true strain in the specimen.

Two different strain rates were applied: $5 \cdot 10^{-5}\mathrm{s}^{-1}$ and $2.5 \cdot 10^{-5}\mathrm{s}^{-1}$.

The samples were rectangular with a size of 5 mm by 30 mm. Samples with dogbone shape were not suitable due to trouble with cutting reproducible specimen with sharp edges. But due to the stress delocalization on the supporting substrates the samples did not fracture at the ends, which were clamped to the tensile tester.

3.4.2 Nanoindentation

Nanoindentation is an indentation hardness test especially applied to small volumes. Indentation is one of the most commonly applied methods to test the mechanical properties of materials. In a conventional indentation test (e.g. macro or micro indentation), a very hard tip with known mechanical properties (usually diamond) is pressed into the sample of the material to investigate. The load on the indenter tip is increased while the tip is pressed into the specimen until it reaches a user-defined value. At this moment, the tip may be removed or the load held constant for a defined period of time. The resulting indentation area in the sample is measured and the hardness is calculated as the maximum load divided by the residual indentation area.

Nanoindentation improves these macro and micro indentation tests by indenting on the nanoscale with a very precise tip shape, high spatial resolution to place the indents, and by providing real-time load-displacement (into the surface) data while the indentation is in progress. An indenter with a geometry known to high precision (usually a Berkovich tip, which has a three-sided pyramid geometry) is employed. During the course of the instrumented indentation process, a record of the depth of penetration is made, and then the area of the indent is determined using the known geometry of the indentation tip [42].

To investigate the mechanical properties of thin films, nanoindentation is a very fast and easy-to-use technique. A small sample is sufficient to perform a complete series of tests, with different strain rates and at least 100 indents per data point. The nanoindenter is even programmable and can test several samples without any user control needed. The results cited in this work were obtained by using a *NANO Indenter XP (MTS Nano Instruments)* with a displacement resolution of < 0.1 nm, maximum indentation depth > 500 μm, maximum load of 500 mN and load resolution of 50 nm [43].

For nanoindentation the films must be deposited on a hard substrate, therefore Si-Wafers of 500 μm thickness were used. To obtain reliable results the indentation depth should not exceed 10 % of the film thickness, but it should not be below 100 nm, to avoid surface effects. Hence, films with 1 μm thickness and more were preferred for nanoindentation tests [44].

3.5 Profilometry

A profilometer is a tool to measure sample surface roughnesses or step heights. It is based on a diamond profiler that scans in contact vertically across the sample surface. The stylus profiler is mechanically connected to the core of a Linear Variable Differential Transformer (LVDT). Surface variations result in a vertically translation of the stylus. This causes changes of the core position of the LVDT coupled to the stylus, which generates electrical signals, that are scaled to the sample height [47]. To produce reliable results the sample surface and substrate materials must be hard, because otherwise the stylus will penetrate into the material and cannot measure the surface features.

The technique was used to determine sputtered film thicknesses, by measuring the step height between substrate and film surface at edges that were covered with tape during sputter deposition. For these measurements a *Dektak Stylus Profiler (Model: Dektak 6M, Veeco Instruments)* was applied. Its vertical resolution scales with the different scan ranges (6.5 μm to 262 μm) from 0.1 nm to 4 nm, the maximum scan length is 50 μm and the stylus tracking force is programmable between 1 and 15 mg [47]. For the sputtered metal films on Si substrate the force was set to 5 mg.

3.6 Scanning Tunneling Microscopy

Scanning tunneling microscopy (STM) is a powerful tool to image surfaces of conducting samples with atomic resolution. With this resolution, individual atoms

within material structures can be imaged and manipulated. The STM is not restricted to ultra high vacuum (UHV) but can also be operated in various media like air, water, or other liquid or gas ambients. Additionally, temperatures ranging from near zero Kelvin to a few hundred degrees Celsius are possible.

The technique is based on the quantum tunneling effect: if a small conducting tip is brought close to the sample surface and a small bias voltage is applied, electrons can tunnel through the vacuum between surface and tip. The resulting tunneling current is detected as a function of tip position, applied voltage, and the local density of states (LDOS) of the sample. By scanning across the sample surface and monitoring the current and the tip's position the surface information is acquired and usually displayed in 2D or 3D image form [45].

Within this thesis an *Omicron UHV-AFM/STM* was applied. The system is part of an UHV cluster which also contains the magnetron sputtering system. Therefore, in-situ microscopy of the prepared films was possible without breaking the vacuum conditions. The system combines various STM and atomic force microscopy (AFM) measurement modes including contact mode AFM with simultaneous lateral force (friction) detection and non-contact mode AFM in a single instrument. The systems resolution in z-direction is 0.01 nm or better (STM mode) with a force resolution of $3 \cdot 10^{-12}$ N or better [46].

3.7 Rutherford Backscattering Spectroscopy

Rutherford backscattering spectroscopy (RBS) is a technique used to determine the structure and composition of materials by measuring the backscattered particles of a beam of high energy ions penetrating a sample. An elastic collision process can be used to describe the process. Elastic means here that during the collision between the high kinetic energy particle from the incident beam and the stationary particle located in the sample no energy is either lost or gained. Considering this energy conservation, the energy E_1 of the scattered particle is reduced from the initial energy E_0:

$$E_1 = k \cdot E_0, \tag{3.18}$$

where k is known as the kinematical factor, which depends on the scattering angles and the masses of the particles.

Two different processes can cause the energy loss of a backscattered ion: the energy loss due to scattering events with the sample nuclei, and the energy loss due to small-angle scattering processes with the sample electrons. The first process depends on the cross-section of the nucleus, which is related to its mass and atomic

number. Therefore, at a given measurement angle, two different elements will scatter incident ions to different degrees and with different energies, which will result in two separate peaks on a plot of measured counts versus energy. These peaks can be used to analyze the sample composition, because they are characteristic of the elements contained in the material. The peak heights are proportional to the relative concentrations. The second process creates a gradual energy loss which depends on the electron density and the distance travelled in the sample [48]. Hence, the sample depth can be determined from the width and shifted position of the peaks. Therefore, to investigate only the sample composition, films of only 10 to 20 nm thickness would be best.

The measurement set-up used contains an ion source, in this case alpha particles (He^{2+} ions), a linear particle accelerator capable to accelerate the ions to more than 2 MeV, and a silicon surface barrier detector to detect the scattered ions.

3.8 X-ray Photoelectron Spectroscopy

X-ray photoelectron spectroscopy (XPS) is a quantitative spectroscopic technique to determine the elemental composition, empirical formula, chemical state and electronic state of the elements within a material. The material of interest is irradiated with a beam of X-rays and simultaneously the kinetic energy and number of electrons that escape from the top 1 to 10 nm are measured. Therefore UHV conditions are required.

A typical XPS spectrum is a plot of the number of electrons detected versus their binding energy. A characteristic set of XPS peaks at certain binding energy values is produced by each element which identifies the sample's surface elements. The amount of the element within the irradiated volume is directly related to the number of electrons in its characteristic peaks [49].

Within this thesis a *SPECS XPS System* was applied. The system is part of an UHV cluster which also contains the magnetron sputtering system. Therefore, in-situ spectroscopy of the prepared films was possible without breaking the vacuum conditions. The SPECS system contains an analyzer suitable for XPS and ultraviolet photoelectron spectroscopy (UPS) with five channeltron detectors [50]. Spectra were collected overnight to increase the accuracy. Hence, the detection limit is in the parts per million (ppm) range.

4 Microstructure and Residual Stress of Magnetron Sputtered Pd and PdAu Films

In this chapter the structural properties and residual stresses of 500-nm-thick nanocrystalline Pd and PdAu films on compliant substrates prepared by magnetron sputtering as a function of the pressure of the Ar-sputtering gas are reported. Films were analyzed by X-ray diffraction, cross-sectional transmission electron microscopy and X-ray photoelectron spectroscopy. At low pressures the metal films exhibit strong compressive stresses, which rapidly change to highly tensile with increasing pressure and then gradually decrease. Along with this effect a change in microstructure is observed from a dense equiaxed structure at low pressures to distinctive columns with reduced atomic density at the column walls at higher pressures. The preparation of nearly stress-free dense nanocrystalline films is demonstrated.

4.1 Introduction

Thin metal films on compliant substrates are important components in electronic applications such as flexible displays [51, 52], wearable electronics [53, 54], electronic skins [55] and flexible solar cells [56]. In all of these applications, the composite material has to withstand variable mechanical stresses. While the polymeric substrate usually deforms elastically even at large strains, the metal deforms plastically, which can result in cracking or delamination. The resulting mechanical failure is one of the most critical issues in the development of metal-based flexible electronics [57]. Thin nanocrystalline (nc) metal films are promising candidates for this propose since it has been demonstrated that nc metals tolerate high mechanical stresses and high strains [7].

It has been shown that sputtering is a powerful technique for the deposition of thin films and it has been successfully applied for the production of nanocomposites with fine alternating layer structures (< 100 nm), such as Cu/Zr, Ni/Cu, and Ag/Cu

alloys [58]. To adapt this processing technique to only one metal, the deposition is repeatedly interrupted after deposition of a certain layer thickness by the action of a shutter. Using this interrupted deposition, often referred to as multilayer sputter deposition, pure Cu films have been prepared maintaining the nanocrystalline grain sizes even at thicknesses of several micrometer [18]. Moreover, it was shown that the resulting films are dense, exhibit nanocrystalline grains and have a low impurity level. In contrast, other synthesis techniques, such as inert gas condensation, exhibit additional defects, such as pores and impurities, which cause mechanical failure in tensile deformation. Furthermore, the study of alloying effects on the mechanical properties is much easier, as the composition can be changed easily by using co-deposition from multiple sources. Therefore, these thin film structures beneficial for the study of mechanical properties are employed in this work.

Thin films prepared by magnetron sputtering exhibit residual stresses as was reported by Thornton and Hoffmann [59]. The film stresses depend strongly on the sputtering parameters used for deposition and can have compressive as well as tensile nature. The residual stresses alone can already lead to cracking and/or spalling of the deposited film even without application of additional mechanical stresses for testing purposes [60]. Residual stresses consist of two components: thermal stresses, caused by the different thermal expansion coefficients of the substrate and the metallic film, and intrinsic stresses. A strong relationship between stresses and working gas pressures, gas type, the atomic mass of the sputtered material, as well as the geometry of the sputtering chamber has been reported [61].

The goal of the present chapter is to investigate the effect of different sputtering pressures on the residual stresses and microstructure in the films for radio-frequency magnetron (RF) sputtered Palladium and PdAu films with 10 at.% Gold [17]. For the mechanical tests, such as tensile deformation, it is important to reduce the residual stresses in the as-prepared films as much as possible. Stress-free thin films will be good candidates for the tests of the mechanical performance of the thin films as a function of grain size.

4.2 Experimental

Palladium and PdAu specimens were deposited by RF magnetron sputtering using two 2” diameter planar targets with 99.95% purity (Pd) and 99.99% purity (Au). To enable co-sputtering of two different elements, the two sources are facing the rotating sample manipulator at a distance of 150 mm at an angle of 20°, the rotational speed of the manipulator is 13.5 rpm. The geometry of the sputter sources is shown in fig. 4.1. Several pure Pd samples were prepared with constant sputtering power of 60

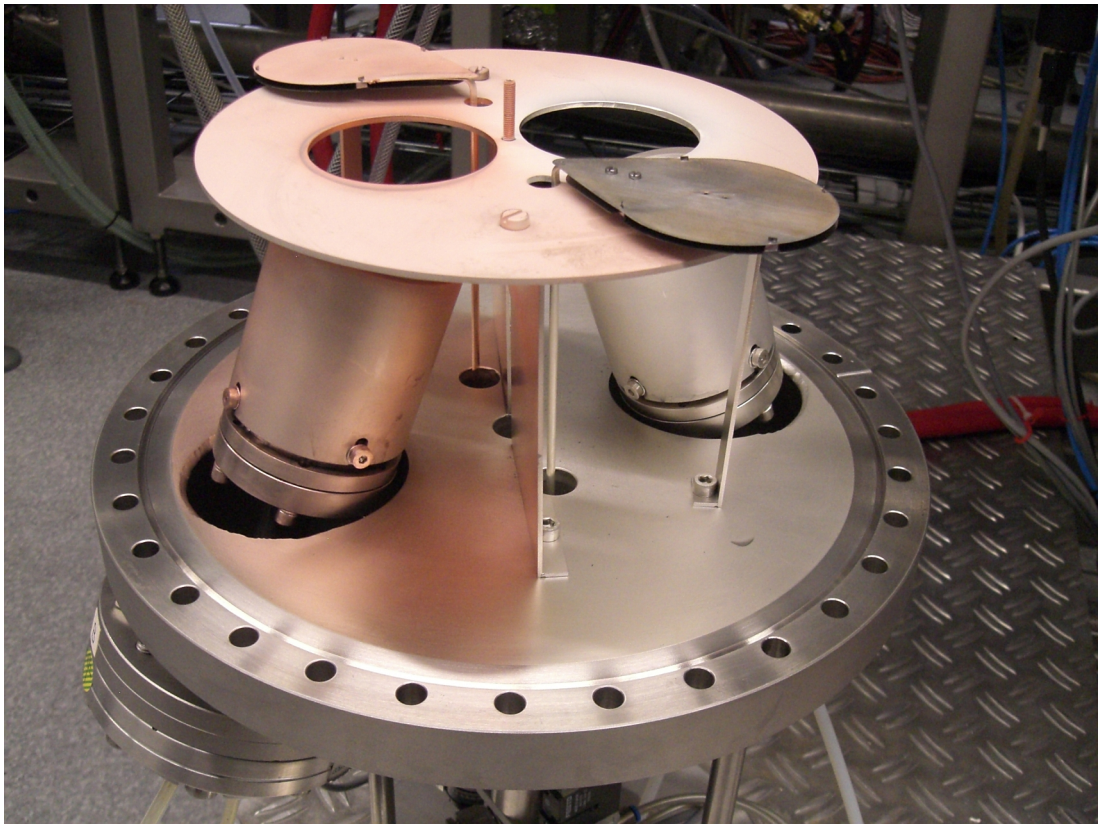

Figure 4.1: The two 2" sputter sources with rotational shutters of the home-built UHV magnetron sputtering system.

W, whereas the working gas pressure (Ar) was varied between 0.003 and 0.02 mbar. The resulting sputtering rate decreases from 0.21 to 0.12 nm/s, respectively. At room temperature 500 nm thick Pd films were grown in 50 steps of 10 nm thickness each interrupted for 10 s using a fast rotational shutter in front of the Pd-target. Additionally, 500 nm thick PdAu films were prepared by co-sputtering. In this case, both sources were operated simultaneously, the Pd target at 60 W and the Au target at 10 W, with an Ar working gas pressure varying between 0.005 and 0.02 mbar, resulting in a gold concentration of 10 at.% confirmed by energy dispersive X-ray spectroscopy (EDX).

Polyimide Kapton HPP-ST (Dupont) foil with a thickness of 25 μm was used as a substrate. Prior to the film deposition, the substrates were cut using a punch into a 'dogbone' shape with a total length of 30 mm, a gauge width of 3 mm and a length of 6 mm, the geometry of the specimen is sketched in fig. 4.2. Afterwards the sample surface was cleaned with methanol and dried with pressurized nitrogen. The samples were clamped onto special sample holders and transferred into ultrahigh vacuum of $2.0 \cdot 10^{-8}$ mbar in the sputtering chamber via a load lock system.

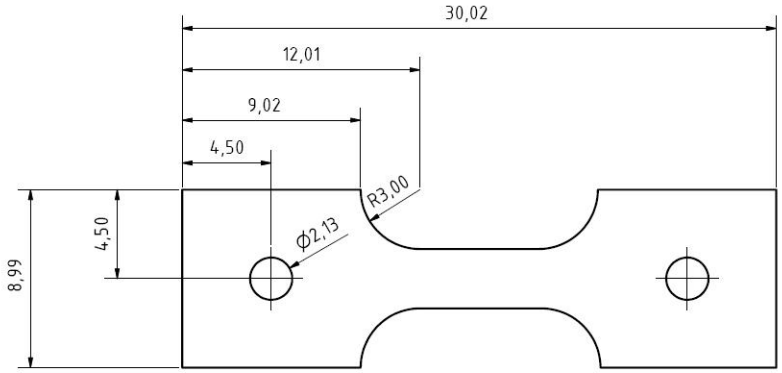

Figure 4.2: The geometry of the specimen, the length scale is mm.

The stress state of the metallic films on the flexible substrates can easily be detected by eye: films in compression and tension bent convexly and concavely, respectively. For all X-ray measurements, the samples were glued onto glass substrates in order to avoid the deformation (rolling) of the films. The quantitative determination of the stress state was performed using the X-ray $\sin^2\psi$ method in iso-inclination mode. The (311) peak was monitored for 13 different equidistant ψ-values between +40° and -40° and the residual stress was calculated by applying the theory of linear elasticity. Conventional Θ-2Θ XRD measurements (Bragg-Brentano) were performed using the Bruker D 8 Discover diffractometer to investigate the crystallographic texture and grain sizes, which were determined by fundamental parameter analysis using Bruker Topas 3.0 software. Cross-sectional TEM analysis was performed using a FEI Titan 80 - 300 with Cs-corrector operated at 300 kV. Specimens were prepared using the focused ion beam (FIB) technique (FEI Strata 400 STEM). The nominal sample thickness was approximately 50 nm with the final thinning performed with a low Ga^+-ion current at 5 kV. The surface roughness of the metal film was measured using an Omicron VT STM. XPS measurements were performed using a Specs system with an Al Kα and a Mg Kα anode.

4.3 Stress Measurements

In case of flexible substrates the only way to measure residual stress is by XRD using the $\sin^2\psi$ method. Other methods, like Stoney's equation, are not applicable as they depend on the curvature of the bare substrate, which is not constant for polyimides. Figure 4.3 displays the longitudinal residual stresses in the pure Pd films as a function of the pressure of the Ar-sputtering gas. For the lowest pressure (0.003 mbar) the Pd film exhibits a strong compressive stress of -327 MPa. With

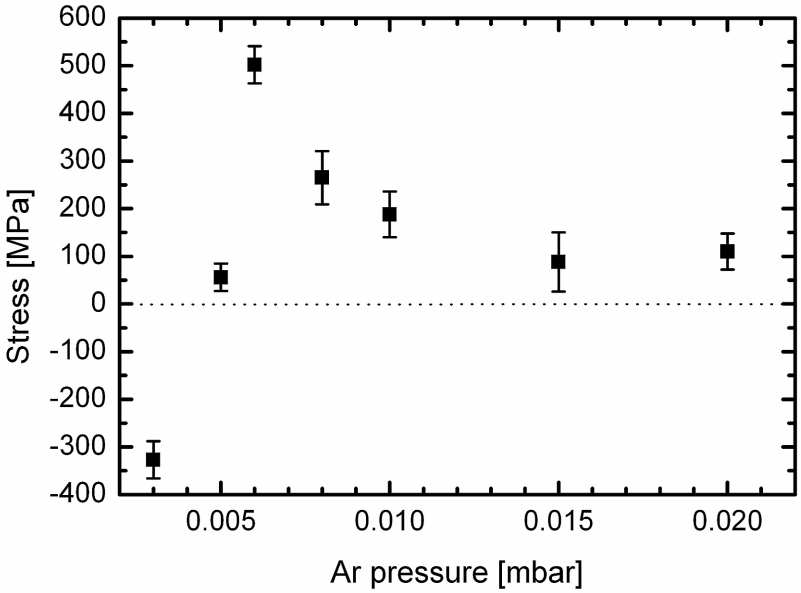

Figure 4.3: Stress measured using X-ray diffraction and the $\sin^2\psi$ method of sputtered Pd films with 500 nm thickness as a function of the pressure of the Ar-sputtering gas.

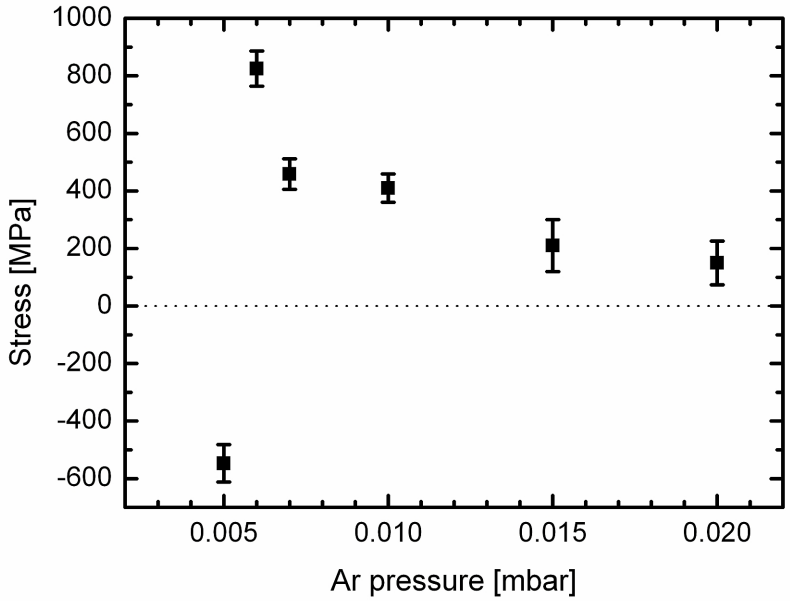

Figure 4.4: Stress measured using X-ray diffraction and the $\sin^2\psi$ method of sputtered PdAu films (with 10 at.% Au) with 500 nm thickness as a function of the pressure of the Ar-sputtering gas.

increasing Ar-pressure the stresses change rapidly from compressive to highly tensile, with a maximum stress of 502 MPa at 0.006 mbar. A further increase of the pressure results in a gradual decrease of the stress to 110 MPa at 0.02 mbar. In the transition zone between compressive and tensile stresses an almost stress-free [56 ± 29 MPa] Pd film at a pressure of the Ar-sputtering gas of 0.005 mbar was prepared.

A comparison of these results with the stress-pressure relationship in the PdAu films with 10 at.% Au (Fig. 4.4) shows the same trend. However, the stress minimum and maximum are more pronounced (-547 MPa at 0.005 mbar and 825 MPa at 0.006 mbar, respectively) and the transition between compressive and tensile stress is even steeper and shifted towards higher pressures.

4.4 Microstructural Characterization

The XRD measurements clearly show that the stress state and the microstructure of the films depend strongly on the pressure of the Ar-sputtering gas. In figure 4.5 typical Θ-2Θ scans are shown for the pure Pd films with a thickness of 500 nm as a function of the pressure of the Ar-sputtering gas. While the film sputtered at the lowest pressure (0.003 mbar) has a strong (111) texture, the extent of texture is decreasing with increasing pressure of the Ar-sputtering gas. A quantitative measure of the texture is the texture factor T_{hkl}, which is defined as:

$$T_{hkl} = \frac{I_{hkl}^{\mathrm{meas}} / I_{hkl}^{\mathrm{stat}}}{1/n \; \Sigma_{i=1}^{n} I_{hkl}^{\mathrm{meas}} / I_{hkl}^{\mathrm{stat}}} \tag{4.1}$$

with I_{meas} measured relative peak intensity, I_{stat} theoretical relative peak intensity for perfect powder samples, and n number of measured reflexes [62]. For T_{hkl} equal to unity, the sample is statistically oriented, for $T_{hkl} > 1$ a preferred orientation is present. Figure 4.6 displays the texture factor of the (111), (200), (220), and (311) reflexes of the pure Pd films. The (220) texture becomes more dominant with increasing pressure. Concurrently, the grain size decreases from 42 to 24 nm. The lattice parameter measured at 0.38950 nm does not change with the Ar-sputtering gas pressure and is slightly higher than the value of 0.38896 nm reported by Pearson [63].

In case of the PdAu solid solution films a highly (111) textured structure was only observed for the lowest sputtering pressure of 0.005 mbar (Figures 4.7 and 4.8). With increasing Ar-sputtering gas pressure the (220) component becomes more dominant. The grain sizes are decreasing from 48 nm at 0.005 mbar Ar pressure to 20 nm at

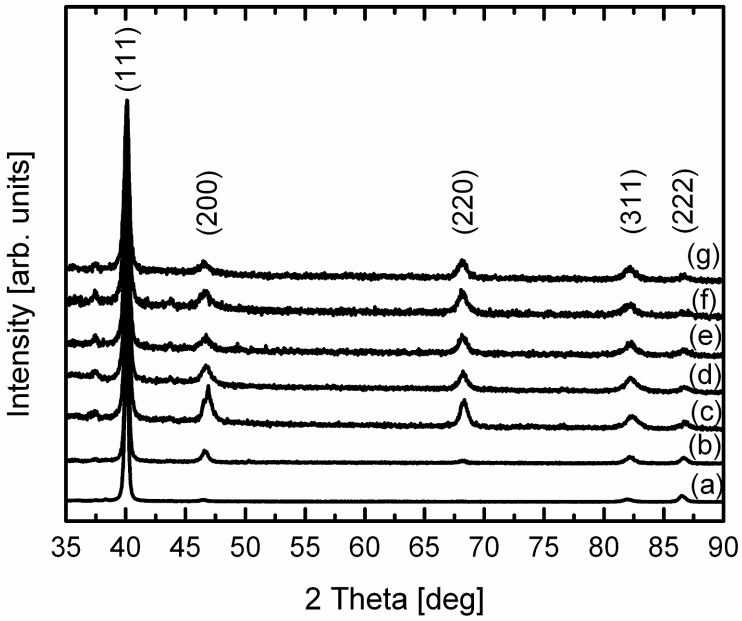

Figure 4.5: Evolution of the structure of pure Pd films with 500 nm thickness determined by X-ray diffraction as a function of the pressure of the Ar-sputtering gas: (a) 0.003 mbar, (b) 0.005 mbar, (c) 0.006 mbar, (d) 0.008 mbar (e) 0.01 mbar, (f) 0.015 mbar, and (g) 0.02 mbar.

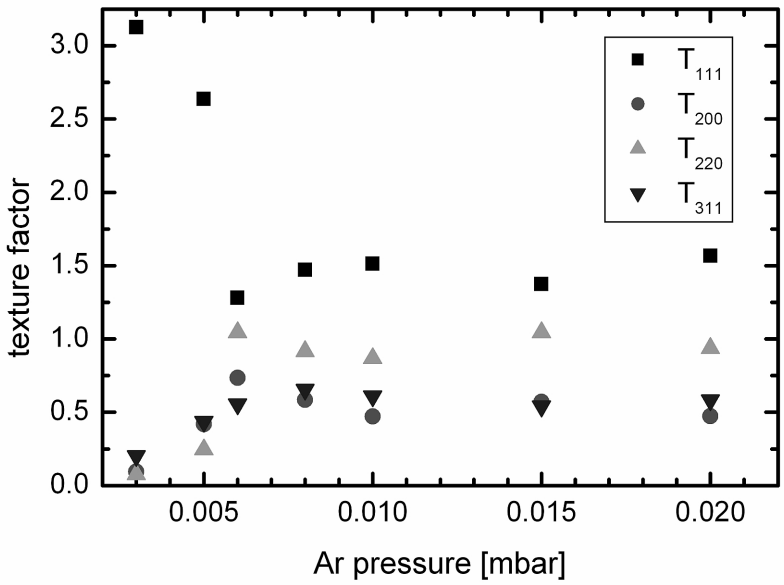

Figure 4.6: Texture factor of the pure Pd films with 500 nm thickness determined by X-ray diffraction as a function of the pressure of the Ar-sputtering gas.

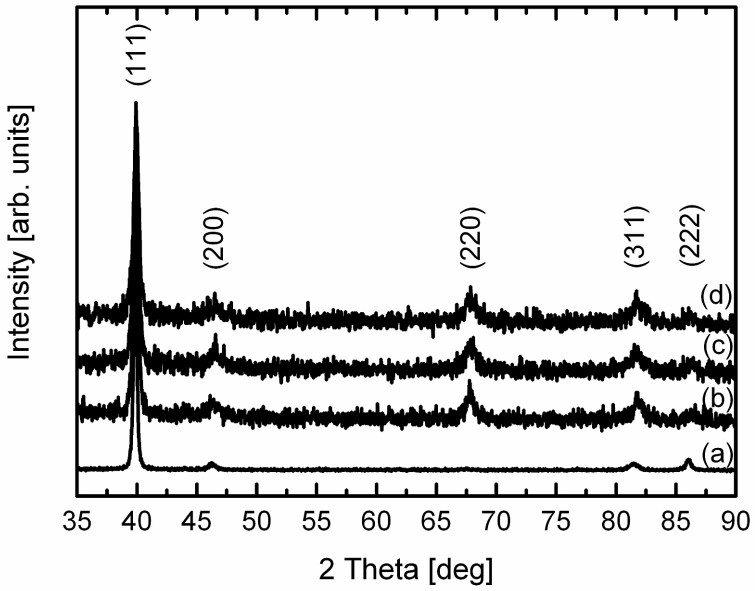

Figure 4.7: Evolution of the structure of solid solution PdAu films with 10 at.% Au and 500 nm thickness determined by X-ray diffraction as a function of the pressure of the Ar-sputtering gas: (a) 0.005 mbar, (b) 0.010 mbar, (c) 0.015 mbar, and (d) 0.020 mbar.

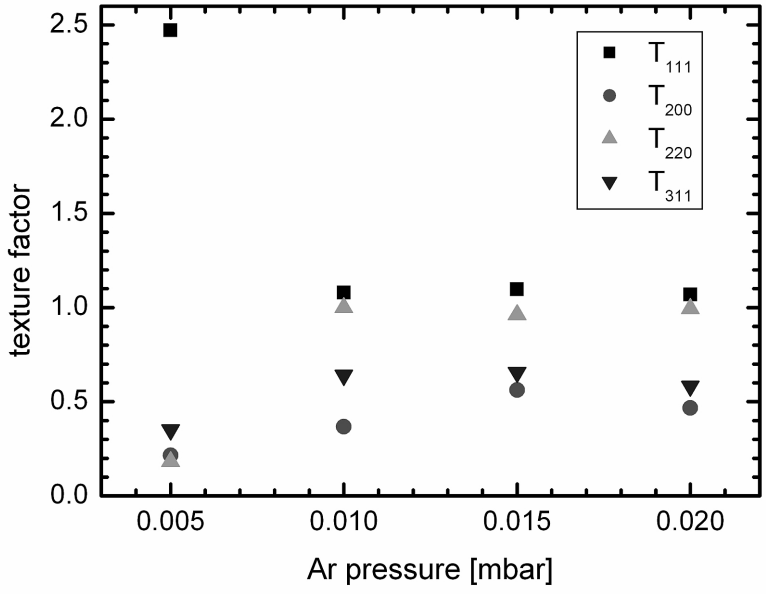

Figure 4.8: Texture factor of the solid solution PdAu films with 10 at.% Au and 500 nm thickness determined by X-ray diffraction as a function of the pressure of the Ar-sputtering gas.

0.01 mbar and above. The lattice parameter does not depend on the pressure of the sputtering gas. Again, as in the case of pure Pd, the value of 0.39175 nm is slightly larger than the expected value of 0.39085 nm for the solid solution PdAu with 10 at.% Au reported in the literature [63].

Figures 4.9 to 4.11 display bright-field cross-sectional TEM micrographs and the corresponding electron diffraction patterns of the Pd films. Films deposited at a low pressure of the sputtering gas (0.005 mbar) exhibit a dense nanocrystalline grain structure. In particular, there is no indication of a strong columnar growth often observed in sputtered films (Figure 4.9). The average grain size of 30 ± 15 nm (standard deviation) determined from DF-TEM images corresponds well to the grain size of 33 nm calculated from XRD. The surface of the Pd film (lower right corner) appears to be smooth, in particular compared to samples prepared at higher pressures (see below). In contrast, the film sputtered at a slightly higher pressure of 0.006 mbar exhibits a strong columnar microstructure (Figure 4.10). The average column width is 66 nm, but each column consists of multiple grains with a broad size distribution centered at an average of 21 ± 10 nm. Each column has a faceted top, which results in a rough film surface (lower left corner). By further increasing the Ar pressure to 0.015 mbar, the structure remains columnar but a large number of twins parallel to the column walls is observed (Figure 4.11). The column width and the grain size are almost unchanged with 67 nm and 24 ± 15 nm, respectively. The surface of all samples with columnar growth appears to be rough. Further details will be given below.

Cross-sectional TEM of the solid solution PdAu film (Figure 4.12) shows again a non-columnar nanocrystalline structure with a smooth surface (lower left corner) at the lowest pressure of the Ar-sputtering gas (0.005 mbar). The average grain size calculated from DF-TEM images is 29 ± 12 nm, which is slightly lower than the value observed from XRD measurements.

Conventional density measurements could not be performed on the sputtered films, because the films were too thin and could not be removed from the substrate without damage. But the TEM measurements of the Pd films prepared at the lowest pressure of the Ar-sputtering gas (0.005 mbar) reveal no signs of pores or other vacancies, like in inert-gas condensated nc Pd. Therefore, we call the sputtered nc structure dense, in agreement with the literature [18].

Additionally, the surface roughness of the Pd films was measured by STM, figure 4.13 displays the surface of a Pd film sputtered at 0.005 mbar Ar pressure. The average roughness is approx. 7 nm for the sample sputtered at 0.005 mbar Ar pressure and 18 nm for the one sputtered at 0.015 mbar. These results confirm the TEM observations.

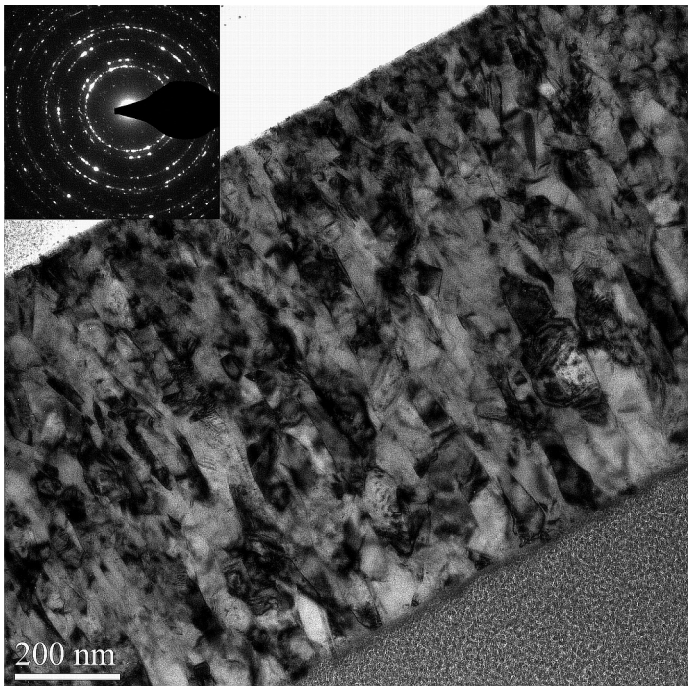

Figure 4.9: Cross-sectional transmission electron microscopy image of a Pd film sputtered at 0.005 mbar Ar-sputtering gas pressure.

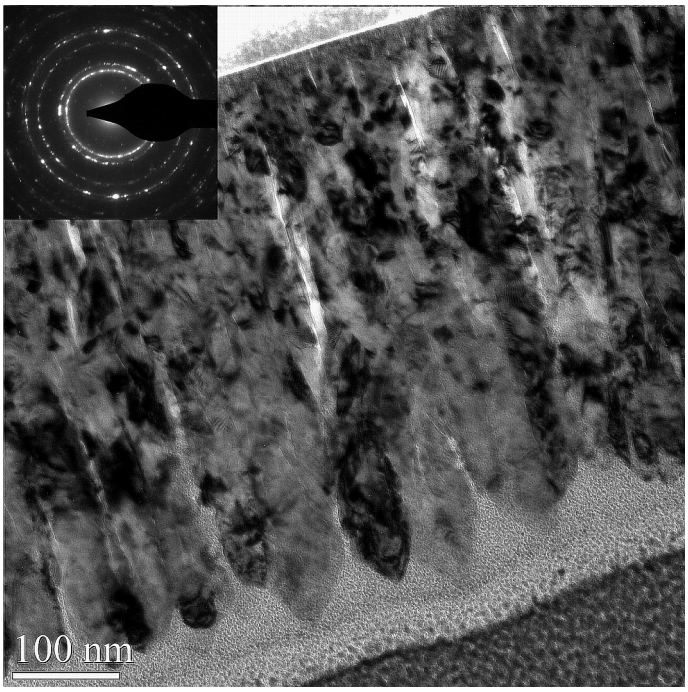

Figure 4.10: Cross-sectional transmission electron microscopy image of a Pd film sputtered at 0.006 mbar Ar-sputtering gas pressure.

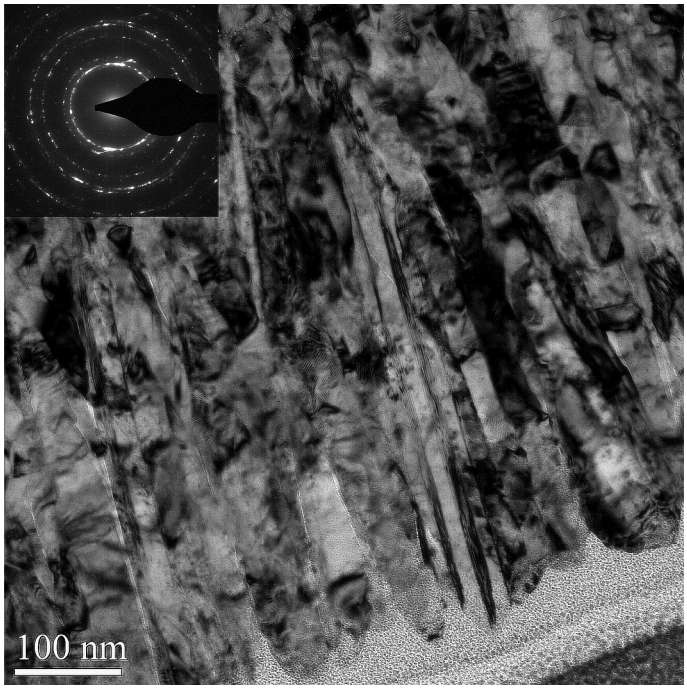

Figure 4.11: Cross-sectional transmission electron microscopy image of a Pd film sputtered at 0.015 mbar Ar-sputtering gas pressure.

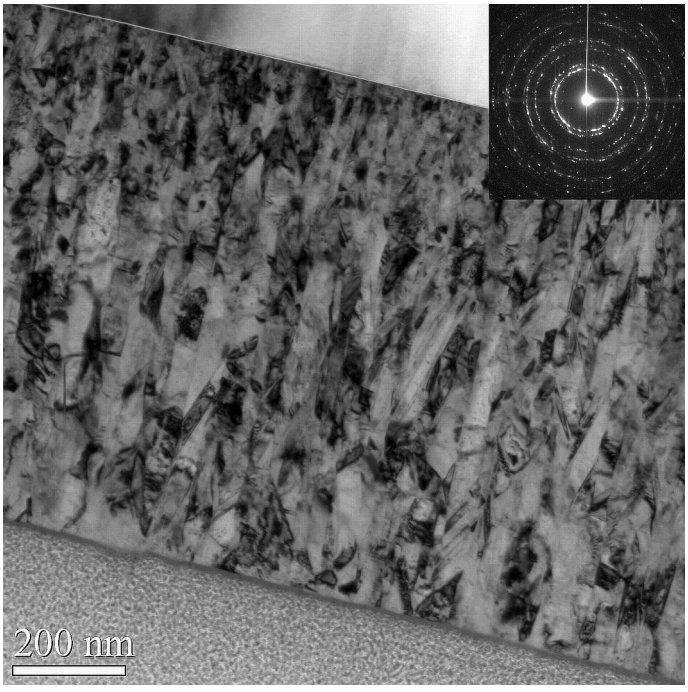

Figure 4.12: Cross-sectional transmission electron microscopy image of the sputtered PdAu film with 10 at.% Au sputtered at 0.005 mbar Ar-sputtering pressure.

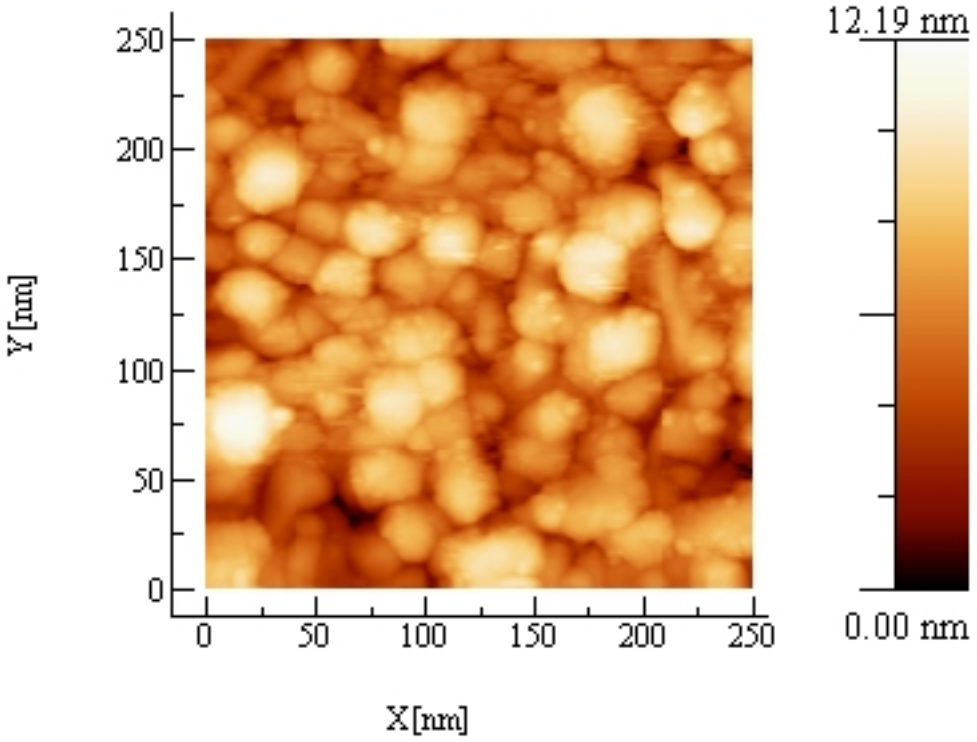

Figure 4.13: Scanning tunneling microscopy image of the surface of the sputtered Pd film sputtered at 0.005 mbar Ar pressure.

Impurity atoms can have substantial influence on the microstructural development and properties of thin films. To analyze the impact of impurity atoms, such as argon or oxygen, in-situ X-ray photoelectron spectroscopy measurements were performed for pure Pd samples deposited at 0.005 mbar and 0.015 mbar, immediately after finishing the sputtering process without breaking the vacuum. In both cases, no evidence of either Ar or O was found within the detection limits of 0.1 at.% of the XPS technique.

4.5 Processing-Structure-Stress Relationship Model

The fundamental process of sputtering has been studied in detail over the past 50 years. A comprehensive and technologically important summary was presented by Thornton and Hoffman (TH) [61]. They investigated a wide variety of metal films

prepared by cylindrical post and planar magnetron sputtering using different sputtering gases, sputtering gas pressures, deposition rates and deposition geometries. Both tensile and compressive intrinsic stresses were reported for magnetron sputtered films. A fundamental finding of TH was the identification of a stress reversal from compressive to tensile stress with operational parameters as a material property. This stress reversal was reported in several other publications experimentally as well as by simulations [64]. The critical pressure for the compression-to-tensile stress transition depends on the atomic mass of the deposited material. It is found that it increases with increasing atomic mass. Pd was not investigated in the work by TH. However, the critical pressure of 0.005 mbar for the compression-tensile transition observed in the present study is close to the literature results for other metals. A value of approx. 0.004 mbar was predicted for rectangular planar magnetrons and 0.008 mbar for cylindrical-post magnetrons [61]. Since the present geometry is based on slightly tilted planar magnetrons, a minimal increase compared to the predicted pressure for rectangular planar magnetrons is expected. The further increase of the critical pressure (0.005 mbar $< p_{\mathrm{crit}} <$ 0.006 mbar) for the PdAu solid solution films is due to the enlarged average atomic mass compared to pure Pd, see figure 4.14.

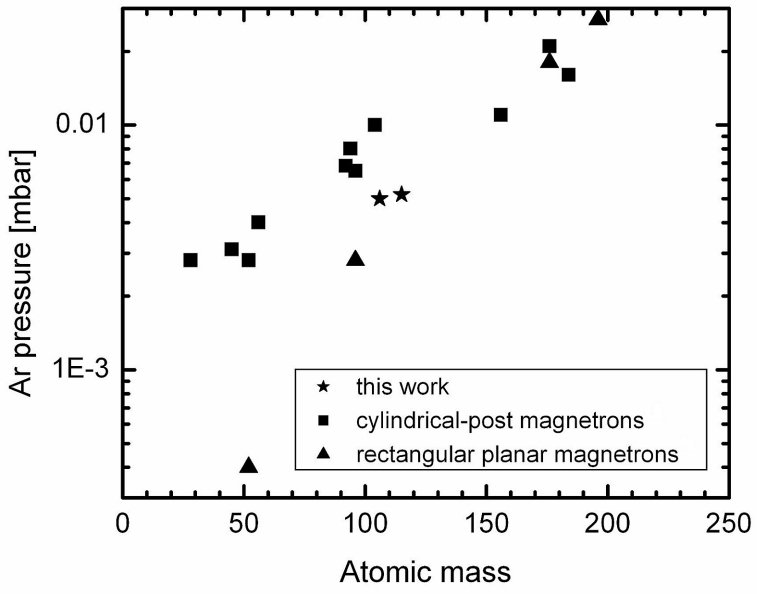

Figure 4.14: Argon transition pressure vs. atomic mass of sputter-coating materials for tensile-to-compressive stress reversal in Pd and $Pd_{90}Au_{10}$ films evaluated in this work (stars) compared to results from Hoffman [61] for dc rectangular planar magnetrons (triangles) and cylindrical-postmagnetron sources (rectangles).

The evolution of the compressive stress is attributed to an atomic peening process [64]. At low pressures the sputtered metal atoms as well as Ar atoms that are reflected by the target are bombarding the part of the film already deposited with high energy ions and atoms. These ions and atoms reach the surface of the growing film due to the low probability of collision processes between metal atoms and gas atoms at the relatively low pressures. Consequently, the impinging atoms drive surface atoms into the coating, compact the film and cause compressive stress [59], compare fig. 4.15. Several authors also observed trapped gas atoms (Ar and O) in the compressive film [65, 66] and attributed the compressive stress to the incorporation of defects. The influence of incorporated Ar-atoms can be excluded as the results of the in-situ XPS measurements indicate a negligible concentration of Ar in the film surface. In conventional magnetron sputtering very large grains are observed at the lowest sputtering pressures, in case of Pd sputtered by the special multilayer technique, small grain sizes of 30 nm are maintained even at large thickness of the film.

By increasing the sputtering pressure, the atomic peening effect is reduced due to efficient thermalization of the bombarding species. The columnar microstructure and the rough surface generate tensile stresses due to the propensity for in-plane contact between neighboring grain surfaces. The coalescence of neighboring grains can result in the elimination of a grain boundary region, thus reducing the volume by an amount equivalent to the thickness of the grain boundary. The change of the interatomic spacing in this process causes tensile stress [59]. If these findings are compared with the Pd films prepared at a pressure of the Ar-sputtering gas of 0.006 mbar, which showed the highest tensile stress, a highly columnar microstructure and a very pronounced surface roughness combined with a slightly decreased grain size are observed.

A further increase of the sputtering pressure results in a decrease of the tensile stress.

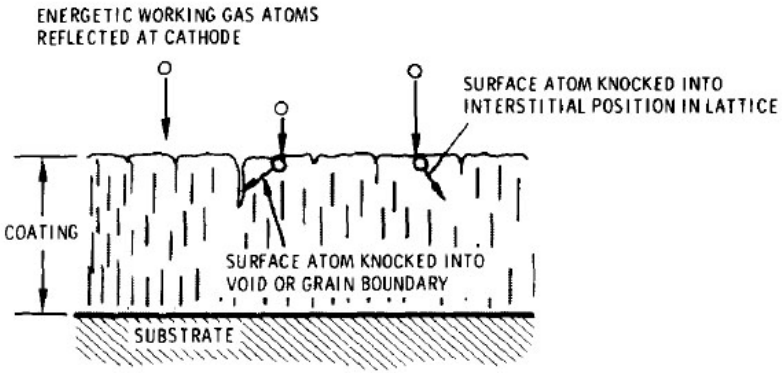

Figure 4.15: Atomic peening model for production of compressive stresses in sputtered coatings deposited at low working pressures [59].

It has been reported that in this regime, the microstructure becomes less dense with dendritic structures and eventually amorphous [59, 65]. In the Pd and PdAu films investigated in the present study, a decrease of tensile stresses was observed, but no amorphization at the highest sputtering pressures occurred.

However, the films prepared at highest pressure of 0.02 mbar showed a reduced reflectivity due to their increased surface roughness, which was also observed by TH [61]. The change in texture from (111) orientation, which is closed-packed in fcc structures with lowest surface energy, to (220) orientation, which is lacking high symmetry, confirms the change to a microstructure with less density.

4.6 Conclusions

The present set of experiments has improved the understanding of residual stress development in magnetron sputtered metal films on flexible substrates. In general, no significant changes were observed in comparison to solid substrates. In the specific case of Pd and the solid solution PdAu a sharp transition from compressive to highly tensile stresses is observed, followed by a gradual decrease in the tensile stress regime with increasing pressure. The observed critical pressures for the compressive-tensile stress transition match with the values predicted by Thornton and Hoffman. The microstructural investigation confirms the results shown for other materials such as W, Be and AlN: columnar structures at highest tensile stress and the beginning of a density reduction of the film with decreasing tensile stress or increasing pressure of the sputtering gas. A novelty was observed at the lowest pressures for Pd as well as for PdAu: the grain structure was still nanocrystalline with grain sizes of about 30 nm, while in case of W and Be the structures show a remarkably increased grain size at low sputtering pressure. This effect demonstrates the strength of the multilayer sputtering technique in combination with low processing temperatures to maintain the small grain sizes even in thick films.

5 Deformation Processes in Nanocrystalline Palladium

The microstructure and mechanical properties of nanocrystalline Pd films prepared by magnetron sputtering have been investigated as a function of strain. The films were deposited onto supporting polyimide substrates and tested in tensile mode. High ultimate tensile strength of 1200 MPa and ductility up to 10 % (engineering strain) were achieved. They are the result of the deformation mechanisms active in the nanocrystalline material. In the current chapter grain growth and twinning were identified as important mechanisms contributing to the deformation in pure nanocrystalline Pd by post-mortem TEM analysis. Additionally pure Pd with a bimodal grain size distribution was investigated, it shows enhanced deformability but reduced tensile strength. Pure Pd as a single element material was chosen as a basis material before alloying effects were investigated in the following chapter 6.

5.1 Introduction

Nanostructured metals and alloys often exhibit unusual mechanical behavior compared to their coarse-grained counterparts [67]. They show extraordinary strength but often exhibit a lack of ductility or suffer from rapid strain localization [68]. That is why understanding the underlying deformation mechanisms operating in these structures is very important to guarantee their reliability in next-generation micro- and nanoscale devices. In nanocrystalline metals, with grain sizes of less than 100 nm, the conventional deformation mechanisms of dislocation generation and multiplication observed in coarse-grained metals are hindered by the grain boundaries. It is believed that their low ductility is associated to this effect [19].

Metals with bimodal grain structure combine both high strength and ductility [69, 70]. This material typically consists of a nanocrystalline (nc) or ultrafinegrained (ufg) matrix in which coarse grains are incorporated. Compared to the pure nc metals bimodal metals show remarkably improved ductility and only slightly reduced

strength [70]. This effect is believed to be resulting from a combination of conventional dislocation slip in the coarse grains and grain boundary mediated processes in the nc or ufg grains.

To study the mechanical properties of nanocrystalline metals and the associated deformation mechanisms in more detail, it is important to produce proper testing material. Bulk nanocrystalline materials which can be produced e.g. by severe plastic deformation or inert gas condensation are easy to test, but often suffer from reduced density resulting from incorporated pores. Also the widely used electrochemically deposited metal films contain impurities present in the chemical bath [16]. Both pores and impurities can pin grain boundaries and therefore influence the mechanical behavior. Alternatively, interrupted magnetron sputtering is a technique capable of producing dense nanocrystalline metals with low impurity levels [17–19]. The drawback of this technique is the difficulty in testing the mechanical properties of the thin films, because of difficulties in handling them. Therefore, a supporting flexible substrate was used to stabilize the samples and to avoid strain localization during tensile testing [23, 71].

The goal of the present chapter is to investigate the deformation processes active in nanocrystalline and bimodal structured Pd films deposited by magnetron sputtering onto compliant substrates, which exhibit a high mechanical strength. Microstructural analysis was performed by transmission electron microscopy (TEM) after straining to different deformation levels.

5.2 Experimental

Nanocrystalline palladium specimens were deposited by radio frequency (RF) magnetron sputtering using 2" diameter planar targets with 99.95 % purity. Several pure Pd samples were prepared with constant sputtering power of 60 W at a working gas pressure (Ar) of 0.005 mbar. At room temperature 1 μm thick Pd films were grown in 100 steps of 10 nm thickness each interrupted for 10 s using a fast rotational shutter in front of the Pd target.

Polyimide Kapton E (Dupont) with a thickness of 50 μm was used as a substrate. Prior to the film deposition, the substrate was cut into strips of 30 mm length and 5 mm width using a razor blade. Afterwards the samples were cleaned in an ultrasonic bath filled with acetone for 15 min, and then rinsed with isopropanol on a resist spinner. Directly after rinsing, the samples were clamped onto special sample holders and transferred into ultrahigh vacuum of $2.0 \cdot 10^{-8}$ mbar in the sputtering chamber via a load lock system, which was baked out for 5 min at 200 °C and pumped over night.

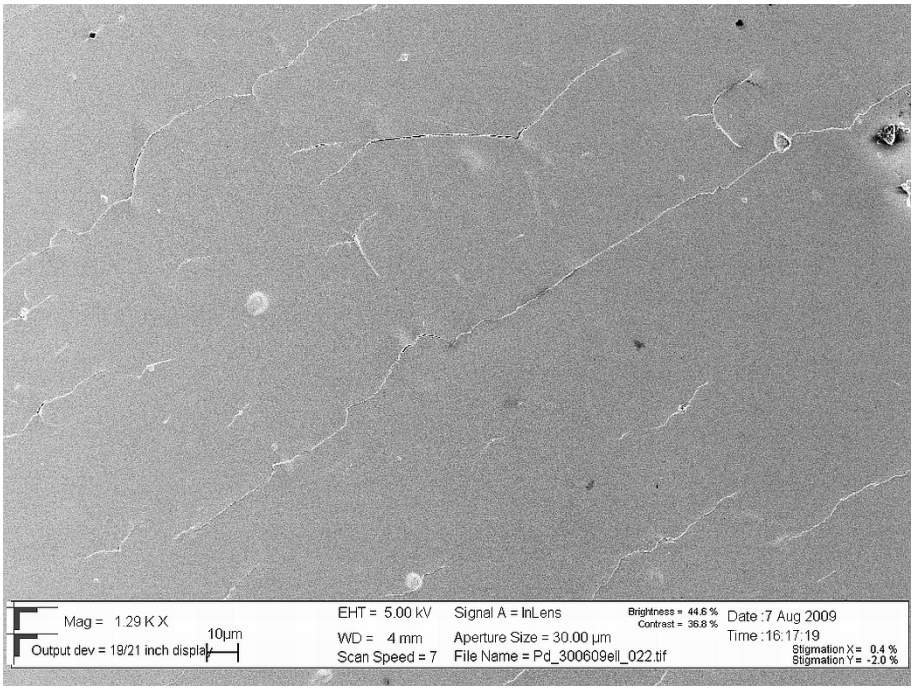

Figure 5.1: Tensiled nc Pd film on improper substrate material Kapton HPP-ST, after 10 % strain.

The sample shape was changed compared to the shape used in chapter 4. The stamping technique used to fabricate the dogbone shape was disadvantageous for mechanical tests, because the sample edges showed fissures. After film deposition the films were inhomogeneous at the fissures which resulted in strain localization and cracking. Therefore, a razor blade was used to cut the Kapton substrate resulting in smooth edges. Unfortunately, it was not possible to cut reproducibly shaped dogbone samples with the razor blade and so strip-shaped samples were prepared for tensile testing.

The choice of an appropriate substrate and cleaning procedure is crucial to the film adhesion on the substrate [71]. Figure 5.1 shows a Pd film sputtered with identical conditions onto a different type of polyimide, named Kapton HPP-ST (DuPont) after it was tensiled to 10 % strain. A close network of cracks and other surface defects are observed, with a crack density in the direction of strain of 55 ± 32 cracks per mm. It was discovered that this substrate, although it is almost chemical identical to the chosen Kapton E (crack density < 10 cracks per mm), tends to delamination resulting from particles added on the substrates' surface by the manufacturer. These particles help to improve the uncoiling behaviour of the polyimide but they serve as origin of delaminations in the sputtered film.

Palladium specimens with bimodal grain structure were prepared by annealing nc Pd samples in-situ without breaking UHV conditions. After sputtering was com-

pleted the samples were moved into an annealing chamber with a base pressure of $5.0 \cdot 10^{-8}$ mbar. Heating bulbs were used to anneal the samples. By this technique the sample's temperature was increased almost linear up to a certain value, when the heating bulbs were switched off. The samples were cooled down under vacuum conditions for at least 60 minutes and removed from the vacuum system. Two sets of samples were prepared with different grain sizes. Sample Pd_{200} was heated for 200 s with a maximum temperature of approx. 165 °C. Sample Pd_{300} was heated for 300 s with a maximum temperature of approx. 230 °C.

Uniaxial tensile tests were carried out at room temperature using a dedicated tensile stage for miniature specimens, as was described in chapter 3.4.1 at a strain rate of $5 \cdot 10^{-5}$ s^{-1} and $2.5 \cdot 10^{-5}$ s^{-1}. The tensile tester was equipped with a special thin film sample clamping to avoid sample deformation during mounting of the delicate thin films. The elongation was precisely measured using a laser extensometer P-50 by Fiedler Optoelectronics to read paper marks added on the backside of the polyimide samples. Samples were pulled to a maximum elongation of 10.0 %. For TEM analysis three additional nc Pd samples were stretched with $5 \cdot 10^{-5}$ s^{-1} to only 2.0 %, 3.5 % and 5.0 % strain and relaxed.

Transmission electron microscopy analysis was performed using a FEI Titan $80-300$ with Cs-corrected imaging system operated at 300 kV. Statistical grain sizes were evaluated by measuring at least 200 grains in different orientations for each straining level including a compilation of grain size distributions, which were mainly lognormal distributed.

Specimens for TEM were taken from the central part of the tensile sample. The Kapton backside was mechanically dimpled and then the metallic film was cut out and clamped in a Cu folding grid to avoid bending of the deformed films. Further thinning of plane-view samples to a thickness of electron transparency was performed using a Gatan Precision Ion Polishing System (PIPS) with Ar^+ ions accelerated by 2.5 kV. Scanning electron microscopy (SEM) was conducted using a Zeiss Leo 1530 Gemini operated at 5 kV and a working distance of 3 mm.

Conventional Θ-2Θ XRD measurements (Bragg-Brentano) were performed using the Bruker D 8 Discover diffractometer to investigate the crystallographic texture and grain sizes, which were determined by Rietveld analysis using Bruker Topas 3.0 software.

Film thickness was controlled on a random basis using a Dektak 6m stylus profilometer by Veeco Instruments. The results agreed well to the ones observed from cross-sectional TEM and the predicted thickness calculated from the sputtering rate.

5.3 Microstructural Characterization of Undeformed Pd Films

In the last chapter it was shown, that using the described parameters we are able to produce dense Pd films with an almost equiaxed nanocrystalline structure, low residual stress (only 16 ± 25 MPa for 1 μm thick films) and low impurity level.

Figure 5.2 displays a dark-field TEM image of the as-deposited microstructure of the sputtered nc Pd films in plane view, which corresponds to the tensile direction. A uniform grain size distribution with a mean grain size of 48 ± 15 nm is observed by DF-TEM, the grains are fully equiaxed. The number of grains containing visible twins in the TEM lamella tilted to 5 different diffraction angles compared to the total number of grains (later on called density of twinned grains) was very low with only 0.48 %.

Figure 5.3 displays a dark-field TEM image of the as-prepared microstructure of the annealed sputtered Pd_{200} films in plane view, which corresponds to the tensile direction. A bimodal grain size distribution with a numeric majority at small grain sizes below 100 nm is observed with a medium grain size of 65 nm ± 13 nm, indeed the area is dominated by larger grains with 500 nm to 800 nm diameter, medium

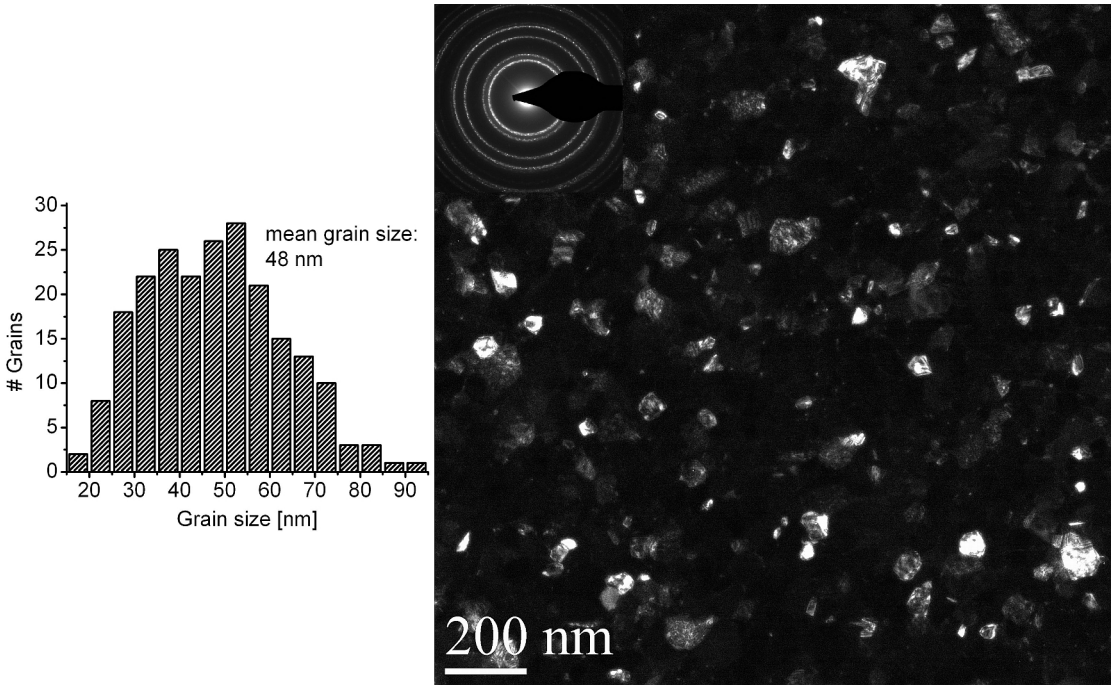

Figure 5.2: In-plane dark field transmission electron microscopy image of the undeformed sputtered nc Pd film.

grain size: 299 nm ± 152 nm. The grains are fully equiaxed and big and large grains are almost randomly distributed in the film. The number of grains containing visible twins is negligible.

The samples annealed at higher temperature Pd_{300} show also a bimodal grain size distribution in TEM imaging, but with increased grain sizes: The small grains dominate again the numerical grain size distribution, but here with grain sizes below 200 nm, medium grain size: 139 nm ± 79 nm. The area is dominated by larger grains with a medium grain size of 646 nm ± 167 nm. The grains are fully equiaxed and big and large grains are almost randomly distributed in the film. The number of grains containing visible twins is negligible.

XRD analysis of the nc Pd films reveals a slightly preferred orientation in (111) direction (figure 5.4). The grain size determined by Rietveld analysis to be 47 ± 13 nm is in good agreement to the one observed by TEM analysis. A medium microstrain was observed in the as-deposited nc Pd samples with 0.05 ± 0.03.

The bimodal grain size distribution of the annealed Pd films Pd_{200} and Pd_{300} could not be distinguished by XRD analysis due to the small difference in the minimum and maximum grain size. The microstrain in both cases is negligible with 0.00002. This points to an relaxation of internal stresses during the annealing process.

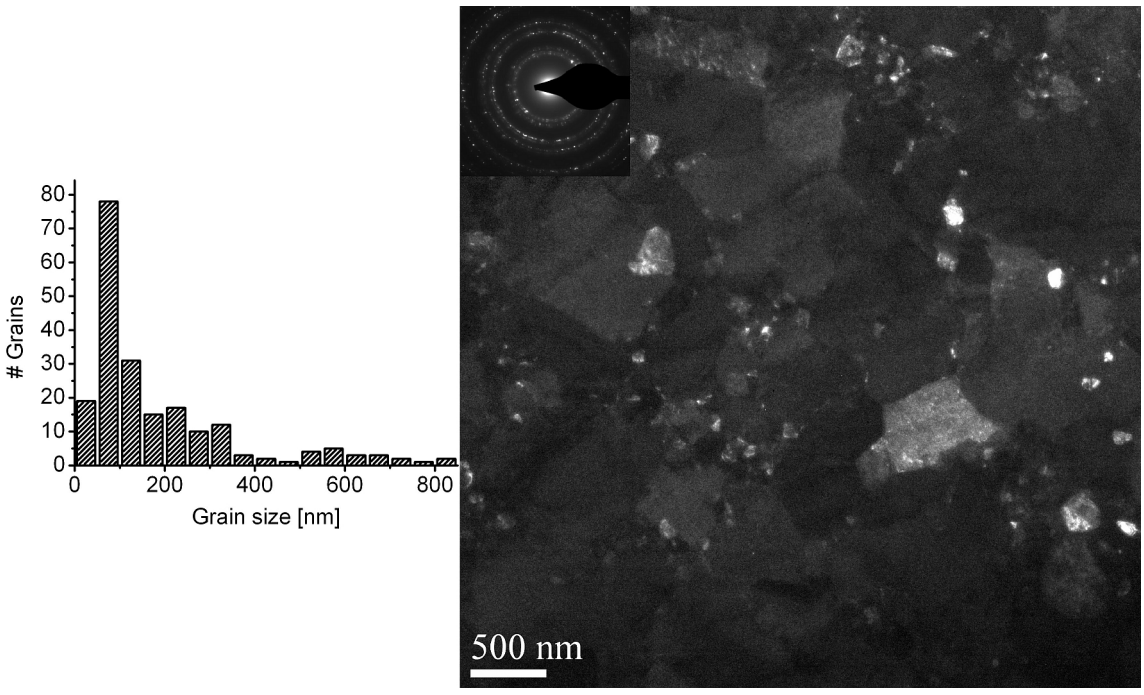

Figure 5.3: In-plane dark field transmission electron microscopy image of the undeformed sputtered bimodal Pd film annealed for 200 s at a maximum temperature of approx. 165 °C.

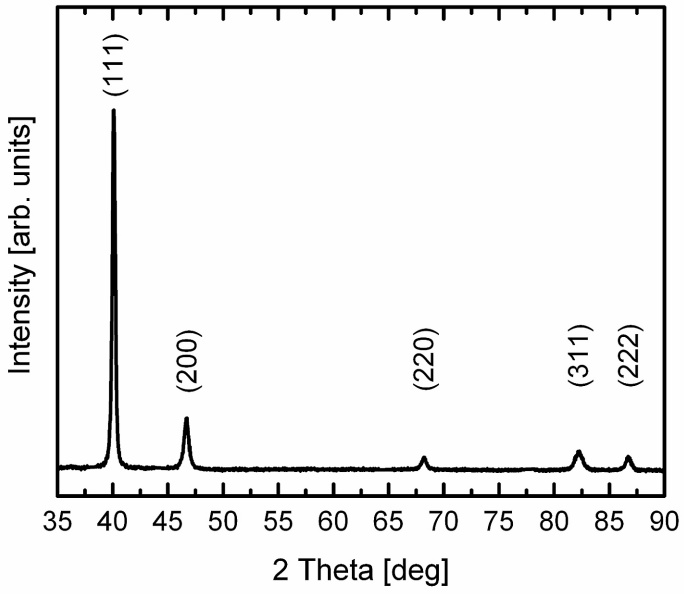

Figure 5.4: X-ray diffraction pattern of the undeformed sputtered nc Pd film.

5.4 Mechanical Properties

To investigate the tensile properties of the actual Pd films on polyimide substrates an additional step is necessary: Yu and Spaepen [23] have shown that the strain applied to the deposited metallic film and the Kapton substrate is the same and the measured force is simply the sum of the forces on both layers:

$$F_{\text{total}} = F_{\text{film}} + F_{\text{Kapton}} \tag{5.1}$$

Therefore, the force-strain curves of several Kapton foil samples with identical dimensions to the sputtered samples were averaged and subtracted from the force-strain curves obtained during tensile testing of the Pd films on the Kapton substrate, compare fig. 5.5.

The accuracy of the resulting data is somewhat limited as can be seen in figure 5.6, where three tensile tests with identical test parameters are shown. The strong signal of the substrate material results in measurement errors in the calculated stress-strain curves of about 100 MPa, meaning a relative error in the stress values of almost 10 %. Therefore, the estimation of the elastic modulus was not feasible and resulted in implausible values, that are not shown in this work.

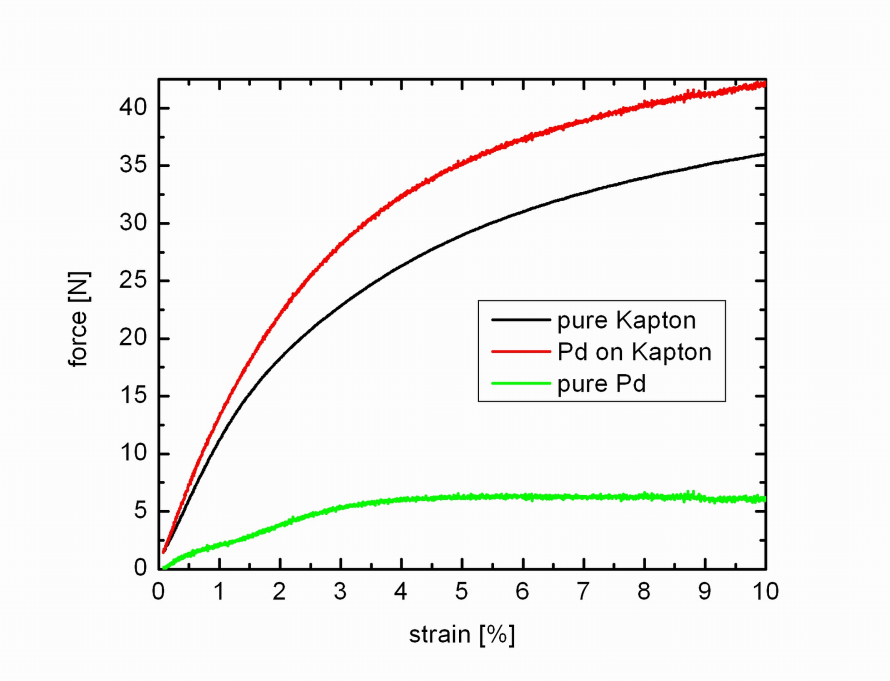

Figure 5.5: Force-strain curves of pure Kapton substrate and a 1 μm thick nc Pd film on Kapton substrate tested at $5 \cdot 10^{-5}$ s^{-1} strain rate and the resulting curve of the pure Pd film.

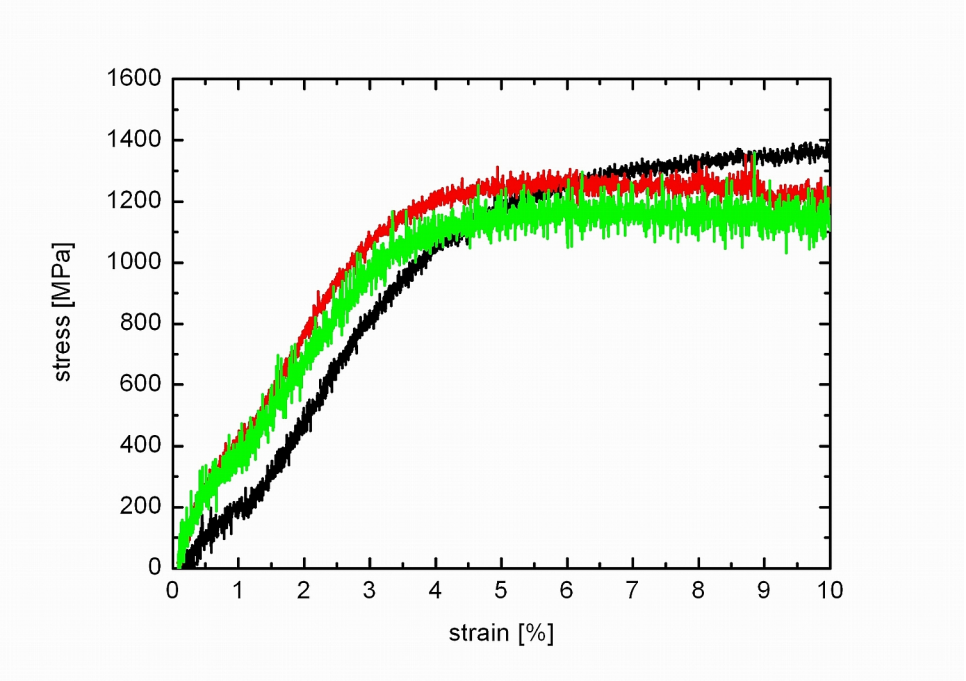

Figure 5.6: Stress-strain curves of three 1 μm thick nc Pd films tested at $5 \cdot 10^{-5}$ s^{-1} strain rate after subtraction of the substrate signal.

Figure 5.7 shows three typical resulting tensile curves of the 1 μm thick nc Pd film Pd_{nc} and the bimodal Pd films Pd_{200} and Pd_{300} deformed at a strain rate of $5 \cdot 10^{-5}$ s^{-1}. With 1260 $\pm$ 100 MPa, the ultimate tensile strength of the nanocrystalline Pd is increased by a factor of 4.5 compared to its coarse-grained counterpart with 270 MPa [72]. The stress increases linearly up to 2.5 % engineering strain, shows some strain hardening up to 5.0 % strain and then saturates at 1260 MPa until the test was stopped at 10.0 % strain.

The bimodal sample Pd_{200} with a medium grain size of 187 $\pm$ 183 nm shows a reduced ultimate tensile strength of 990 $\pm$ 100 MPa, whereas the UTS is further reduced to 870 $\pm$ 100 MPa in sample Pd_{300} with a medium grain size of 231 $\pm$ 235 nm. The bimodal samples show an increased strain hardening compared to the nc films. No saturation in the stress was observed in both cases. The tests were stopped at 9 % strain even though no cracking could be observed in post-mortem SEM top-view investigations.

Figure 5.8 displays a Hall-Petch plot with the ultimate tensile strength values of the nc Pd and the bimodal Pd samples (small grains) tested at a strain rate of $5 \cdot 10^{-5}$ s^{-1} as well as the ultimate tensile strength of the coarse grained Pd, which was reported in the literature [72]. The data points match the expected linear behavior according to the Hall-Petch equation (2.2). By linear fitting of the data one obtains the Hall-Petch constants $k_y = 6.47$ MPa $mm^{1/2}$ and $\sigma_0 = 278$ MPa.

The data points of the bimodal Pd samples show reduced strength compared to the value predicted by the Hall-Petch equation. This effect results from the special grain size distribution present in bimodal microstructures. The medium grain size of the small grains was used for the Hall-Petch plot, because according to the results obtained by Han and coworkers [70] the small grains in the bimodal structures carry the load and cause increased tensile strength compared to samples with grain sizes of medium size in-between the sizes of the small and large grains. Our results confirm their model, because the strength of the bimodal samples is only slightly reduced compared to the values predicted by the Hall-Petch equation for nanocrystalline samples with grain size corresponding to the small grains in the bimodal structures.

To determine the activation volume ΔV and the strain rate sensitivity m tensile tests at two different strain rates were performed, as is shown in fig. 5.9. Preferably strain rate jump tests or relaxation tests would be applied to estimate these values, but this was not possible. Figure 5.10 displays strain rate jump tests with pure Kapton substrate samples. The arrows mark the jumps in the strain rate. One clearly observes that the substrate material itself suffers from relaxation effects. Therefore, the determination of the pure film signal was not possible for strain rate jump tests and relaxation tests.

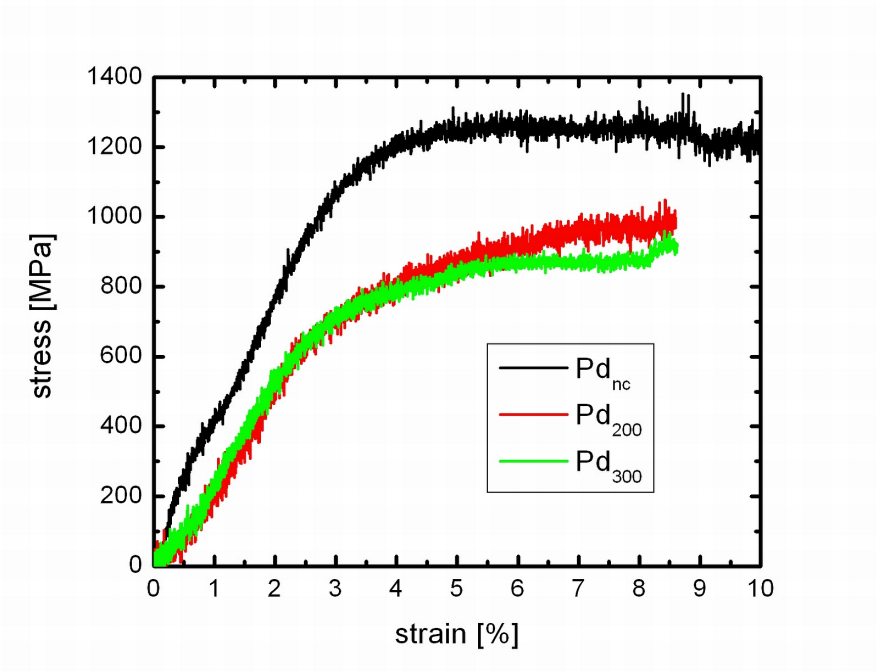

Figure 5.7: Stress-strain curves of 1 μm thick nc Pd film Pd_{nc} and bimodal Pd films Pd_{200} and Pd_{300} tested at 5 $\cdot$ 10^{-5} s^{-1} strain rate after subtraction of the substrate signal.

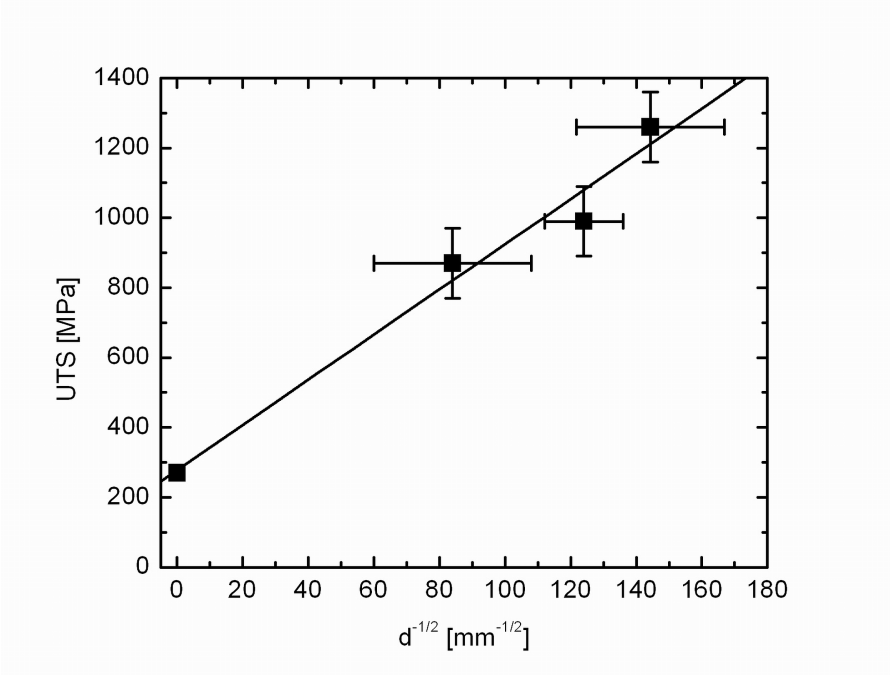

Figure 5.8: Hall-Petch plot of 1 μm thick nc Pd film Pd_{nc} and bimodal Pd films Pd_{200} and Pd_{300} tested at 5 $\cdot$ 10^{-5} s^{-1} strain rate and coarse grained Pd [72].

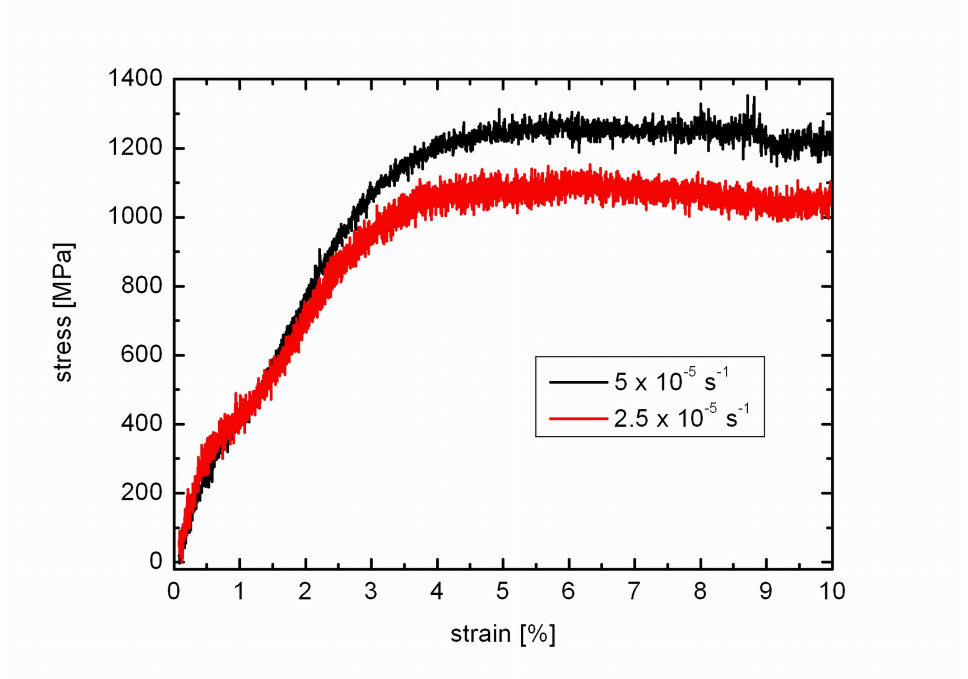

Figure 5.9: Stress-strain curves of pure 1 μm thick nc Pd films tested at $2.5 \cdot 10^{-5}$ s^{-1} and $5 \cdot 10^{-5}$ s^{-1} strain rate.

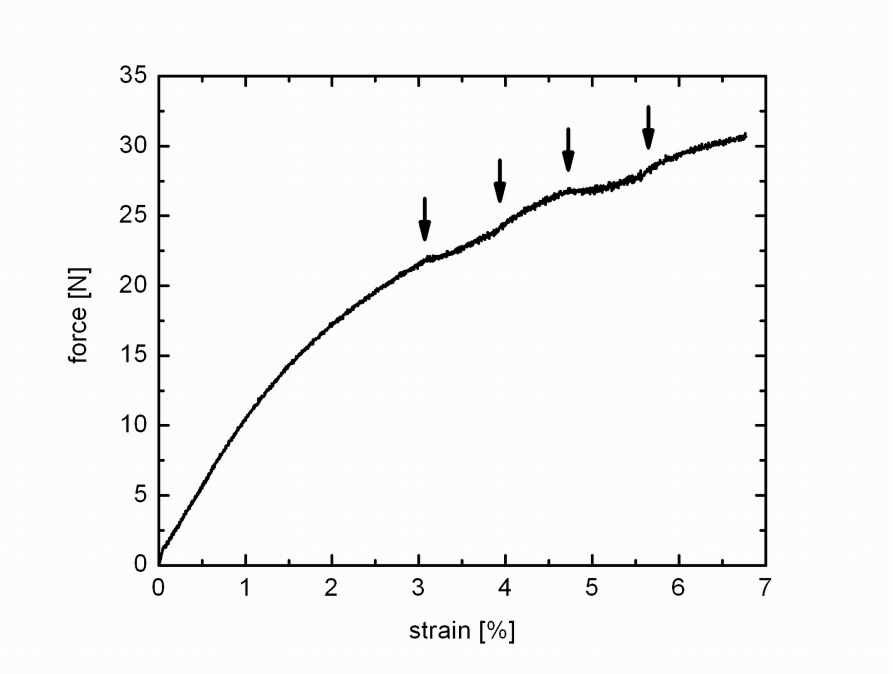

Figure 5.10: Strain rate jump tests on pure Kapton tested at $5 \cdot 10^{-5}$ s^{-1} and $2.5 \cdot 10^{-5}$ s^{-1}.

Table 5.1 displays an overview of the mechanical properties of nc Pd films and bimodal structured Pd films. Note the large error bars given for the strain rate sensitivity m and the activation volume ΔV. They are the results of remarkable uncertainties in the test method. Strain rate sensitivity m and activation volume ΔV were calculated using equations (2.3) and (2.14), respectively. The values of $\dot{\epsilon}_2$, $\dot{\epsilon}_1$, σ_2, and σ_1 were determined from the two tensile tests at different strain rate.

Sample	small grain size [nm]	UTS [MPa]	m	ΔV [b^3]	crack density
Pd_{nc}	47 ± 13	1260 ± 100	0.22 ± 0.14	1.3 ± 0.8	7.5/mm
Pd_{200}	65 ± 13	990 ± 100	0.07 ± 0.07	4.7 ± 4.3	-
Pd_{300}	139 ± 79	870 ± 100	0.07 ± 0.04	5.8 ± 3.6	-

Table 5.1: List of mechanical properties of Pd samples Pd_{nc}, Pd_{200} and Pd_{300}: ultimate tensile strength (UTS) at $5 \cdot 10^{-5}$ s^{-1} strain rate, strain rate sensitivity (m), activation volume (ΔV) and crack density.

5.5 Microstructural Characterization of Deformed Pd Films

The microstructural deformation processes were monitored by TEM. The microstructure of the deformed bimodal Pd film Pd_{200} after 10.0 % elongation is shown in fig. 5.11. Here grain growth is observed in the small grains as well as in the big grains, compare the grain size distribution. The amount of small grains below 100 nm diameter decreased remarkably.

Hence, the medium grain size of small grains in the Pd_{200} sample increased from 65 ± 13 nm to 198 ± 58 nm, whereas the maximum grain size increased only by a factor of two from 299 nm ± 152 nm to 593 nm ± 191 nm. Twin formation was not observed in a statistical relevant amount.

The medium grain size of small grains in the Pd_{300} sample increased from 139 ± 79 nm to 233 ± 78 nm, whereas the maximum grain size was constant with 646 nm ± 167 nm before and 620 ± 134 nm after deformation. Twin formation was not observed in statistical relevant amount in the Pd_{300} samples, either.

SEM top-view imaging of the deformed bimodal Pd films Pd_{200} and Pd_{300} revealed smooth surfaces with no cracking after 10 % elongation.

In fig. 5.12 to 5.15 the in-plane dark-field micrographs of the nc Pd films after several strains are shown: the initially uniform grain size distribution is maintained up to the largest deformation of 10 % engineering strain. The grain size increases, but no preferred growth direction is obtained and the size distribution remains lognormal distributed. Additionally an increasing twin density is observed.

Fig. 5.16 displays a SEM top-view overview image of the deformed film after 10 % elongation and relaxing the film. At this strain cracking starts in the Pd film, preferably at weak points where the film adhesion is disturbed by foreign particles at the interface [71]. In a detailed view, see fig. 5.17, the grain structure is equivalent to the surface structure visible in the SEM image. In the flawless area the structure is quite homogenous, but at the cracks, where stress-concentrations are assumed, the grain size increases extraordinary to hundreds of nanometers. The cracks are mainly oriented in 45 degree to the loading direction.

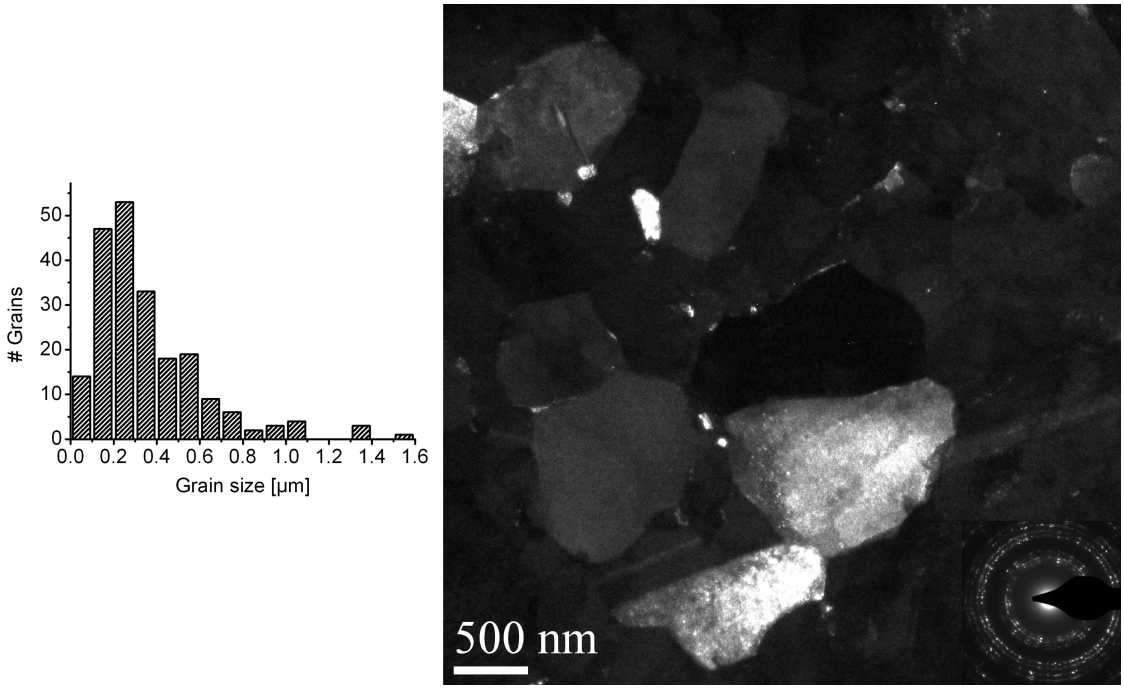

Figure 5.11: In-plane dark field transmission electron microscopy image of the tensiled bimodal Pd film Pd_{200} after 10.0 % elongation.

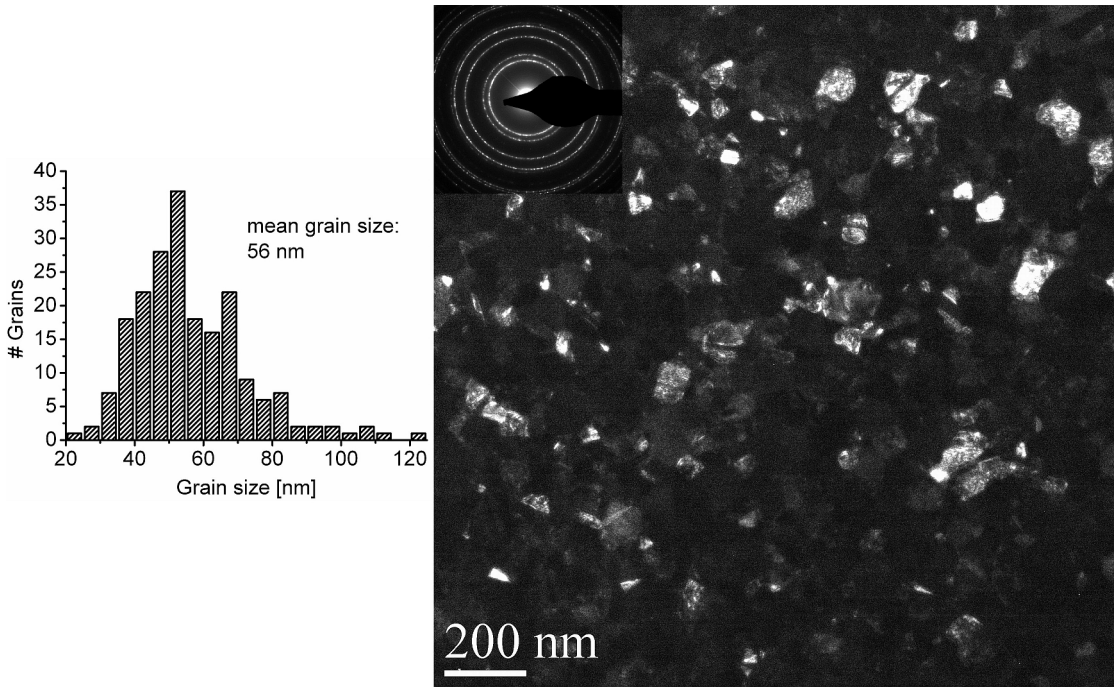

Figure 5.12: In-plane dark field transmission electron microscopy image of the tensiled nc Pd film after 2.0 % elongation.

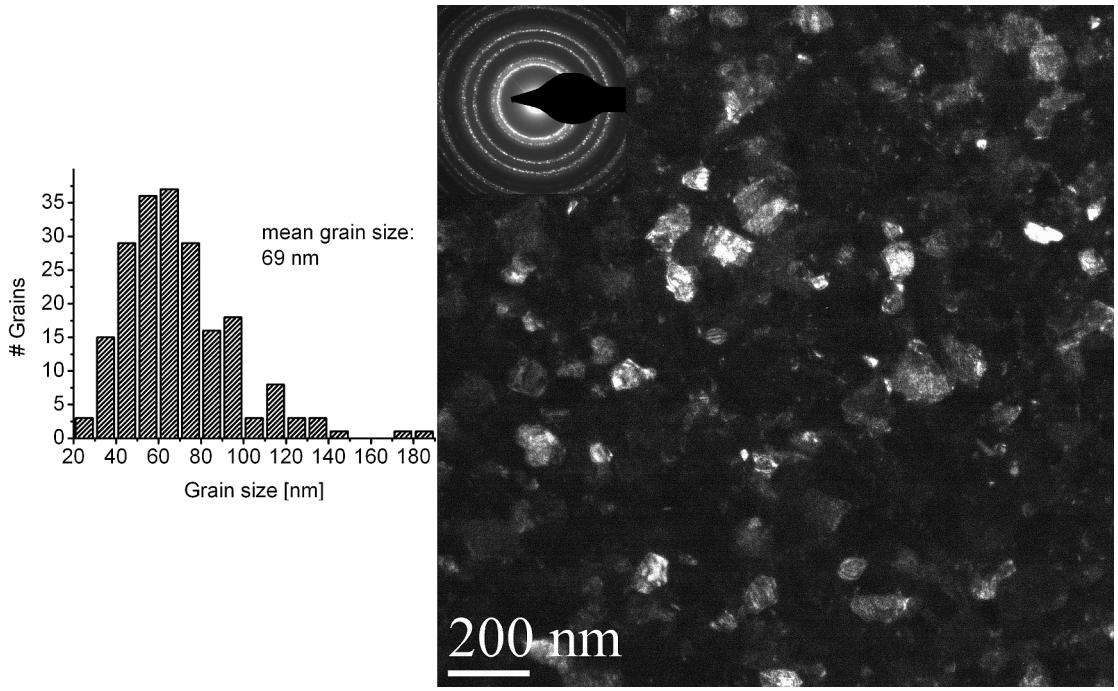

Figure 5.13: In-plane dark field transmission electron microscopy image of the tensiled nc Pd film after 3.5 % elongation.

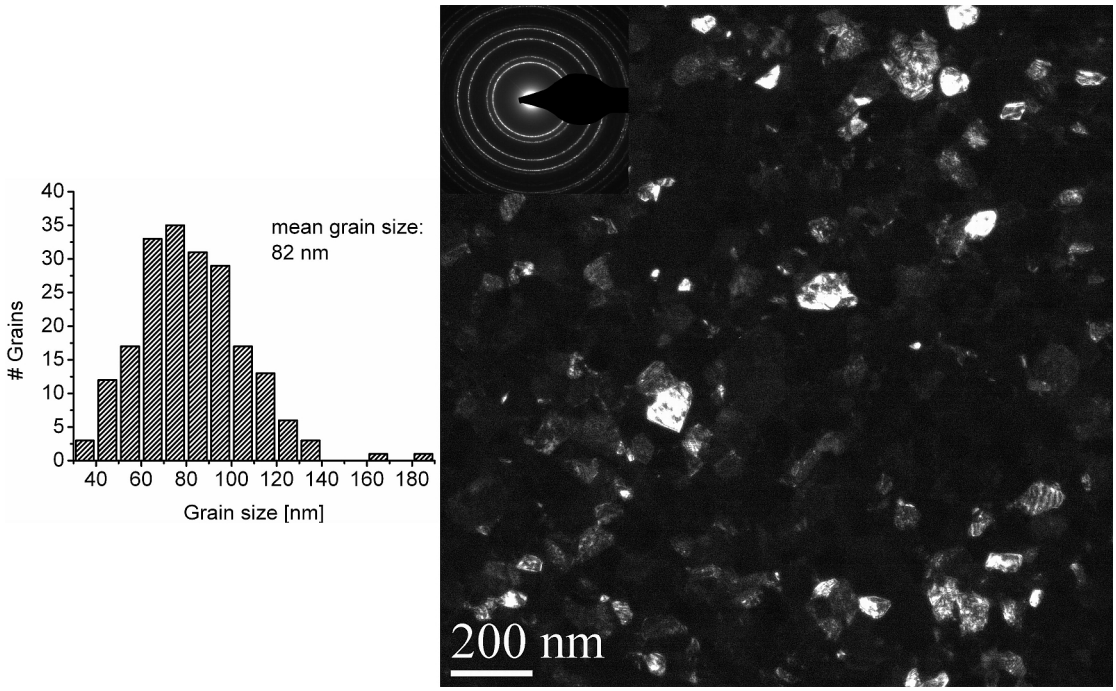

Figure 5.14: In-plane dark field transmission electron microscopy image of the tensiled nc Pd film after 5.0 % elongation.

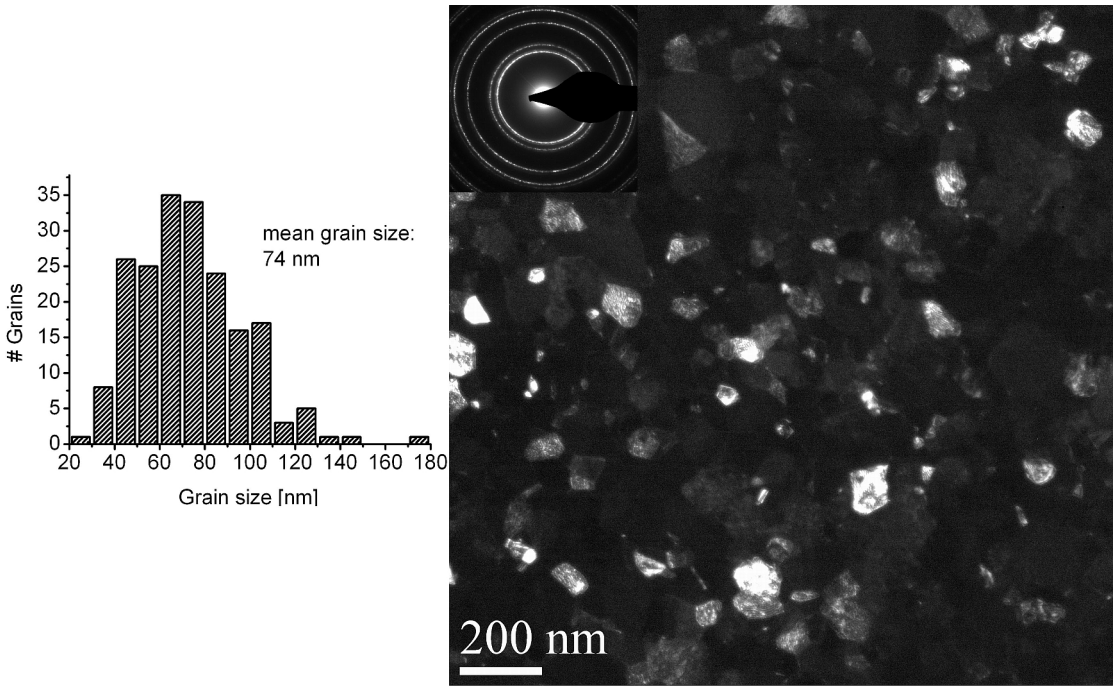

Figure 5.15: In-plane dark field transmission electron microscopy image of the tensiled nc Pd film after 10.0 % elongation.

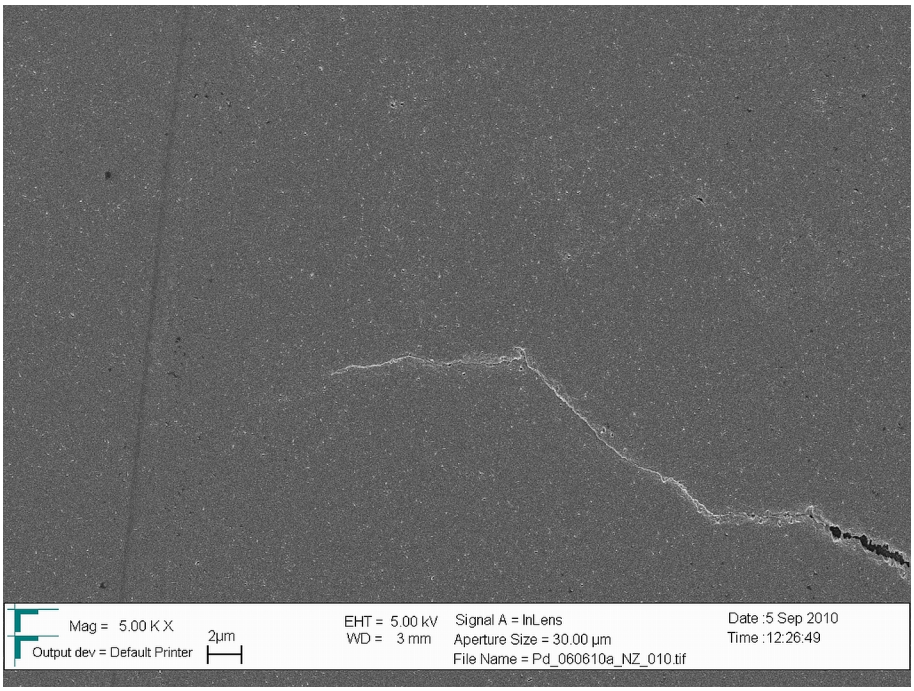

Figure 5.16: Overview SEM image of a crack in the nc Pd film after 10 % elongation.

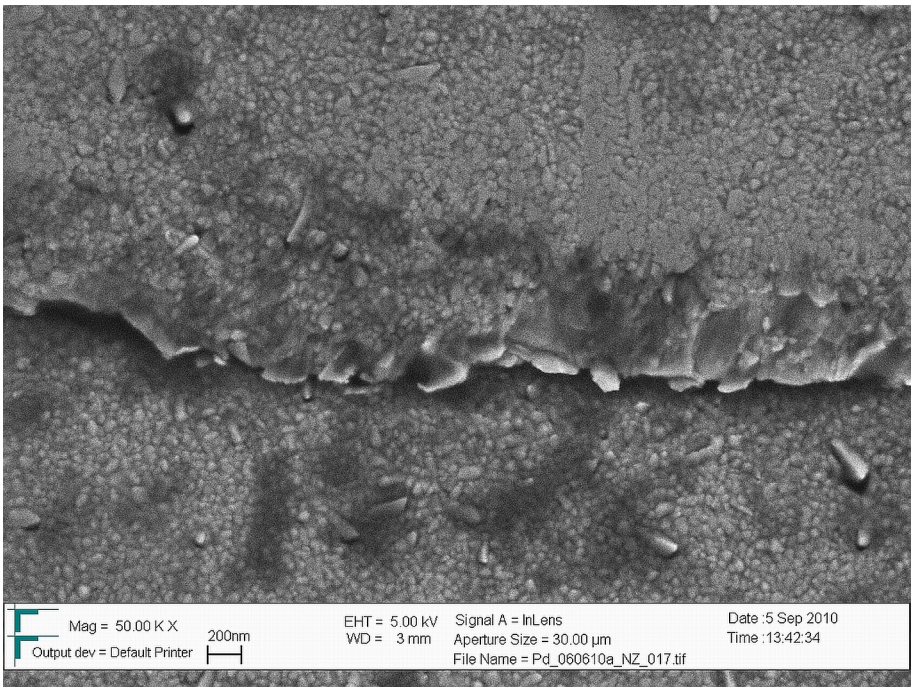

Figure 5.17: Detailed SEM image of a crack in the nc Pd film after 10 % elongation.

5.6 Deformation Mechanisms

The deformation mechanisms present in nc Pd and bimodal structured Pd are on the one hand evaluated by TEM and SEM investigation of the undeformed and deformed films. On the other hand the mechanical properties (especially strain rate sensitivity and activation volume) themselves give information about possible deformation mechanisms, as was explained in chapter 2.1.2.

5.6.1 Nanocrystalline Palladium

In fig. 5.18 a quantitative analysis of grain size and density of twinned grains in the nc Pd films as a function of strain is given. Both values increase almost linearly until 5 % engineering strain and remain unchanged until 10 % engineering strain. The grain size almost doubles from 48 ± 15 nm to 82 ± 24 nm and the density of twinned grains increases from 0.48 % to 2.31 %, which is almost a factor of five.

The reported grain growth and twinning during deformation in the sputtered high purity Pd films are assumed to be stress-driven. By grain growth the material's

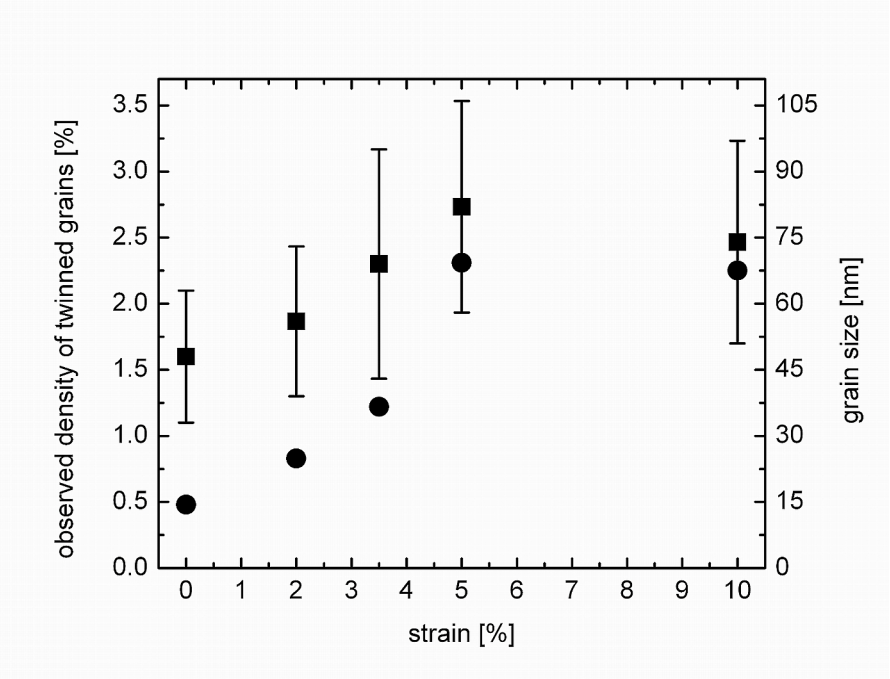

Figure 5.18: Grain size and density of twinned grains of the Pd films as a function of engineering strain.

desire to reduce its overall free energy is compensated. The continuous nature of the growth process is compatible with the kinetics of growth in two dimensions as was reported by Gottstein [73]: "The average in-plane grain radii increase homogenously with $t^{1/2}$ and the shape of the grain size distribution is time-invariant." Comparison of TEM samples prepared from the undeformed tensile sample ends with the initial structure excludes the possibility of temperature-driven grain growth.

Grain growth is supposed to be mediated by grain boundary motion. Four fundamental phenomena are reported by Mishin and coworkers [74]:

- Normal motion (migration): The grain boundary moves in normal direction to its direction vector, parallel to its Burgers Vector.
- Relative translation: The grains move parallel to the grain boundary while the grain boundary moves in normal direction to its direction vector.
- Relative rigid-body translation: The grains move parallel to the unmoved grain boundary.
- Grain rotation: The grains move parallel to the surrounding grain boundary and the lattice misorientation across the grain boundary is changed.

These processes are in good agreement with the observed strain rate sensitivity of $m = 0.22 \pm 0.14$ and activation volume $\Delta V = (1.3 \pm 0.8)$ b^3 compared to the predicted values of $m = 0.5$ and $\Delta V = 1$ b^3. Intragranular slip and dislocation motion ($\Delta V = 10...100$ b^3) as well as dislocation nucleation by grain boundary sources ($\Delta V = \pi$ b^3) are unlikely due to the relative low activation volume observed in the nc Pd films. Additionally no hints of an increased dislocation density in the deformed films could be observed in the TEM investigations. Conventional deformation by forest dislocations ($m << 0.01$) can be excluded as important deformation mechanisms in nc Pd if one compares the strain rate sensitivity values.

The observed good ductility of the Pd films is related to the ability of the grains to grow. In an earlier work by Gianola [19] two types of Al samples were reported, one showed very high strength but poor ductility and no grain growth, the other type showed high ductility and grain growth but reduced strength. It was stated that sample purity plays an important role in the material's ability to facilitate grain growth and is therefore also linked to the material's ductility. This thesis is proven by our results on the high purity Pd films prepared by magnetron sputtering in a UHV system.

Nanocrystalline Pd prepared by inert gas condensation with a grain size of around 14 nm was reported to be extremely brittle in tension, it showed no ductility at

all [75]. In these materials pores are very common, which probably pin the grain boundaries and hinder grain growth. And consequently no stress-driven grain growth was observed in tensile tests in the inert gas condensated Pd.

Twinning is an alternate mode of plastic deformation which is mainly observed in fcc metals with low stacking fault energy, but also in fcc metals with high stacking fault energy if deformed under extreme conditions, like cryogenic temperatures, shock loading, or large strains [16]. Hence, the very high stacking fault energy of Pd ($169\,\mathrm{mJ/m^2}$) [76] explains the low absolute value of the twin density, but nevertheless the relative increase in the density of twinned grains of almost a factor of five points out its importance in deformation processes in nanocrystalline metals. Anyhow the uncertainties in the manual evaluation routine and the low concentrations of the twinned grains weaken our conclusions.

5.6.2 Bimodal Structured Palladium

The mechanical behavior of bimodal structured Pd films shows commonalities as well as differences to the one observed in nc Pd films: The strength is slightly reduced, whereas the deformability increases, which could simply be explained by the increased medium grain size. But concomitantly the activation volume increases ($\Delta V = (4.7 \pm 4.3)\mathrm{b}^3$) and the strain rate sensitivity ($m = 0.07 \pm 0.07$) decreases remarkably.

Figure 5.19 displays a model of the crack propagation in the bimodal microstructure as it was predicted by Han and coworkers [70]. It shows the propagation of a microcrack in a nanostructured sample area with a coarse grained neighbouring sample area. The crack is expected to nucleate in the harder nc area and propagate along the grain boundaries. When the microcrack approaches the coarse grained area, the coarse grains will retard the propagation of the microcrack by blunting it. Finally the coarse grained area itself will crack.

In the bimodal structured Pd films investigated in our study the stress relaxation in the coarse grains is supported by the grain growth of the nc grains, which was observed in our TEM investigations. Consequently, no evidence of cracking was found in the bimodal structured Pd films.

The change in the deformation parameters ΔV and m is most probably due to the different areas which are dominated by different deformation processes. Hence, average values are observed in-between the ones of grain boundary motion and forest dislocations.

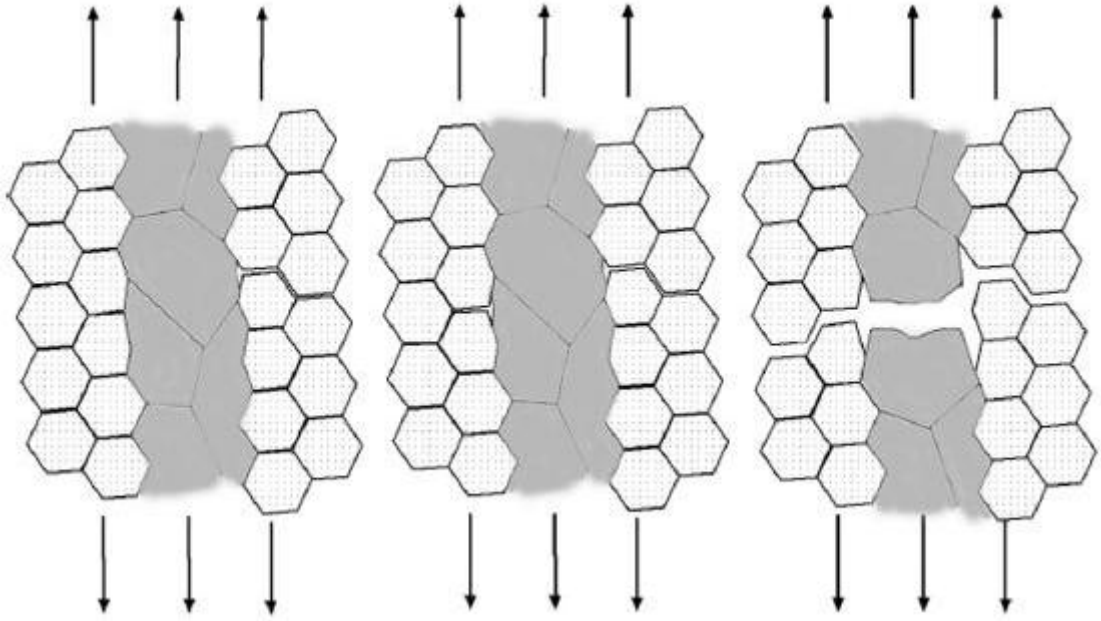

Figure 5.19: Scheme of the crack propagation in the bimodal microstructure [70].

5.7 Conclusions

Nanocrystalline Pd films with a grain size of 48 ± 15 nm and bimodal structured Pd films were sputter-deposited onto flexible polyimide substrates. The samples were tensile tested ex-situ in a miniature tensile testing stage and afterwards the resulting microstructure as a function of maximum strain was investigated using TEM. The conclusions can be summarized as follows:

- Nanocrystalline Pd shows remarkably increased ultimate tensile strength compared to its coarse grained counterpart with 1200 MPa compared to 270 MPa, respectively.
- Strain delocalization by the supporting substrate material helps to achieve high ductility with cracking starting at 10 % engineering strain.
- Bimodal structured Pd shows increased deformability and slightly reduced strength with different deformation processes working in the coarse grains and the nc grains, where the coarse grains secure the ductility and the nc grains carry the load.
- Nanocrystalline and bimodal Pd follow the Hall-Petch relationship with Hall-Petch constants $k_y = 6.47$ MPa mm$^{1/2}$ and $\sigma_0 = 278$ MPa.

- Grain boundary motion and twin formation were identified as deformation processes by microstructural investigation of the deformed nc Pd films. Both grain size and density of twinned grains are increasing almost linearly with strain until the stress saturates and remains stable as the stress does until cracking occurs.

In the next chapter the effect of purity will be studied by alloying the Pd with different contents of Au. Additionally, in-situ tensile testing should give deeper insight into alternate deformation mechanism like shear banding, which might be implied by the shape of the observed cracks in ex-situ SEM.

6 Solid Solution Palladium Gold: Changes in the Mechanical Behavior

The microstructure and mechanical properties of nanocrystalline solid solution PdAu films prepared by magnetron sputtering have been investigated as a function of Au concentration. The films were deposited onto supporting polyimide substrates and tested in tensile mode. Increasing ultimate tensile strength of up to 1.5 GPa but decreasing ductility with increasing Au content were achieved up to 29 at.% Au, by further increasing the Au concentration the trend is reversed. For comparison nanoindentation tests were performed, which showed increasing hardness up to 4.1 GPa with no turning point. In the current chapter the effects of alloying are observed as solid solution hardening and embrittlement.

6.1 Introduction

The strength of nanocrystalline metals can be further increased by the incorporation of foreign atoms in the matrix [3]. The second constituent alters the crystalline structure of the matrix. Moving dislocations have to overcome obstacles in the form of stress fields, precipitates or particles. Consequently, the deformation processes in alloyed metals are assumed to vary from the mechanisms working in the pure constituents.

Another advantage of nc alloys is their enhanced thermal grain size stability [78], which makes them more attractive for industrial applications. It is believed that the low ductility observed in some nc materials is attributed to considerable amount of impurities incorporated during material processing [19]. By investigating alloyed material with low real impurity level by subsequently increasing the amount of substitute atoms, it is possible to examine the effect of impurities.

Magnetron sputtering enables us to produce any desired alloy composition by using co-sputtering: Two (or more) sputtering sources pointing to one sample and

equipped with targets of the different atomic species are operated simultaneously. By adjusting the sputtering power of the sources independently, any desired alloy composition can be deposited easily and with a high reproducibility. This is much more complicated by using inert gas condensation or electrochemical techniques where the deposition conditions have to be adjusted carefully or proper precursers have to be identified. On the other hand, alloys prepared by severe plastic deformation from foils or pellets of different atomic species may suffer from insufficient intermixing of the atoms [77].

The goal of the present chapter is to investigate the changes in the deformation processes active in nanocrystalline PdAu films with increasing Au concentration by tensile testing and nanoindentation. Microstructural analysis was performed by transmission electron microscopy (TEM) and scanning electron microscopy (SEM) before and after tensile deformation. The thermal grain size stability was tested by high temperature X-ray diffraction analysis (HTXRD).

6.2 Experimental

Palladium and PdAu specimens were deposited by RF magnetron sputtering using two 2" diameter planar targets with 99.95% purity (Pd) and 99.99% purity (Au). To enable co-sputtering of two different elements, the two sources are facing the rotating sample manipulator at a distance of 150 mm at an angle of 20°, the rotational speed of the manipulator is 13.5 rpm.

This way 1 μm thick PdAu films were prepared by co-sputtering. In this case, both sources were operated simultaneously. Different alloy compositions were prepared by varying the sputtering power of the Pd and the Au source. To produce samples with low residual stresses below 0.1 GPa, the Ar sputtering gas pressure was adjusted

Pd power [W]	Au power [W]	Au conc. EDX [at.%]	Au conc. RBS [at.%]	Ar pressure [mbar]
60	15	12 ± 1	-	$5.0 \cdot 10^{-3}$
60	20	19 ± 1	-	$5.0 \cdot 10^{-3}$
60	30	29 ± 1	29 ± 3	$5.5 \cdot 10^{-3}$
60	60	52 ± 1	51 ± 5	$5.5 \cdot 10^{-3}$
30	30	72 ± 1	70 ± 7	$5.5 \cdot 10^{-3}$

Table 6.1: Sputter parameters and the resulting Au concentrations measured by EDX and RBS.

according to the results of chapter 4. The gold concentration was estimated by energy dispersive X-ray spectroscopy (EDX) and partly confirmed by Rutherford backscattering spectroscopy (RBS). The sputtering parameters and resulting alloy compositions are displayed in table 6.1.

As substrates again Polyimide Kapton E (Dupont) was used and the substrates were prepared as described in chapter 5.2. Uniaxial tensile tests were carried out with identical conditions as described before.

Nanoindentation tests were performed on 1 μm thick films grown on Si(111) substrates with 50 nm SiO_2 surface, sputtered with identical parameters compared to the tensile test samples. The maximum indentation depth was 100 nm, with an indentation rate of 0.05 s^{-1}, using a Nano Indenter XP with diamond Berkovich tip in CSM mode[1].

The microstructure of the deformed and undeformed samples was investigated by in-plane and cross-sectional TEM imaging, surface SEM imaging and conventional XRD, compare chapter 5.2.

High temperature X-ray diffraction (HTXRD) measurements were performed using a Bruker D 8 Advance equipped with an Anton Paar in-situ heating stage providing protective gas atmosphere (Ar) and a VANTEC area detector[2].

6.3 Microstructural Characterization of Undeformed PdAu Films

In chapter 4 it was shown, that by choosing the appropriate sputtering parameters it is possible to prepare not only pure nanocrystalline Pd but also nanocrystalline solid solution PdAu alloys by magnetron sputtering. As an example in fig. 6.1 and 6.2 cross-sectional bright-field TEM images of solid solution PdAu with 19 at.% and 29 at.% are displayed, respectively.

A perfectly non-columnar nanostructure is observed with grain sizes of 29 ± 21 nm (19 at.% Au) and 41 ± 24 nm (29 at.% Au) in the direction of growth and 47 ± 12 nm (44 ± 13 nm) in-plane, respectively.

[1]The nanoindentation tests were performed by Thomas Neithardt at IAM, Karlsruhe Institute of Technology.

[2]The HTXRD measurements were performed by Azad Darbandi at Joint Research Laboratory Nanomaterials, Technical University of Darmstadt.

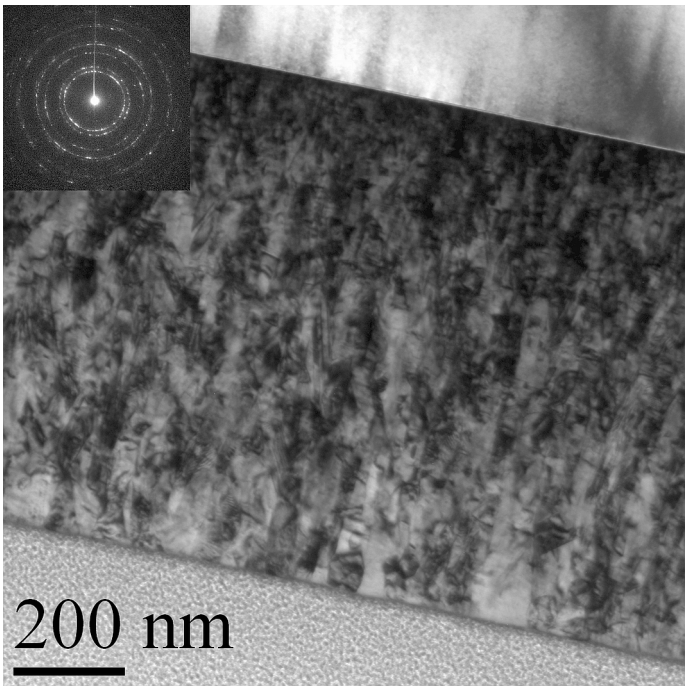

Figure 6.1: Cross-sectional transmission electron microscopy image of an undeformed PdAu film with 19 at.% Au.

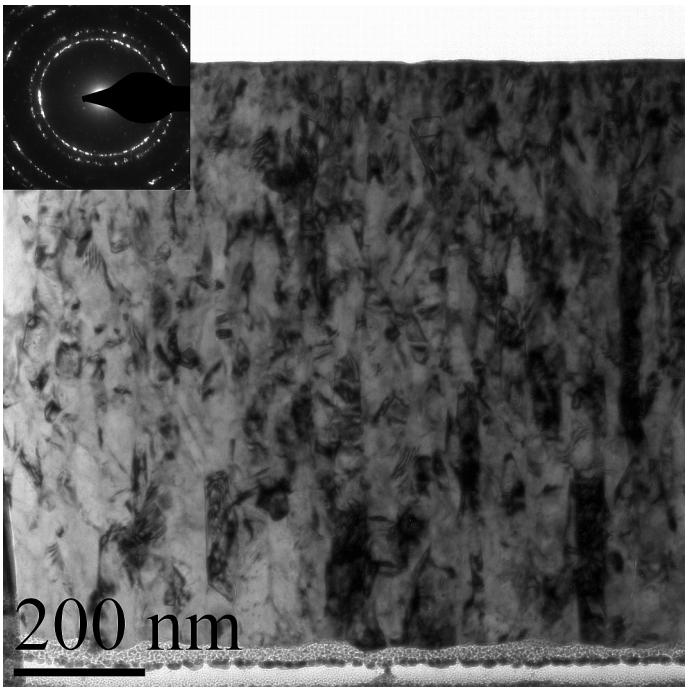

Figure 6.2: Cross-sectional transmission electron microscopy image of an undeformed PdAu film with 29 at.% Au.

The inserted selected area diffraction patterns reveal the polycrystalline structure of the PdAu films. The TEM in-plane grain sizes of undeformed 1-μm-thick PdAu films with 12, 52 and 72 at.% Au were observed to be 42 $\pm$ 14 nm, 36 $\pm$ 9 nm, and 47 $\pm$ 16 nm, respectively.

Figure 6.3 displays XRD patterns of a pure Pd film and PdAu films with Au concentrations of 12, 19, 29, 52, and 72 at.% Au. All the samples show the expected (fcc) structure, but an increase in the (111) texture factor with increasing Au content is observed.

The shift in the peak position is related to the changes in the lattice parameter of the solid solution alloy. The smaller Pd atoms are replaced by bigger Au atoms. Due to the random distribution of this effect in solid solution alloys the average lattice distance measured by XRD measurements increases with increasing Au content. The linear increase of the lattice parameter of the PdAu alloy with increasing Au content is illustrated in figure 6.4 and compared with literature data of solid solution PdAu [63]. In contrast to our EDX measurements the alloys were chemically analyzed in the reference material. The good agreement of alloy composition and lattice parameter confirms our assumption of solid solution PdAu.

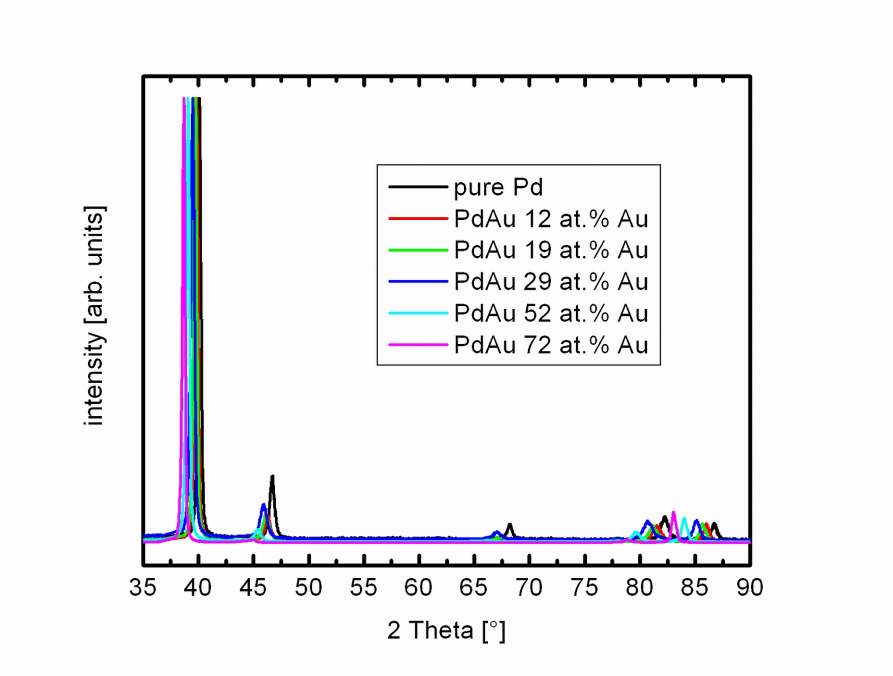

Figure 6.3: XRD measurements of undeformed Pd and PdAu films with 12, 19, 29, 52, and 72 at.% Au.

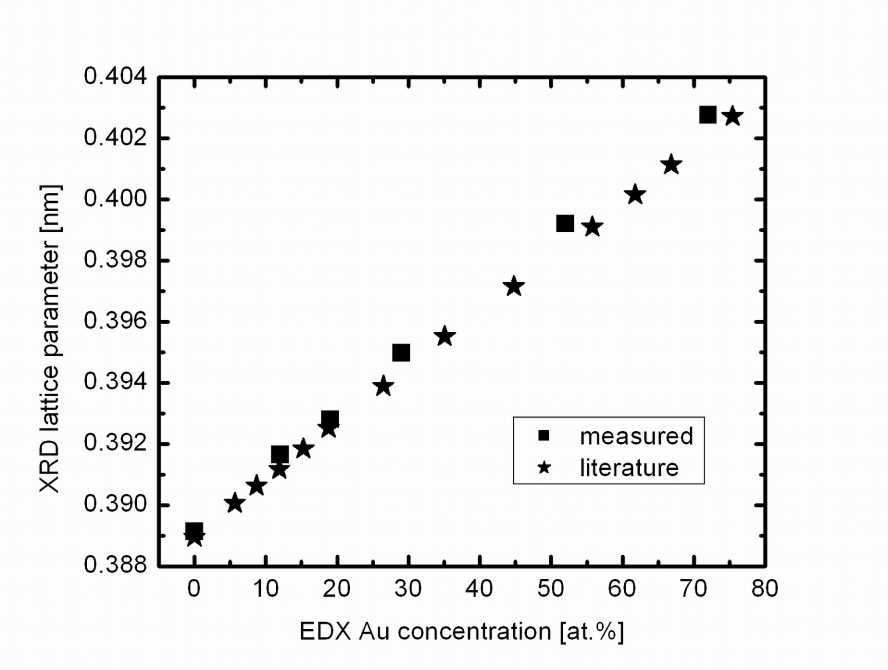

Figure 6.4: Lattice parameters of sputtered nanocrystalline PdAu films determined by XRD and literature values of solid solution PdAu [63].

6.3.1 Temperature Stability

A benefit of nanocrystalline solid solution alloys compared to pure nanocrystalline materials is their enhanced temperature stability. It was demonstrated by Krill and coworkers [78], that nanocrystalline (grain size < 20 nm) solid solution PdZr with only 10 at.% Zr prepared by ball milling showed grain size stability up to 600 °C.

Fig. 6.5 shows HTXRD measurements of the main (111) peak of magnetron sputtered nanocrystalline pure Pd with an initial grain size of 48 ± 15 nm. Measurements were performed every 5 °C, starting from room temperature up to 100 °C under protective Ar atmosphere to avoid incorporation of impurities, especially oxygen. With increasing temperature the peak shifts to smaller diffraction angles, which might be related to the formation of a Pd_2Si layer at the interface between the Pd film and the Si wafer [79]. Grain growth starts quite early at only 70 °C, indicated by the decreasing full width at half maximum (FWHM) of the peak. By further increasing the temperature changes in the peak shape are observed which might be related to impurities.

In figure 6.6 HTXRD measurements of the main (111) peak of nanocrystalline solid solution PdAu films with 12 at.% Au and an initial grain size of 42 ± 14 nm are displayed. The measurement routine was identical to the one explained in the case

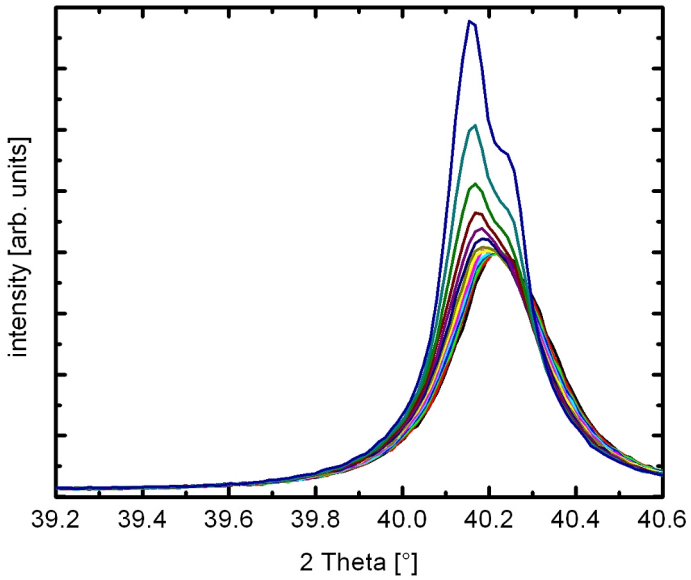

Figure 6.5: In-situ HTXRD measurements of a Pd film: The (111) peak at various temperatures, increasing from RT to 100 °C in steps of 5 °C.

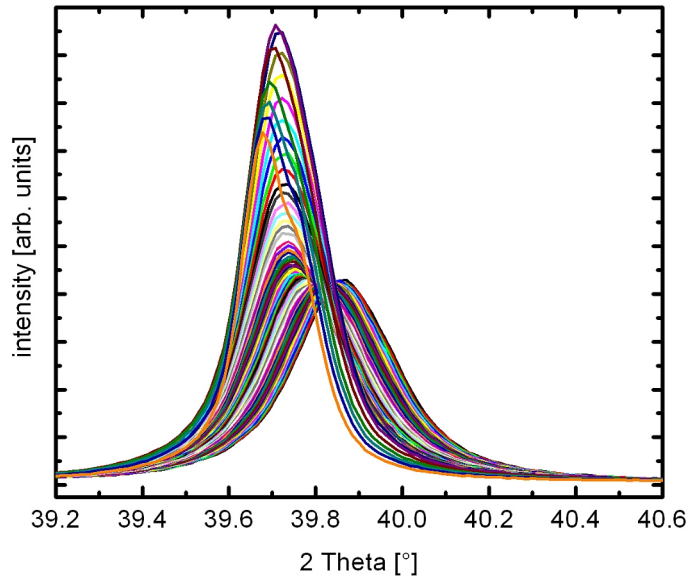

Figure 6.6: In-situ HTXRD measurements of a PdAu film with 12 at.% Au: The (111) peak at various temperatures, increasing from RT to 250 °C in steps of 5 °C.

of pure Pd, but with a maximum temperature of 250 °C. Again the peak position is shifted to smaller diffraction angles with increasing temperature. But in contrast to the previous results, the grain size of the PdAu film is stable up to 115 °C and no changes in the peak shape are observed. Further increasing the Au content to 19 at.% Au does not enhance the temperature stability.

This effect might be resulting from the incorporation of Si, but is more likely due to Au atoms that were segregated at the grain boundaries and start incorporating in the Pd lattice with increasing temperature.

The results of the HTXRD measurements confirm the results of Krill and coworkers [78] that alloying can enhance the temperature stability of the nanocrystalline material, even though alloying Pd with Au is not as sufficient as Zr. By adding Zr to the Pd the driving force for grain growth is suppressed by the decreasing grain boundary energy. This is resulting from segregation of the solute atoms into the grain boundary area, which is a thermodynamic effect. This process is more effective than the kinetic pinning effect in the solid solution PdAu, where the solute atoms pin the grain boundaries, because according to an Arrhenius law, kinetic effects will always be overcome at some elevated temperature [78].

Additionally, room temperature grain growth can be excluded as driving force for grain growth during room temperature deformation of our materials, compare chapter 5.

6.4 Mechanical Properties

The tensile tests have been evaluated as was described in the previous chapter: the films were tensile tested together with the supporting flexible substrate and afterwards the stress-strain-curve of the metallic film was calculated according to equation 5.1.

Figures 6.7 and 6.8 display stress-strain-curves of pure Pd and solid solution PdAu with 12 at.% Au, 19 at.% Au, 29 at.% Au, 52 at.% Au, and 72 at.% Au tested at $5 \cdot 10^{-5}$ s^{-1} strain rate. On the one hand the ultimate tensile strength (UTS) increases by alloying Pd with Au, with a maximum at 19.% Au and 1.5 GPa compared to 1.2 GPa in the case of pure Pd. But on the other hand with increasing Au content the films suffer from increasing embrittlement. Whereas in the pure Pd the stress saturates at 5.0 % strain, in PdAu with 19 at.% the stress increases up to 4.0 % strain and then decreases. The stress decrease is assumed not to be related to real strain softening but is resulting from the supporting substrate, which prevents

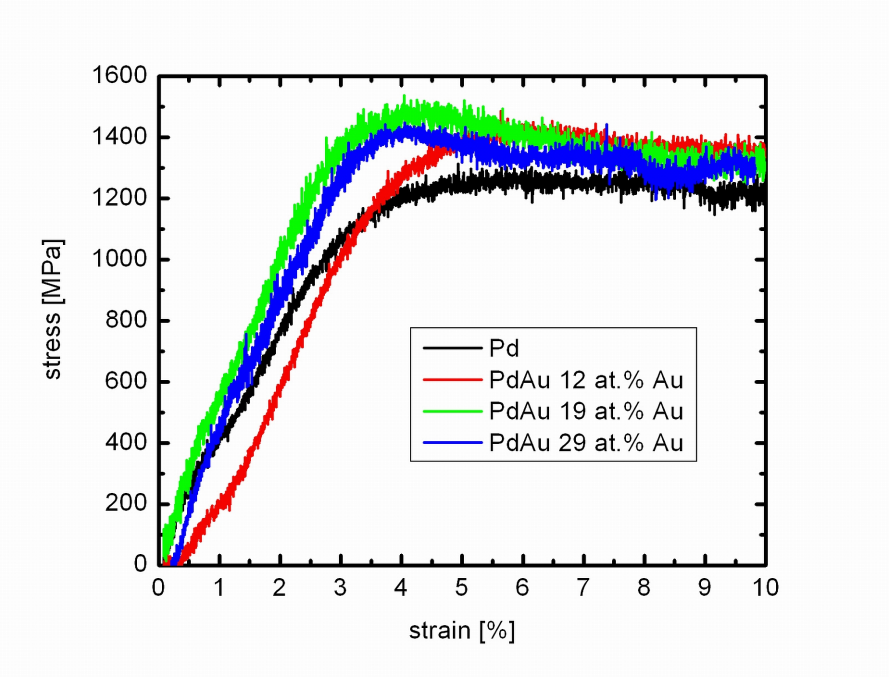

Figure 6.7: Stress-strain curves of pure Pd and solid solution PdAu with 12 at.% Au, 19 at.% Au, and 29 at.% Au tested at $5 \cdot 10^{-5}$ s^{-1} strain rate.

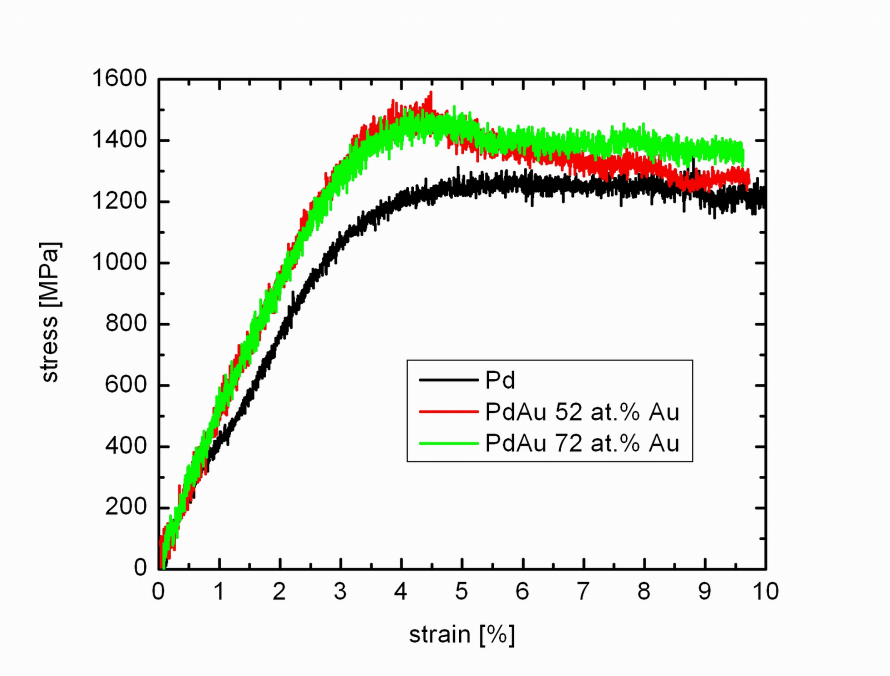

Figure 6.8: Stress-strain curves of pure Pd and solid solution PdAu with 52 at.% Au and 72 at.% Au tested at $5 \cdot 10^{-5}$ s^{-1} strain rate.

Au conc.	grain size [nm]	UTS [MPa]	m	ΔV [b^3]	crack density
0 at.%	47 ± 13	1260 ± 100	0.22 ± 0.14	1.3 ± 0.8	7.5/mm
12 at.%	42 ± 14	1410 ± 100	0.27 ± 0.13	1.0 ± 0.5	12/mm
19 at.%	47 ± 12	1490 ± 100	0.30 ± 0.08	0.8 ± 0.2	11/mm
29 at.%	44 ± 13	1420 ± 100	0.17 ± 0.10	1.5 ± 0.8	13/mm
52 at.%	36 ± 9	1490 ± 100	0.16 ± 0.08	1.5 ± 0.7	11/mm
72 at.%	47 ± 16	1450 ± 100	0.24 ± 0.12	1.1 ± 0.5	14/mm

Table 6.2: List of mechanical properties of solid solution PdAu samples: ultimate tensile strength (UTS) at $5 \cdot 10^{-5}$ s^{-1} strain rate, strain rate sensitivity (m), activation volume (ΔV) and crack density.

the film from total failure even though a close network of cracks is observed in the metallic film.

Table 6.2 summarizes the mechanical properties of the Pd film and the solid solution PdAu films, which were evaluated as described in chapter 5.4. Although the grain size is comparable in all the samples, the UTS increases by adding Au to the Pd and the ductility decreases, which is resulting in an increased crack density. Within the error bars the deformation parameters m and ΔV are comparable in the pure Pd film and the solid solution PdAu films.

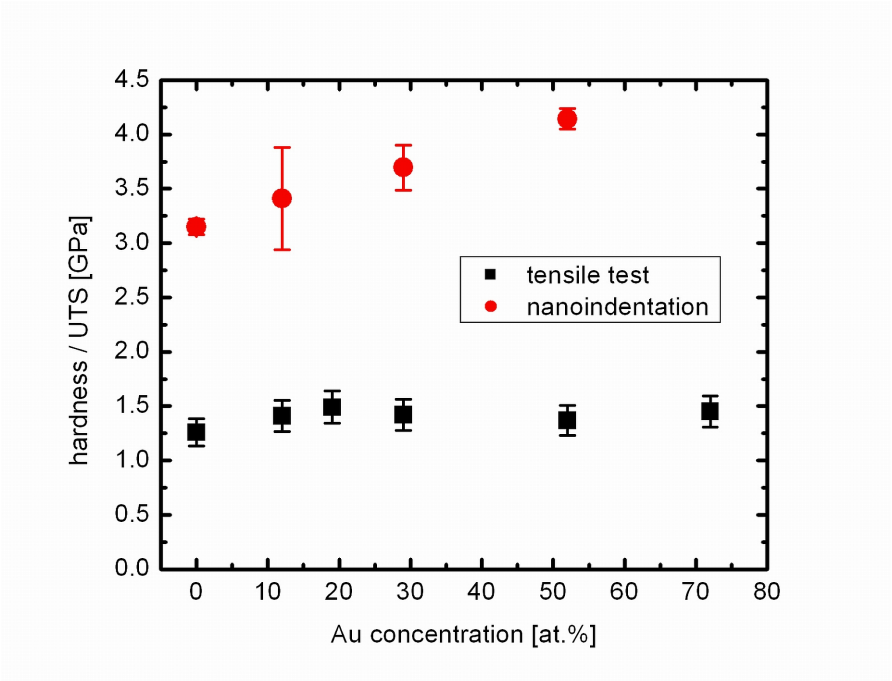

Figure 6.9: Ultimate tensile strength and nanoindentation hardness of pure Pd and solid solution PdAu as a function of Au concentration.

In fig. 6.9 the UTS observed by tensile testing is compared with hardness values H obtained by nanoindentation tests as a function of Au concentration. The UTS increases with increasing Au content and shows its maximum at 19 at.% Au with 1.5 GPa, by further increasing the Au content the UTS decreases to 1.4 GPa where it saturates up to 72 at.%. In contrast to the tensile tests the hardness observed by nanoindentation tests increases almost linearly from 3.1 GPa to 4.1 GPa with increasing Au concentration from 0 at.% Au up to 52 at.% Au. Taking into account the relationship $H = 3 \cdot \mathrm{UTS}$, the absolute values of hardness and UTS match quite well for pure Pd and PdAu with small Au content below 20 at.% Au.

6.5 Microstructural Characterization of Deformed PdAu Films

The microstructural deformation processes were monitored by TEM. In fig. 6.10 and 6.11 the in-plane dark-field micrographs of PdAu films with 12 at.% Au before and after 10 % engineering strain are shown: the initially uniform grain size distribution is maintained after deformation. The grain size increases, but no preferred growth direction is obtained and the size distribution remains lognormal distributed. Additionally the density of twinned grains increases. But compared to the results obtained in the case of pure Pd films, grain growth is reduced, the grain size only increases from 42 ± 14 nm to 60 ± 21 nm, whereas again a distinct increase in the density of twinned grains is observed from 0.47 % to 2.70 %, which is more than a factor of five.

Figures 6.12 and 6.13 display dark-field TEM micrographs of PdAu films with 29 at.% Au before and after 10 % engineering strain. Again no changes in the uniform lognormal distributed grain size distribution are observed during deformation. But by adding 29 at.% Au to the Pd, grain growth is fully disabled: the grain size is stable before (44 ± 13 nm) and after deformation (43 ± 11 nm). Additionally, the increase in the density of twinned grains is not as pronounced as in the pure Pd and the PdAu films with only 12 at.% Au: it increases from 0.86 % to 1.33 %, which is less than a factor of two.

In fig. 6.14 a quantitative analysis of grain size and density of twinned grains before and after tensile deformation to 10 % engineering strain as a function of Au concentration is given. Whereas in the previous chapter grain growth and twin formation were identified as two of the processes present during tensile deformation of pure nc Pd films, this process is vanishing with increasing Au concentration in the nc PdAu films.

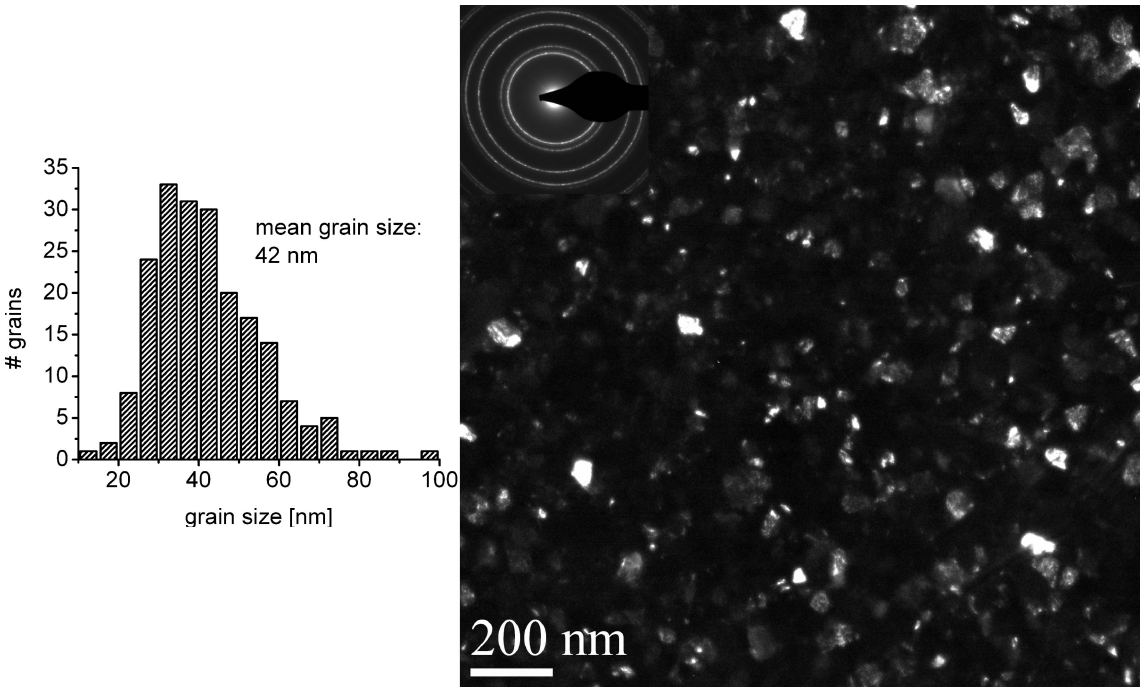

Figure 6.10: In-plane dark field transmission electron microscopy image of the undeformed sputtered PdAu film with 12 at.% Au.

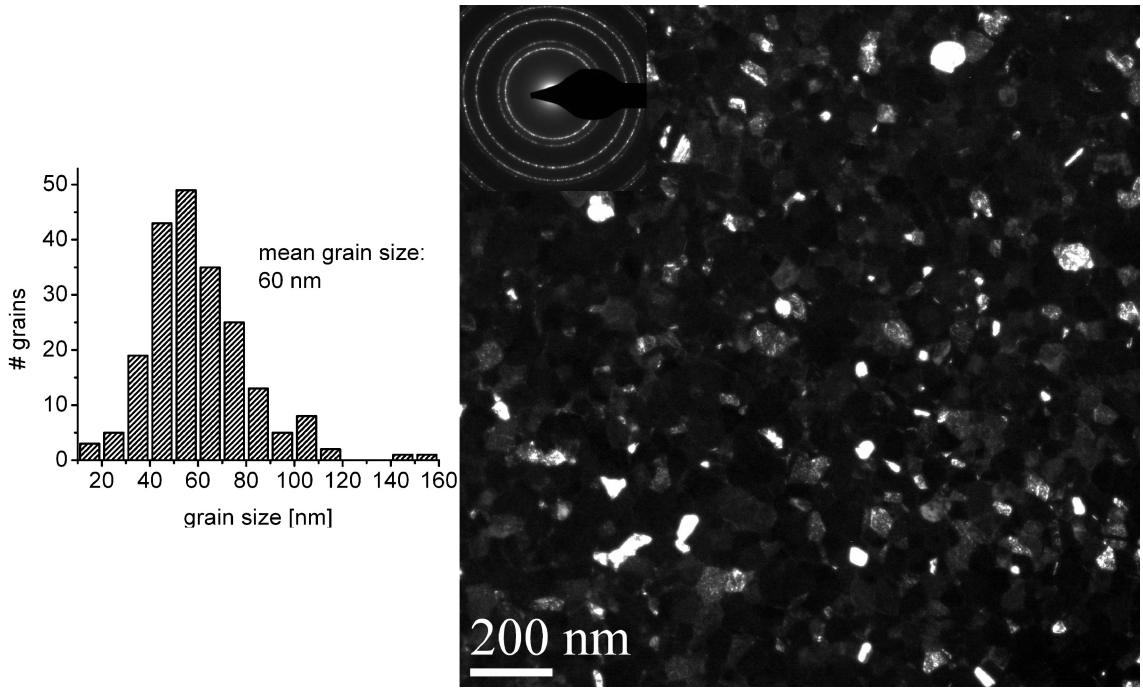

Figure 6.11: In-plane dark field transmission electron microscopy image of the tensiled PdAu film with 12 at.% Au after 10.0 % elongation.

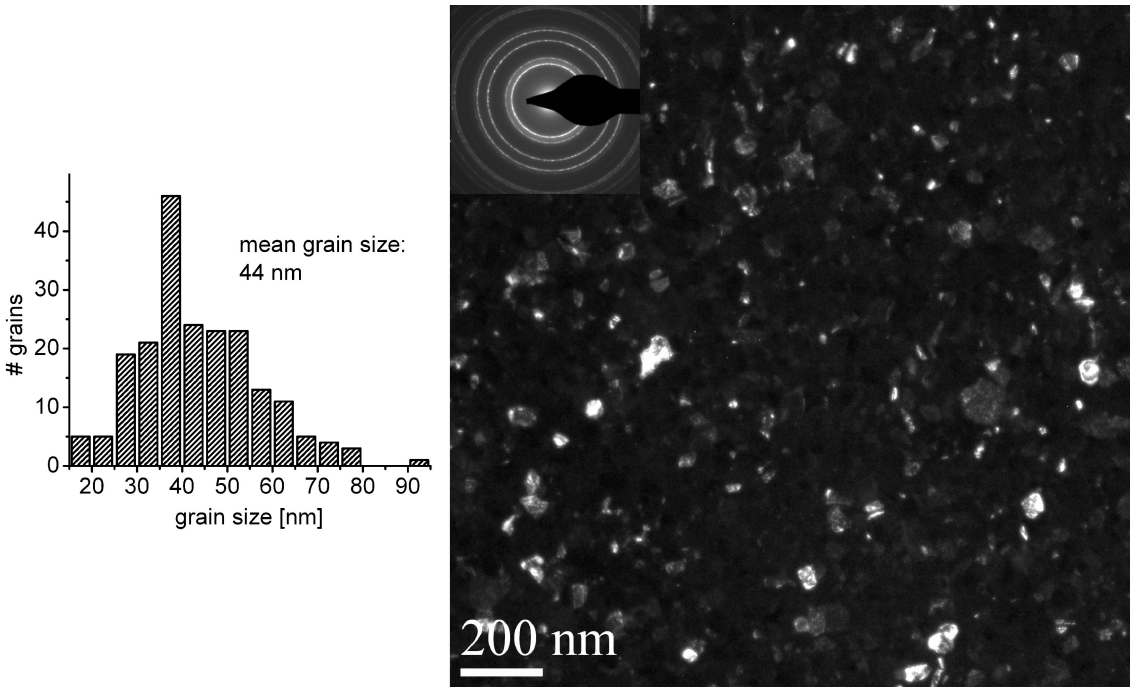

Figure 6.12: In-plane dark field transmission electron microscopy image of the undeformed sputtered PdAu film with 29 at.% Au.

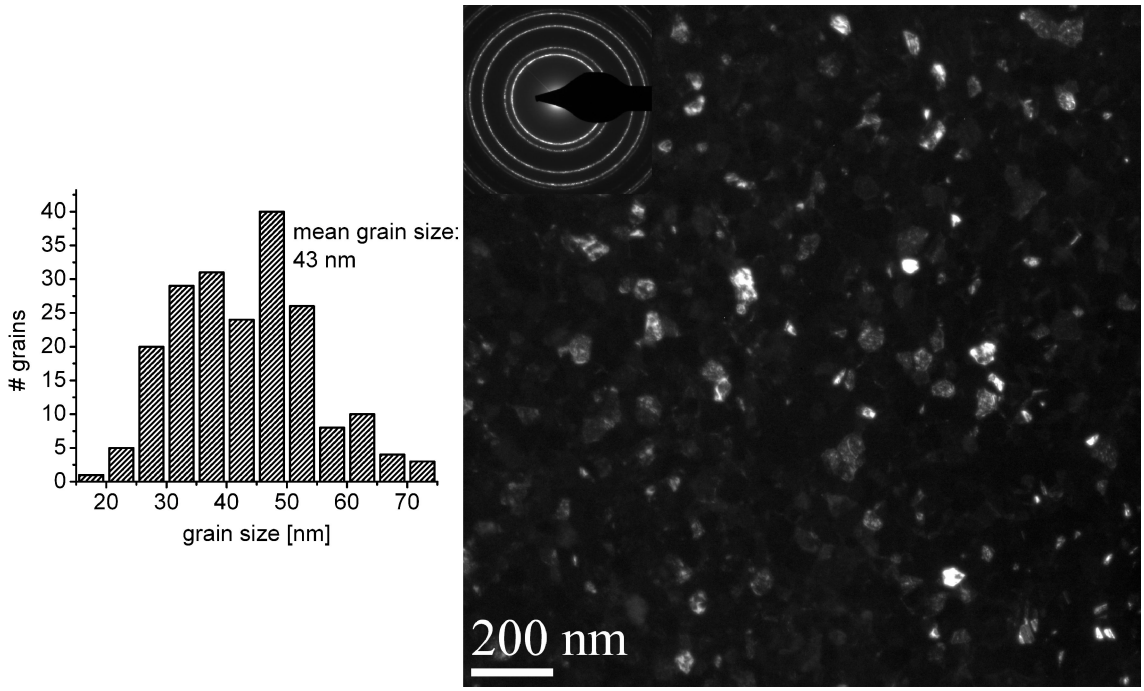

Figure 6.13: In-plane dark field transmission electron microscopy image of the tensiled PdAu film with 29 at.% Au after 10.0 % elongation.

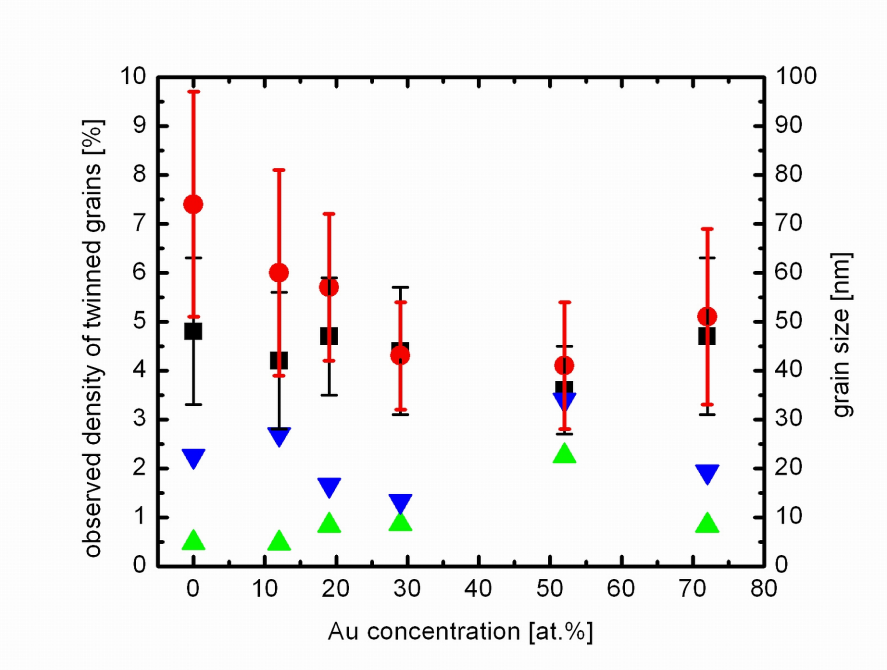

Figure 6.14: Grain size (rectangles and circles) and density of twinned grains (triangles) of the undeformed (black and green) and strained (red and blue) PdAu films as a function of the Au concentration.

At low Au concentration of 12 at.% Au a reduced grain growth compared to pure nc Pd is observed, which further decreases in the PdAu films with 19 at.% Au (grain size increase from 47 ± 12 nm to 57 ± 15 nm) and is fully disabled in films with 29 at.% Au and more. Additionally, the increase in the density of twinned grains is reduced from more than five times in the PdAu film with 12 at.% Au to about two times in PdAu films with 19 at.% Au and more.

Fig. 6.15 displays a SEM top-view image of the deformed PdAu film with 12 at.% Au after 10 % elongation and relaxing the film. At this strain cracking is already quite pronounced with a crack density in the direction of strain of 15 cracks per mm. But the crack orientation is still comparable to the cracks observed in the pure Pd, compare fig. 5.17, again the cracks are mainly oriented in 45 degree to the loading direction. And again cracking starts preferably at weak points where the film adhesion is disturbed by foreign particles at the interface [71]. Only at these weak points the film is fully delaminated from the supporting substrate. Even after relaxing, the gap in the film is not closed.

Fig. 6.16 displays a SEM top-view image of the deformed PdAu film with 29 at.% Au after 10 % elongation and relaxing the film. The crack density in the direction of strain (21 cracks per mm) is increased compared to the one detected in the deformed PdAu films with 12 at.% Au. Additionally, the crack orientation is changed, the

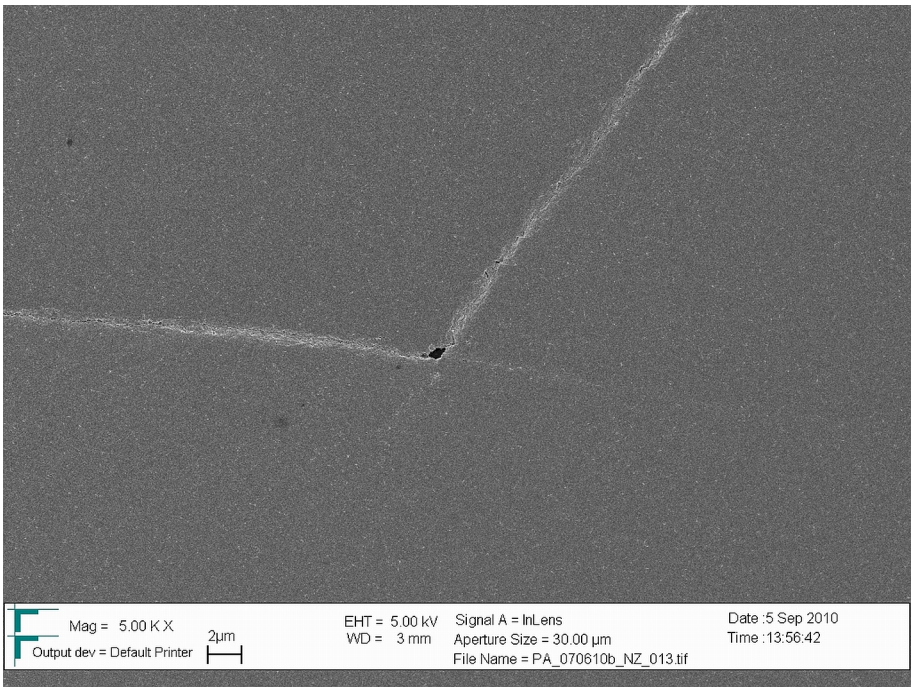

Figure 6.15: Detailed SEM image of a crack in the PdAu film with 12 at.% Au after 10 % elongation.

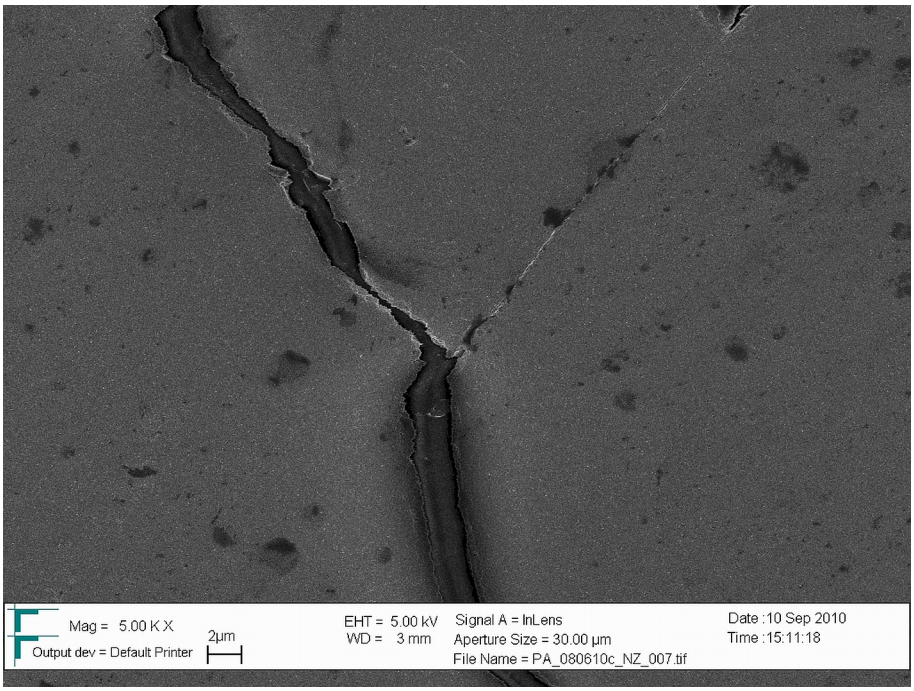

Figure 6.16: Detailed SEM image of a crack in the PdAu film with 29 at.% Au after 10 % elongation.

cracks are almost in-line perpendicular to the loading direction. Even after relaxing, the film is almost fully delaminated from the supporting substrate along the cracks, the gap in the film is much more pronounced than in the PdAu films with 12 at.% Au.

The changes in the cracking behaviour by alloying the Pd with an increasing amount of Au are consistent with the stress-strain curves observed by tensile testing: there a shift of the stress maximum to lower strains was observed, which matches with the increased crack density and confirms the assumption, that the stress maximum is related to the appearance of the first crack and the following stress drop points to a developing close network of cracks. But not only the growing crack density in the deformed PdAu films indicates increasing embrittlement by adding more Au to the PdAu alloy, the change in the crack direction from 45 degree to the loading direction oriented zick-zack structures, which might be attributed to shear deformation, to lines perpendicular to the loading direction gives also evidence of embrittlement.

6.6 Solid Solution Hardening

The increasing ultimate tensile strength in the PdAu compared to pure Pd is attributed to solid solution hardening, caused by both parelastic and dielastic interaction [10]. The elastic modulus of Au is with 29 GPa about 40 % smaller than the elastic modulus of Pd with 48 GPa [82] and the atomic radius of the Au atom is with 144 pm slightly bigger than the Pd atom's radius of 138 pm [83]. The solute atoms imply stress fields in the matrix and thereby hinder dislocation glide and increase the material's strength.

In case of solid solution PdAu the maximum repelling force experienced by the moving dislocation in the solid solution is given by [3]:

$$F_{max} = F^{p}_{max} + F^{d}_{max}, \tag{6.1}$$

where F^{p}_{max} is the parelastic force and F^{d}_{max} is the dielastic force.

The critical stress $\Delta\tau_c$ required to enable plastic flow is related to the maximum repelling force via:

$$\Delta\tau_c \cdot b \; l_F = F_{max}, \tag{6.2}$$

with b the Burger's vector and l_F the mean free dislocation length. The mean free dislocation length is called Friedel length and given by:

$$l_F = \sqrt[3]{\frac{6E_v}{\Delta\tau_c \; c_F \; b}}, \tag{6.3}$$

where $E_v \cong 0.5Gb^2$ is the dislocation energy and c_F is the number of second constituents per area in the glide plane. By inserting equation (6.3) in equation (6.2) one obtains:

$$\Delta\tau_c = \frac{G}{\sqrt{3}} \left(\frac{F_{max}}{G \; b^2} \right)^{3/2} \sqrt{c^a}. \tag{6.4}$$

With equations (6.1), (2.15) and (2.17) this results in:

$$\Delta\tau_c = \frac{G}{\sqrt{3}} \left(|\delta| + \frac{1}{20} \, |\eta| \right)^{3/2} \sqrt{c^a}. \tag{6.5}$$

Figure 6.17 displays the hardness values measured by nanoindentation plotted against the square root of the Au concentration. Within the error bars the linear increase of the hardness with increasing square root of the Au concentration confirms the linear increase of the critical stress $\Delta\tau_c$ with increasing square root of the Au concentration.

By adding more than 19 at.% Au to the nc Pd the UTS of the tensile tested PdAu films decreases and saturates. This effect is on the one hand related to the increased embrittlement in the PdAu films, compare table 6.2. On the other hand is coarse grained Au with 100 MPa UTS [84] much softer than coarse grained Pd with 270 MPa UTS [72]. Hence, adding a small amount of Pd to Au will increase the UTS of the alloy compared to the pure Au. Adding more Pd will further increase the UTS, according to equation 6.5. Consequently, a reversal in the UTS would be expected at a certain composition. Tensile tests suggest this composition is in-between 19 and 29 at.% Au.

Surprisingly, the nanoindentation tests show no hardness reversal up to 52 at.% Au. This implies that maybe embrittlement hinders the observation of the stress reversal by tensile tests. Embrittlement is not that critical to hardness tests, because the hardness test does not suffer from single defects in the film but measures the hardness of a volume of the material.

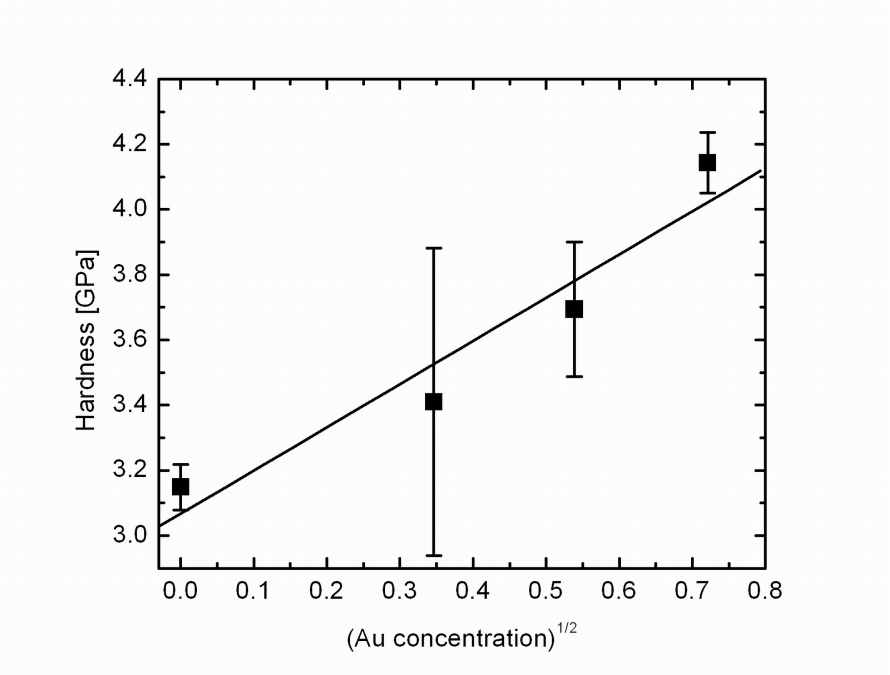

Figure 6.17: Hardness measured by nanoindentation plotted against the square root of the Au concentration.

Another aspect is the limited accuracy of the tensile tests on substrates. The small number of tests and the large error bars make reliable statements on the small differences between different PdAu alloys troublesome. Due to their statistical accuracy the results of the nanoindentation tests are more reliable.

6.7 Deformation Mechanisms

The enhanced temperature stability of the solid solution PdAu can be attributed to solute atoms which hinder grain growth by pinning grain boundaries. This effect influences the deformation processes as well. We showed in chapter 5 that stress-driven grain growth is important to enable plastic deformation. The observed limited or even suppressed grain growth in the solid solution PdAu is most probably caused by the solute atoms, which pin the grain boundaries, hinder grain growth and thereby cause embrittlement.

The Hall-Petch relationship explains the increased strength of the nanocrystalline Pd and PdAu compared to their coarse grained counterparts. The increase in strength of the solid solution nanocrystalline PdAu compared to the pure nanocrystalline Pd

on the other hand is not related to Hall-Petch, because the initial grain size of Pd and PdAu samples is comparable.

We did not observe a considerable change in the twin density in the solid solution PdAu compared to the pure nc Pd.

The deformation parameters m and ΔV give no hint to significant changes in the deformation processes by alloying Au to the nc Pd films: they remain almost constant independent from the Au concentration. The increasing brittleness might be resulting from Au atoms that hinder grain boundary motion as the dominating deformation process.

As was described earlier we observed embrittlement and strengthening with increasing Au concentration in the nc PdAu films. This effect is contradictory to the results given by Valiev [7], who stated that by decreasing the grain size to nanometer size high ductility and strength are possible. We assume that his results are not only related to the small grain size, but also to a high density of crystal defects present in the SPD processed material, which was not observed in the sputtered nc Pd and PdAu films.

The increasing embrittlement with increasing Au concentration matches the results by Hemker and coworkers [19]: They stated that lacking ductility in many nc materials might be related to a high density of impurities incorporated during fabrication of the nc material. In the pure sputtered nc Pd the impurity level is pretty low, as was proven in chapter 4, and consequently a relatively high ductility was observed. By alloying the Pd with Au we were able to control the amount of foreign atoms and verified the assumption of Hemker and coworkers [19], that the foreign atoms inhibit ductility.

6.8 Conclusions

Nanocrystalline PdAu films with Au concentrations varying from 12 at.% Au to 72 at.% Au and comparable grain sizes were sputter deposited onto flexible polyimide substrates. The samples were tensile tested ex-situ in a miniature tensile testing stage and afterwards the resulting microstructure was investigated using TEM. Additionally films were tested by nanoindentation. The conclusions can be summarized as follows:

- Nanocrystalline PdAu films show an increased thermal grain size stability compared to pure nc Pd films. The starting point of temperature driven grain growth is shifted from 70 °C to 115 °C.

- The alloyed nanocrystalline PdAu films show an increased ultimate tensile strength compared to pure nanocrystalline Pd with 1.5 GPa compared to 1.2 GPa, respectively. UTS is increasing with increasing Au concentration up to 19 at.% Au and then decreasing to a constant value of roughly 1.4 GPa.
- Solid solution hardening causes the increased strength of the nc solid solution PdAu compared to pure nc Pd.
- Embrittlement is developing with increasing Au concentration during tensile testing.
- By nanoindentation testing an almost linear increase in hardness was observed with increasing square root of the Au concentration up to 52 at.% Au, matching the critical stress $\Delta\tau_c$ required for dislocations to overcome the stress fields of solute atoms.
- The amount of grain growth during tensile deformation is decreasing with increasing Au concentration. In pure nc Pd the grain size increases by almost a factor of two. In PdAu with 12 at.% Au the grain size increases by 50%. Above 29 at.% Au in the PdAu no more grain growth is observed. This effect is caused by solute Au atoms, which pin the grain boundaries.
- There is no general change in the deformation parameters by alloying the nc Pd with Au, independent of the Au concentration grain boundary motion is dominating the deformation.

7 Conclusion and Outlook

7.1 Conclusion

In the present thesis the mechanical properties of nanocrystalline palladium films and solid solution palladium gold films prepared by magnetron sputtering have been investigated in order to understand the underlying deformation processes. In comparison to coarse grained metals, where the deformation is carried almost exclusively by dislocation glide, in nanocrystalline metals many different deformation mechanisms have already been observed in different metals [6, 9, 10, 12]. One can conclude that it is not possible to extract one single deformation process working in nanocrystalline metals but there are various processes working simultaneously.

The initial step of this work was to prepare proper testing material with nanocrystalline structure, high density, negligible amount of crystal defects, low impurity level and low residual stresses. UHV magnetron sputtering was the method of choice, because we demonstrated that by adjusting the sputtering parameters in a proper way, all these requirements can be fulfilled reproducibly. 500 nm thick pure Pd films and solid solution PdAu films were prepared by interrupted deposition and co-deposition, respectively. We focussed on the relationship between structural properties and residual stresses and the pressure of the Ar-sputtering gas and observed the following results:

- A sharp transition from compressive to highly tensile stresses is observed, followed by a gradual decrease in the tensile stress regime with increasing Ar-sputtering gas pressure.
- The observed critical pressures for the compressive-tensile stress transition match with the values predicted by Thornton and Hoffman [61].
- The microstructural investigation confirms the results shown for other materials such as W, Be and AlN: columnar structures at highest tensile stress and the beginning of a density reduction of the film with decreasing tensile stress or increasing pressure of the sputtering gas.

- A novelty was observed at the lowest pressures for Pd as well as for PdAu: the grain structure was still nanocrystalline with grain sizes of about 30 nm.

Subsequently the microstructure and mechanical properties of 1-μm-thick nanocrystalline Pd films and bimodal structured Pd films have been investigated as a function of strain. Therefore, the samples were deposited onto supporting flexible polyimide substrates (Dupont Kapton E, 50 μm thick), to stabilize the delicate films especially during handling. A special thin film sample clamping was designed for the tensile tests. The microstructure of the undeformed as well as of the deformed films was investigated by transmission electron microscopy. The results can be summarized as follows:

- Nanocrystalline Pd shows remarkably increased ultimate tensile strength compared to its coarse grained counterpart with 1200 MPa compared to 270 MPa, respectively.
- Strain delocalization by the supporting substrate material helps to achieve high ductility with cracking starting at 10 % engineering strain.
- Bimodal structured Pd shows increased ductility and slightly reduced strength with different deformation processes working in the coarse grains and the nc grains, where the coarse grains secure the ductility and the nc grains carry the load.
- Nanocrystalline and bimodal Pd follow the Hall-Petch relationship with Hall-Petch constants $k_y = 6.47$ MPa mm$^{1/2}$ and $\sigma_0 = 278$ MPa.
- Grain boundary motion and twin formation were identified as deformation processes by microstructural investigation of the deformed nc Pd films. Both grain size and density of twinned grains are increasing almost linearly with strain until the stress saturates and remains stable as the stress does until cracking occurs.

Finally, the microstructure and mechanical properties of 1-μm-thick nanocrystalline solid solution PdAu films with comparable grain sizes have been investigated as a function of Au concentration. By adding a defined amount of Au to the very pure sputtered Pd samples the effect of impurity atoms on the deformation processes can be studied. Additionally, nanocrystalline alloys are attractive candidates for industrial application due to their increased thermal grain size stability, but their response to mechanical deformation is only vaguely understood. The resulting changes in the mechanical response due to alloying Pd with Au can be summarized as follows:

- Nanocrystalline PdAu films show an increased thermal grain size stability compared to pure nc Pd films. The starting point of temperature driven grain growth is shifted from 70 °C to 115 °C.
- Due to solid solution hardening the alloyed nanocrystalline PdAu films show increased ultimate tensile strength compared to pure nanocrystalline Pd with 1.5 GPa compared to 1.2 GPa, respectively. UTS is increasing with increasing Au concentration up to 19 at.% Au and then decreasing to a constant value of roughly 1.4 GPa.
- Embrittlement is developing with increasing Au concentration during tensile testing.
- By nanoindentation testing an almost linear increase in hardness was observed with increasing square root of the Au concentration up to 52 at.% Au, matching the critical stress $\Delta\tau_c$ required for dislocations to overcome the stress fields of solute atoms.
- The amount of grain growth and twinning during tensile deformation is decreasing with increasing Au concentration. In pure nc Pd the grain size increases by almost a factor of two. In PdAu with 12 at.% Au the grain size increases by 50%. Above 29 at.% Au in the PdAu no more grain growth is observed. This effect is caused by solute Au atoms, which pin the grain boundaries and thereby hinder grain growth.
- There is no general change in the deformation parameters by alloying the nc Pd with Au, independent of the Au concentration grain boundary motion is dominating the deformation.

7.2 Outlook

The direct proof of the deformation processes indicated by the measurement results of this work is lacking from the matter of fact that the microstructural investigation was generally conducted post-mortem. Especially TEM analysis might suffer from preparational effects occurring during thinning of the deformed samples. Grain growth and twinning can be excluded by statistical analysis of deformed and undeformed samples and could therefore be analyzed in this work. But the investigation of deformation processes on the atomic level by HRTEM might misinterpret single events, which cannot be statistically evaluated.

On the other hand, deformation processes have dynamic character and some effects may not be observable in post-mortem analysis. Therefore, in-situ tensile tests in

the TEM are currently under preparation, which will hopefully give direct proof of grain boundary motion and twin formation. These tests will be assisted by orientation imaging at low precession angles (AStar by NanoMegas) in micro-probe STEM mode, which will allow automatic analysis of twins and grain size distribution with improved statistics. HRTEM imaging of selected events might identify deformation processes on the atomic level.

Cracking behaviour and surface effects will be investigated by in-situ SEM measurements. This technique enables us to detect even very small developing cracks, which might close after relaxing of the sample, which will help to detect the starting point of crack formation. Additionally, surface effects can be identified (like shear lines) and later on be investigated by TEM using FIB target preparation.

Despite from a closer investigation of the nanocrystalline Pd and PdAu films, other materials could also give deeper insight in deformation processes on the nanoscale level: Nano-twinned structures are promising candidates, they show an increased strength like nanocrystalline materials, but do not suffer as much from embrittlement. It was already demonstrated that these materials can also be prepared by magnetron sputtering, but the underlying deformation processes are not fully understood up to now.

Bibliography

[1] E.O. Hall, Proceedings of the Physical Society, Ser. B **64**, 747 (1951).

[2] N.J. Petch, J. Iron and Steel Institute, **174**, 25 (1953).

[3] Günther Gottstein, *Physikalische Grundlagen der Materialkunde*, Springer Verlag, Berlin, 2007.

[4] William D. Callister, Jr., *Materials Science and Engineering: An Introduction*, John Wiley & Sons, Inc., New York, 2007.

[5] Rolf E. Hummel, *Understanding Materials Science: History, Properties, Applications, Second Edition*, Springer Verlag, Berlin, 2004.

[6] M. Dao, L. Lu, R.J. Asaro, J.T.M. De Hosson, and E. Ma, Acta Mat. **55**, 4041 (2007).

[7] R. Valiev, Nature **419**, 887 (2002).

[8] L. Lu, M.L. Sui, and K. Lu, Science **287**, 1463 (2000).

[9] DFG Forschergruppe 714, *Plastizität in nanokristallinen Metallen und Legierungen, Fortsetzungsantrag 2009-2012*, 2009.

[10] A.S. Argon, *Strengthening Mechanisms in Crystal Plasticity*, Oxford, New York, 2008.

[11] D. Calliard, J.L. Martin, *Thermally activated mechanisms in crystal plasticity*, Pergamon, Amsterdam, 2003.

[12] Lilia Kurmanaeva, *Design and Mechanical Performance of Fully Dense Nanocrystalline Noble Metals on the Basis of Pd, Pd-Ag and Pd-Au*, Ph. D. thesis, University of Ulm, 2011.

[13] H. Hahn, P. Mondal, K.A. Padmanabhan, NanoStructured Materials **9**, 603 (1997).

[14] M. Legros, D.S. Gianola, K.J. Hemker, Phys. Rev. B **56**, 3380 (2008).

[15] R.Z. Valiev, I.V. Alexandrov, Y.T. Zhu and T.C. Lowe, J. Mater. Res. **17**, 5 (2002).

[16] K.S. Kumar, H. Van Swygenhoven, and S. Suresh, Acta Mat. **51**, 5743 (2003).

[17] A. Castrup, C. Kübel, T. Scherer, H. Hahn, JVST A **29**, 021013 (2011).

[18] A.M. Hodge, Y.M. Wang, T. W. Barbee Jr., Mater. Sci. Eng. A **429**, 272 (2006).

[19] D.S. Gianola, S. Van Petegem, M. Legros, S. Brandstetter, H. Van Swygenhoven, and K.J. Hemker, Acta Mat. **54**, 2253 (2006).

[20] L. Kurmanaeva, Yu. Ivanisenko, J. Markmann, R.Z. Valiev, and H.-J. Fecht, Mater. Sci. For. **584-586**, 182 (2008).

[21] D.S. Gianola and C. Eberl, JOM **61**, 24 (2009).

[22] F. Macionczyk, W. Brückner, W. Pitschke, and G. Reiss, J. Mater. Res. **13**, 2852 (1998).

[23] D.Y.W. Yu and F. Spaepen, J. Appl. Phys. **95**, 2991 (2004).

[24] M.A. Haque and M.T.A. Saif, Sensors and Actuators A **97-98**, 239 (2002).

[25] Patric A. Gruber, *Mechanical Properties of Ultra Thin Metallic Films Revealed by Synchrotron Techniques*, Ph. D. thesis, University of Stuttgart, 2007.

[26] M. Ames, M. Grewer, C. Braun, and R. Birringer, Mater. Sci. Eng. A **546**, 248 (2012).

[27] Daimler AG, http://www.daimler.com (20.10.2011).

[28] R.Z. Valiev, I.P. Semenova, E. Jakushina, V.V. Latysh, H. Rack, T.C. Lowe, J. Petruželka, L. Dluhoš, D. Hrušák, J. Sochová, Mater. Sci. For. **584-586**, 49 (2008).

[29] C. Suryanarayana and C.C. Koch, Hyperfine Interactions **130**, 5 (2000).

[30] Daimler AG, German patent application, DE102010049840A1 (27.11.2009).

[31] TITAN, *Product Data*, http://www.fei.com (13.12.2010).

[32] David B. Williams and C. Barry Carter, *Transmission electron microscopy: a textbook for materials science*, Plenum Press, New York, 1996.

[33] Philips, *CM 200 Super Twin, Manual*, 1995.

[34] Karlsruhe Nano Micro Facility, *Technologies*, http://www.knmf.kit.edu/ (13.12.2010).

[35] Gatan, *Product Data*, http://www.gatan.com (10.01.2011).

[36] Bruker AXS, http://www.bruker-axs.com (07.09.2006).

[37] Sonja Heitmann, *Cobalt / Copper Multilayers: Interplay of Microstructure and GMR and Recrystallization as the Key towards Temperature Stability*, Ph. D. thesis, University of Bielefeld, 2004.

[38] Sven Kämmerer, *The Heusler alloy Co_2MnSi in thin films*, Ph. D. thesis, University of Bielefeld, 2004.

[39] E. Macherauch, H. Wohlfahrt, U. Wolfstieg, Härtereitechn. Mitteilungen **28**, 201 (1973).

[40] P. Müller, E. Macherauch, Z. ang. Phys. **13**, 305 (1961).

[41] H.J. Bunge, *Mathematische Methoden der Texturanalyse*, Akademie-Verlag, Berlin, 1969.

[42] W.C. Oliver, G.M. Pharr, J. Mater. Res. **7**, 1564 (1992).

[43] MTS Nano Instruments, http://www.mtsnano.com (14.12.2010).

[44] Andrea Hodge, *Personal notification*, 2010.

[45] J. Chen, *Introduction to Scanning Tunneling Microscopy*, Oxford University Press, Oxford, 1993.

[46] Omicron NanoTechnology GmbH, http://www.omicron.de (14.12.2010).

[47] Veeco Instruments, *Dektak 6M Manual*, 2002.

[48] K. Oura, V.G. Lifshits, A.A. Saranin, A.V. Zotov, M. Katayama, *Surface Science: An Introduction*, Springer-Verlag, Berlin, 2003.

[49] K. Siegbahn, *Electron Spectroscopy for Atoms, Molecules and Condensed Matter*, Nobel lecture, 1981.

[50] SPECS Surface Nano Analysis GmbH, http://www.specs.de (23.01.2011).

[51] Y. Chen, J. Au, P. Kazlas, A. Ritenour, H. Gates, and M. McCreary, Nature **423**, 136, (2003).

[52] G.H. Gelinck, H. Edzer, A. Huitema, E.V. Veenendaal, E. van Cantatore, L. Schrijnemakers, J. van der Putten, T.C.T. Geuns, M. Beenhakkers, J.B. Giesbers, B.H. Hiusman, E.J. Meijer, E.M. Benito, F.J. Touwslager, A.W. Marsman, B.J.E. van Rens, and D.M. De Leeuw, Nat. Mater. **3**, 106 (2004).

[53] E.R. Post, M. Orth, P.R. Russo, and N. Gershenfeld, IBM Syst. J. **39**, 840 (2000).

[54] E. Bonderover and S. Wagner, IEEE Electron Device Lett. **25**, 295 (2004).

[55] S. Wagner, S.P. Lacour, J. Jones, P.H.I. Hsu, J.C. Sturm, T. Li, and Z.G. Suo, Physica E **25**, 326 (2004).

[56] C.J. Brabec, Sol. Energy Mater. Sol. Cells **83**, 273 (2004).

[57] P.A. Gruber, E. Arzt, and R. Spolenak, J. Mater. Res. **24**, 1906 (2009).

[58] T.W. Barbee Jr., in: L. Chang, B.C. Giessen (Eds.), Synthetic Modulated Structures, Academic Press, New York, 1985, p. 313.

[59] J.A. Thornton, and D.W. Hoffman, Thin Solid Films **171**, 5 (1989).

[60] A.J. Detor, A.M. Hodge, E. Chason, Y. Wang, H. Xu, M. Conyers, A. Nikroo, and A. Hamza, Acta Mater. **57**, 2055 (2009).

[61] D.W. Hoffman, J. Vac. Sci. Technol. A **12**, 953 (1994).

[62] U.F. Kocks, C.N. Tomé, and H.R. Wenk, *Texture and Anisotropy*, Cambridge University Press, Cambridge, 1998.

[63] W.B. Pearson, *A Handbook of Lattice Spacings and Structures of Metals and Alloys*, Pergamon Press, Oxford, 1967, vol. 2

[64] H. Windischmann, J. Vac. Sci. Technol. A **9**, 2431 (1991).

[65] Y.G. Shen, Y.W. Mai, Q.C. Zhang, D.R. McKenzie, W.D. McFall, and W.E. McBride, J. Appl. Phys. **87**, 177 (2000).

[66] M. Pletea, R. Koch, H. Wendrock, R. Kalthofen, and O.G. Schmidt, J. Phys.: Condens. Matter **21**, 225008 (2009).

[67] H. Gleiter, Acta Metall. **48**, 1 (2000).

[68] L. Kurmanaeva, Yu. Ivanisenko, J. Markmann, C. Kübel, A. Chuvilin, S. Doyle, R.Z. Valiev, and H.-J. Fecht, Mater. Sci. Eng. A**527**, 1776 (2010).

[69] Z. Lee, V. Radmilovic, B. Ahn, E.J. Lavernia, S.R. Nutt, Metall. Mat. Trans. A **41A**, 795 (2003).

[70] B.Q. Han, Z. Lee, D. Witkin, S. Nutt, E.J. Lavernia, Metall. Mat. Trans. A **36A**, 957 (2005).

[71] J. Lohmiller, N.C. Woo, and R. Spolenak, Mater. Sci. Eng. A **527**, 7731 (2010).

[72] Holden, Douglass, and Jaffee, ASTM Spec. Tech. **272**, 68 (1960).

[73] G. Gottstein, L.S. Shvindlermann, *Grain boundary migration in metals: thermodynamics, kinetics, applications*, CRC Press, Boca Raton (FL), 1999.

[74] J.W. Cahn, Y. Mishin, and A. Suzuki, Acta Mat. **54**, 4953 (2006).

[75] L. Kurmanaeva, Yu. Ivanisenko, J. Markmann, K. Yang, H.-J. Fecht, and J. Weissmüller, Phys. Stat. Sol. RRL **5-6**, 130 (2010).

[76] S. Crampin, D.D. Vedensky, and R. Monnier, Philos. Mag. A **67**, 1447 (1993).

[77] M. Pouryazdan Panah, D. Wang, T. Scherer, R.S. Averback, and H. Hahn, *Forced chemical mixing in Ag-Cu immiscible system using high pressure torsion*, Nano 2010 conference, Rome, 2010.

[78] C.E. Krill III, H. Ehrhardt, and R. Birringer, Z. Metallkd. A **96**, 10 (2005).

[79] R. Suryana, O. Nakatsuka, and S. Zaima, Jpn. J. Appl. Phys. **50**, 05EA09 (2011).

[80] S.D. Wicksell, Biometrika **17**, 84 (1925).

[81] H. Rietveld, J. Appl. Cryst. **2**, 65 (1969).

[82] B. Ilschner, R.F. Singer, *Werkstoffwissenschaften und Fertigungstechnik*, Springer Verlag, Berlin, 2010.

[83] C. Kittel, *Einführung in die Festkörperphysik*, Oldenbourg Verlag, München, 2006.

[84] A.M. Howatson, P.G. Lund, and J.D. Todd, *Engineering Tables and Data*, Kluwer Academic Publishers, Dordrecht, 1991.

Curriculum Vitae

The curriculum vitae is not included in the online version for reasons of data protection.

Publications

1. **A. Castrup**, C. Kübel, T. Scherer, H. Hahn, *Microstructure and residual stress of magnetron sputtered nanocrystalline palladium and palladium gold films on polymer substrates*, JVST A **29**, 021013 (2011).

2. A. Kobler, J. Lohmiller, J. Schäfer, M. Kerber, **A. Castrup**, A. Kashiware, P.A. Gruber, K. Albe, H. Hahn, C. Kübel, *Deformation-induced Grain Growth and Twinning in Nanocrystalline Palladium Thin Films*, Beilstein J. Nanotechnol. **4**, 554 (2013).

3. T. Ulyanenkova, R. Baumbusch, T. Filatova, S. Doyle, **A. Castrup**, P.A. Gruber, J. Markmann, J. Weissmüller, T. Baumbach, H. Hahn, O. Kraft, *A synchrotron tensile test setup for nanocrystalline thin films*, Phys. Status Solidi A **206**, 1795 (2009).

4. **A. Castrup**, S. Dasgupta, T. Scherer, H. Rösner, J. Ellrich, R. Kruk, M. Ghafari, H. Hahn, A. Hütten, D. Ebke, N.-N. Liu, I. Ennen, A. Thomas, J. Schmalhorst and G. Reiss, *Half-metallic* $\{Co_2MnSi/Co_2FeSi\}$ *multilayered Heusler electrodes in magnetic tunnel junctions*, J. Magn. Magn. Mat., **310** 2009 (2007).

5. J. Lohmiller, R. Baumbusch, M.B. Kerber, **A. Castrup**, H. Hahn, E. Schafler, M. Zehetbauer, O. Kraft, P.A. Gruber *Following the deformation behavior of nanocrystalline Pd films on polyimide substrates using in situ synchrotron XRD*, accepted by Mechanics of Materials (2013).

Acknowledgments

Finally I would like to thank all the people who supported me during the last years in writing my PhD thesis.

First of all, with a great pleasure I thank my supervisor, Prof. Dr. Horst Hahn, for his guidance and advice. He offered the opportunity to me to concern myself with an interesting and challenging topic. Furthermore, he provided me with the possibility of participating in conferences and workshops around the world.

In addition I would like to thank Prof. Dr. Martin Heilmaier for carefully revising my manuscript as well as for agreeing to be the second referee of this PhD thesis.

Many colleagues contributed with their expertise and companionship to the success of this work, these are:

- Dr. Yulia Ivanissenko and Dr. Lilia Kurmanaeva, who introduced me to tensile testing and discussed the mechanical properties with me.
- Dr. Christian Kübel, Dr. Torsten Scherer, and Aaron Kobler, who performed all the TEM measurements and part of the TEM sample preparation and were always there for fruitful discussions.
- Prof. Dr. Andrea Hodge, who invited me to her lab at LLNL in Livermore, CA, and introduced me to the mechanical investigation techniques in the field of thin films.
- Dr. Mohammad Ghafari, who provided me the opportunity to use the thin film diffractometer and was always there for fruitful discussions and moral support.
- Azad Darbandi, who performed the high temperature XRD measurements.
- Thomas Neithardt, who provided results of nanoindentation tests for comparison with the tensile test data.

- The Hahn-group at INT, KIT. We had lots of fun rebuilding our UHV-lab in the new INT building. Especially I have to thank: Dr. Robert Kruk, Philipp Leufke, Martin Limbach, Mohsen Pouryazdan, Dr. Babak Nasr, Dr. Subho Dasgupta, and Dr. Ajay Kumar Mishra.
- The members of DFG Research Group 714. There were always fruitful discussions at our meetings and workshops.
- The secretaries Erika Schütze, Birgit Limmer, and Renate Hernichel. They were always friendly and helpful.

Financial support provided by the Deutsche Forschungsgemeinschaft (DFG) through DFG Research Group 714 is gratefully acknowledged.

Last but not least I have to thank my husband Michael. He provided me with lots of moral support and never complained about my high work load, especially after I left the institute and continued writing in my free time. Additionally, I would like to thank my parents, they gave me moral support and encouragement, whenever it was needed.

Deutsche Zusammenfassung

Das Ziel dieser Arbeit ist die Erforschung der Verformungsprozesse in nanokristallinen Metallen und Legierungen. Dazu wurden die mechanischen Eigenschaften von nanokristallinen Palladium- und Palladium-Gold-Filmen untersucht, welche mittels Magnetronsputtern hergestellt wurden.

Ausgangspunkt war die Präparation von geeignetem Testmaterial mit nanokristalliner Struktur, hoher Dichte, wenigen Kristalldefekten und wenigen Verunreinigungen sowie niedrigen Eigenspannungen. Als Präparationsmethode wurde Ultra-Hoch-Vakuum-Magnetronsputtern ausgewählt, da gezeigt werden konnte, dass Metallfilme mit den gewünschten Eigenschaften durch Anpassung der Sputterparameter reproduzierbar hergestellt werden können. Für die Herstellung von 500 nm dicken Pd-Filmen wurde der Sputterprozess in regelmäßigen Abständen unterbrochen, um die nanokristalline Struktur zu erzielen. Die legierten PdAu-Filme wurden mittels Codeposition hergestellt. Die Abhängigkeit von strukturellen Eigenschaften, Eigenspannungen und dem während des Herstellprozesses eingestellten Argon-Arbeitsdruck wurde untersucht, wobei folgende Ergebnisse zu nennen sind:

- Die Eigenspannungen zeigen einen scharfen Übergang von Druckspannung zu hoher Zugspannung, gefolgt von einer stetigen Spannungsabnahme mit zunehmendem Argon-Arbeitsdruck.

- Die gemessenen kritischen Argon-Arbeitsdrücke für den Übergang von Druckspannung zu Zugspannung passen zu den von Thornton und Hoffmann vorhergesagten Werten.

- Die Mikrostruktur der Pd- und PdAu-Filme ist abhängig von den Eigenspannungen: Im Eigenspannungsminimum beim Übergang von Druck- zu Zugspannungen ist das Material nanokristallin mit einer Korngröße von circa 30 nm. Es zeigt säulenartige Kornstrukturen bei hoher Zugspannung und eine beginnende Dichtereduktion mit darauffolgender abnehmender Zugspannung.

Im Folgenden wurden in Abhängigkeit von der Zugdehnung die Mikrostruktur und die mechanischen Eigenschaften von 1-μm-dicken nanokristallinen Pd-Filmen und bimodal-strukturierten Pd-Filmen untersucht. Dazu wurden die Filme auf flexible Polyimid-Substrate aufgebracht, welche die empfindlichen Filme während der Versuchsvorbereitung stabilisierten. Zusätzlich wurde eine spezielle Einspannvorrichtung für Dünnschichtproben verwendet. Die Mikrostruktur der unverformten und der verformten Filme wurde mittels Transmissionselektronenmikroskopie untersucht. Folgende Ergebnisse wurden erzielt:

- Die Zugfestigkeit des nanokristallinen Pd ist mit 1200 MPa deutlich erhöht gegenüber konventionellem grobkörnigen Pd mit 270 MPa.
- Das elastische Substratmaterial mindert Spannungskonzentrationen im Film und ermöglicht eine hohe Dehnbarkeit des Films. Erste Risse treten erst bei 10 % Dehnung auf.
- Das bimodale Pd zeigt eine erhöhte Dehnbarkeit bei leicht reduzierter Zugfestigkeit im Vergleich zum nanokristallinen Pd. Dieses Verhalten wird mit unterschiedlichen Verformungsprozessen in den nanokristallinen und den grobkörnigen Bereichen erklärt: Die grobkörnigen Bereiche ermöglichen die Dehnbarkeit, während die nanokristallinen Körner die Zuglast aufnehmen.
- Das nanokristalline und bimodale Pd folgen im Wesentlichen der Hall-Petch-Beziehung mit den Parametern $k_y = 6.47$ MPa mm$^{1/2}$ und $\sigma_0 = 278$ MPa.
- Korngrenzengleiten und Zwillingsbildung wurden als Verformungsmechnismen im nanokristallinen Pd identifiziert. Mit zunehmender Dehnung nehmen sowohl die Korngröße als auch die Zwillingsdichte nahezu linear bis zum Spannungsmaximum zu, danach bleiben beide Werte stabil, bis Rissbildung eintritt.

Abschließend wurden die Mikrostruktur und die mechanischen Eigenschaften von 1-μm-dicken nanokristallinen PdAu-Mischkristall-Filmen als Funktion der Goldkonzentration untersucht. Ziel dieser Untersuchung war die Übertragung der Ergebnisse im reinen nanokristallinen Pd auf ein komplexeres Mischkristallsystem, welches aufgrund der verbesserten thermischen Kornstabilität eine höhere industrielle Anwendbarkeit bietet. Folgende Unterschiede in den mechanischen Eigenschaften wurden beobachtet:

- Das nanokristalline PdAu zeigt eine erhöhte thermische Kornstabilität im Vergleich zu reinem nanokristallinen Pd. Der Beginn des Kornwachstums verschiebt sich von 70 °C zu 115 °C.

- Mischkristallhärtung bewirkt eine erhöhte Zugfestigkeit des nanokristallinen PdAu mit 1,5 GPa im Vergleich zu 1,2 GPa bei nanokristallinem Pd. Die Zugfestigkeit steigt mit zunehmender Goldkonzentration bis 19 at.% Au, danach liegt die Zugfestigkeit stabil bei circa 1,4 GPa.
- Gleichzeitig wird eine zunehmende Versprödung mit steigender Goldkonzentration beobachtet.
- Vergleichsuntersuchungen mittels Nanoindenation zeigen einen nahezu linearen Anstieg der Quadratwurzel der Härte mit steigender Goldkonzentration bis 52 at.% Au. Dieses Verhalten bestätigt die Zunahme der kritischen Spannung für Versetzungen zur Überwindung von durch Fremdatome verursachten Spannungsfeldern mit steigender Fremdatomkonzentration.
- Kornwachstum und Zwillingsbildung während der Zugverformung nehmen mit zunehmender Goldkonzentration ab. Das abnehmende Kornwachstum wird durch Au-Atome bewirkt, die das Korngrenzengleiten behindern.
- Es wurde keine generelle Änderung der Verformungsprozesse durch das Legieren des nanokristallinen Pd mit Au festgestellt, unabhängig vom Goldgehalt dominiert Korngrenzengleiten den Verformungsprozess.